Inaugural dissertation

for

obtaining the doctoral degree

of the

Combined Faculty of Mathematics, Engineering and Natural Sciences

of the

Ruprecht - Karls - University

Heidelberg

Presented by

M.Sc. Halyna Karpusha

born in: Sumy, Ukraine

Oral examination: 29.09.2025

Structure-functional analysis of the small heat shock protein sequestrase Hsp42 from *Saccharomyces cerevisiae*

Referees: Prof. Dr. Bernd Bukau

Apl. Prof. Dr. Matthias Mayer

Abstract

Cells have evolved a complex network of mechanisms to maintain protein homeostasis. Among these, protein sequestration executed by small heat shock proteins (sHsps) serves as a strategy to prevent deleterious aggregation by capturing misfolded proteins into complexes that remain amenable to disaggregation by ATP-dependent chaperones. The size and morphology of these complexes are determined by the sHsp involved, the substrate, and the aggregation conditions. Some sHsps form only small, soluble assemblies (holdase activity), while others additionally generate large, microscopically visible inclusions (aggregase activity). The precise mechanisms governing the architecture of these complexes remain incompletely understood.

In this study, I investigated the structure and function of the *Saccharomyces cerevisiae* sHsp Hsp42, which exhibits both holdase and aggregase activities. Hsp42 is distinguished from other sHsps by an extended intrinsically disordered N-terminal region, which comprises a prion-like domain (PrLD) and a classical intrinsically disordered domain (IDD), defined by their amino acid composition. To dissect the structural organization of Hsp42, I employed a combination of biophysical, microscopic, and computational approaches. My data reveal that Hsp42 assembles into a range of oligomeric states, from dimers to decamers, with octamers being the predominant species. This oligomerization is dynamic and responsive to environmental triggers such as temperature and pH. Additionally, Hsp42 undergoes extremely rapid subunit exchange, a feature critical for its chaperone function.

Structural modeling predicts that Hsp42 forms planar ring-like octamers made of folded domains, flanked by disordered regions extending outward. This novel arrangement of ACDs in sHsp was never reported in other sHsps. This model was partially validated by cross-linking mass spectrometry, which identified proximity regions within the oligomer, and by limited proteolysis coupled to mass spectrometry, which identified exposed and protected regions.

I further demonstrate that Hsp42 forms substrate-dependent complexes of varying size. Cross-linking mass spectrometry identified multiple substrate-binding regions within Hsp42. Importantly, my findings confirm that Hsp42 and bound substrate are not passively released from these complexes and that complex dissolution requires the coordinated action of the Hsp70/Hsp40/Hsp100 disaggregation machinery.

Finally, I dissected the contributions of PrLD, IDD, and other domains and conserved motifs of Hsp42 to substrate sequestration and recovery. Using a series of deletion and point mutants, I show that distinct domains of Hsp42 mediate substrate interaction and complex formation, with the PrLD playing a central role – its deletion markedly reduced chaperone activity. In contrast, other domains are required for efficient substrate handover to the disaggregase system. The IDD was found to be essential for forming large Hsp42-substrate complexes and to confer temperature-dependent aggregase activity. Moreover, the IDD appears to influence complex architecture in a manner that facilitates access by Hsp70, while blocking access by standalone Hsp100 disaggregases.

Zusammenfassung

Zellen haben ein komplexes Netzwerk von Mechanismen zur Aufrechterhaltung der Proteinhomöostase entwickelt. Die Sequestrierung von Proteinen durch kleine Hitzeschockproteine (sHsps) ist eine Strategie zur Verhinderung schädlicher Aggregation, bei der fehlgefaltete Proteine in Komplexe eingeschlossen werden, die durch ATP-abhängige Chaperone dissoziiert werden können. Die Größe und Morphologie dieser Komplexe wird durch die Identität des sHsp, das Substrat und die Aggregationsbedingungen bestimmt. Einige sHsps bilden nur kleine, lösliche Assemblierungen (Holdase-Aktivität), während andere zusätzlich große, mikroskopisch sichtbare Einschlusskörper bilden (Aggregase-Aktivität). Die genauen Mechanismen, die die Architektur dieser Komplexe steuern, sind noch nicht vollständig geklärt.

In dieser Studie untersuchte ich die Struktur und Funktion des sHsp Hsp42 von *Saccharomyces cerevisiae*, das sowohl Holdase- als auch Aggregase-Aktivitäten aufweist. Hsp42 unterscheidet sich von anderen sHsps durch eine ausgedehnte intrinsisch ungeordnete N-terminale Region, die eine prionähnliche Domäne (PrLD) und eine klassische intrinsisch ungeordnete Domäne (IDD) umfasst, welche durch ihre Aminosäurezusammensetzung definiert sind. Um die strukturelle Organisation von Hsp42 zu bestimmen, habe ich eine Kombination aus biophysikalischen, mikroskopischen und computergestützten Ansätzen verwendet. Meine Daten zeigen, dass sich Hsp42 aus verschiedenen oligomeren Zuständen zusammensetzt, von Dimeren bis zu Dekameren, wobei Oktamere die vorherrschende Spezies sind. Diese Oligomerisierung ist dynamisch und reagiert auf Umwelteinflüsse wie Temperatur und pH-Wert. Darüber hinaus unterliegt Hsp42 einem sehr schnellen Austausch von Untereinheiten, was für seine Chaperonfunktion entscheidend ist.

Die Strukturmodellierung sagt voraus, dass Hsp42 planare, ringförmige Oktamere bildet, die aus gefalteten Domänen bestehen, flankiert von ungeordneten Regionen, die sich nach außen erstrecken. Dieses Modell wurde teilweise durch Vernetzungs-Massenspektrometrie validiert, bei der angrenzende Regionen innerhalb des Oligomers identifiziert wurden, sowie durch limitierte Proteolyse in Verbindung mit Massenspektrometrie, bei der exponierte und geschützte Regionen unterschieden wurden.

Außerdem konnte ich zeigen, dass Hsp42 substratabhängige Komplexe unterschiedlicher Größe bildet. Mit Hilfe der Quervernetzungs-Massenspektrometrie wurden mehrere substratbindende Regionen in Hsp42 identifiziert. Wichtig ist, dass meine Ergebnisse bestätigen, dass Hsp42 und gebundenes Substrat nicht passiv aus diesen Komplexen freigesetzt werden und dass deren Dissoziation die koordinierte Wirkung der Chaperonmaschinerie Hsp70/Hsp40/Hsp100 erfordert.

Schließlich untersuchte ich die Beiträge von PrLD, IDD und anderen Domänen und konservierten Motiven von Hsp42 zur Sequestrierung und Wiederherstellung von Substraten. Anhand einer Reihe von Deletions- und Punktmutanten konnte ich zeigen, dass bestimmte Domänen von Hsp42 die Substratinteraktion und die Komplexbildung vermitteln, wobei die PrLD eine zentrale Rolle spielt - ihre Deletion reduziert die Chaperonaktivität deutlich. Im Gegensatz dazu sind andere Domänen für eine effiziente Substratübergabe an das Disaggregasesystem erforderlich.Es wurde festgestellt, dass die IDD für die Bildung großer

Hsp42-Substrate Komplexe unerlässlich ist und Hsp42 eine temperaturabhängige Aggregaseaktivität verleiht. Darüber hinaus scheint die IDD die Komplexarchitektur in einer Weise zu beeinflussen, die den Zugang für Hsp70 erleichtert, während es die Bindung von eigenständigen Hsp100 Disaggregasen verhindert.

Table of Contents

1. Introduction

1.1. Protein homeostasis

Any living organism relies on proteins for performing their biological processes like homeostasis, organization, growth and adaptation, metabolism, response to stimuli, reproduction, etc. Even viruses whose living status is debatable in the scientific community (Harris and Hill, 2021) rely on the protein shell (capsid) and other viral proteins that enable a virus to survive, infect host cells, and propagate effectively. The human body contains ~20,000 protein-coding genes, which give rise to ~70,000 splice variants with many hundreds of thousands of post-translationally modified variants and single-nucleotide polymorphs (Aebersold et al, 2018). These proteins must fold to acquire the correct three-dimensional structure (native conformation) to function properly. While some proteins can fold independently due to the chemical properties of their amino acids, many require the co- or post-translational assistance of other proteins, i.e., molecular chaperones, or interaction with ligands or partner proteins.

Once folded, proteins are not rigid molecules. Many of them can continuously interconvert between conformational states and undergo a shift to a metastable state. This can lead to the formation of partly misfolded proteins in the cells. Protein misfolding could lead to the loss or gain of function or the interaction with other misfolded proteins and subsequent protein aggregation – the irreversible, uncontrollable process of clamping together misfolded proteins to form large amorphous masses. In addition, various endogenous and exogenous stress conditions may significantly increase the concentration of the misfolded or even fully unfolded proteins, resulting in protein aggregation. Moreover, some fully functional proteins can undergo conformational changes to form β-sheets and assemble into pathological fibrillar amyloids.

To ensure the correct protein folding and its surveillance throughout life, cells develop a complex protein quality control system (PQS). PQS encompasses several intervened mechanisms: sequestration of misfolded proteins, disaggregation and refolding of misfolded proteins by molecular chaperones, ubiquitin-proteosome degradation system, and autophagy (Fig. 1).

1.1.1. Protein sequestration

Under various stress conditions, aging, or mutations, misfolded proteins can form aggregates that are associated with cytotoxicity and disease (Morimoto 2008, Tsoi et al., 2023). However, increasing evidence suggests that cells have evolved highly coordinated mechanisms to control the aggregation of misfolded proteins by sequestering them in a refolding amenable form, potentially mitigating their toxic effects. These sequestration processes form inclusions in both the cytoplasm and nucleus, orchestrated by distinct classes of molecular chaperones, including small heat shock proteins and Hsp40 (JDP: J-domain protein) family (Ho et al., 2019; Cabrera et al., 2020). Additionally, membraneless organelles, such as stress granules in the cytoplasm and nucleoli in the nucleus, have been implicated in the sequestration of misfolded proteins (Mateju et al., 2017; Frottin et al., 2019). Regardless of the sequestration mechanism, misfolded proteins undergo a shared fate – they are disaggregated if needed and

subsequently refolded by specific molecular chaperones or cleared by autophagy or proteasomal degradation.

1.1.2. Protein disaggregation and refolding by molecular chaperones

Molecular chaperones represent diverse proteins that assist in protein folding, refolding, and disaggregation. Different families of molecular chaperones perform their functions differently (Hartl et al., 2011). Among all families, the Hsp70 family plays a central role by binding to misfolded proteins and using ATP hydrolysis to facilitate their proper (re)folding. Hsp70 consist of three domains – the N-terminal ATPase domain (NTD), the substrate-binding domain (SBD), and the C-terminal domain or the Lid. Refolding of misfolded proteins is initiated by their binding to the SBD in its open state, which is allosterically ensured by binding ATP to the NTD. Substrate binding (together with co-chaperone Hsp40) stimulates ATP hydrolysis to ADP and a confirmation change which leads to the Lid domain closure of the bound substrate. Another co-chaperone – nucleotide exchange factor – exchange ADP to ATP, which triggers the Lid to open and return the SBD in the open state. Upon opening, the substrate is released and may be refolded spontaneously or with the assistance of the downstream chaperones.

Members of the Hsp40 family (J-domain proteins or JDPs) act as co-chaperones by delivering misfolded substrates to Hsp70 and stimulating its ATPase activity. JDPs are divided into three classes (A, B, C). Classes A and B are canonical Hsp40 members and consist of the N-terminal J-domain, an adjacent glycine-rich region (GF), two C-terminal domains for substrate binding, and a dimerization domain. In addition, class A contains a zinc-finger-like domain. Class C JDPs are structurally more diverse but also contain a J-domain. The J-domain in Hsp40 interacts with Hsp70 at the interface between the NBD and SBD, bringing the substrate in**to** close proximity of the Hsp70 SBD, and promotes allosteric transition in Hsp70, which triggers ATP hydrolysis (Tomiczek et al., 2020). In class B JDPs, the additional interaction of C-terminal domain I in JDPs with the C-terminal extreme EEVD motif of Hsp70 has to happen prior the J-domain interaction with Hsp70 (Faust et al., 2020).

Hsp60 family chaperonins form large, cage-like oligomeric complexes that encase misfolded proteins, aiding in their ATP-dependent refolding. The family of Hsp90 functions through ATP-driven conformational changes and collaborates with co-chaperones to mediate the structural maturation and functional regulation of numerous client proteins, including kinases and steroid hormone receptors.

The last family – Hsp100 chaperones – works in disaggregation by extracting misfolded polypeptides from aggregates through a threading mechanism, in which substrates are translocated through the central pore of the hexameric complex (Glover and Lindquist, 1998; Mogk et al., 2015). Hsp100 chaperones can be associated with AAA+ peptidases to ultimately degrade misfolded proteins.

1.1.3. Ubiquitin-proteasome system

The ubiquitin-proteasome system is another mechanism to maintain protein homeostasis in cells by degrading misfolded or unneeded proteins. Proteins destined for degradation are post-translationally tagged with polyubiquitin peptides by a cascade of enzymes, marking them for recognition by the 26S proteasome, which unfolds and degrades them into peptides (Kandel et al., 2024). The E1 ubiquitin-activating enzyme carries a single ubiquitin peptide, which is attached to E1 via a thioester bond to a cysteine residue using ATP energy. This ubiquitin is transferred to a cysteine on the E2 ubiquitin-conjugating enzyme. Finally, the E3 ubiquitin ligase transfers ubiquitin from E2 to the protein targeted for degradation. A polyubiquitin chain is created via the same cycle by addition of multiple ubiquitin peptides. The 26S proteasome is a large protein complex which consists of the narrow cylindrical 20S proteolytic core complex and the 19S proteasome cap. The cap recognizes the ubiquitinated proteins, removes ubiquitin, unfolds them, and forwards them into the proteolytic core. By the coordinated work of the 20S subunits, the target protein is degraded into small peptides and released for further reuse in the cell using ATP energy.

1.1.4. Autophagy

Autophagy is a process in which cells degrade and recycle protein aggregates and damaged organelles to maintain homeostasis and adapt to stress. It begins with the initial nucleation of the isolated membrane/phagophore. Nucleation is driven by the activation and assembly of autophagy-related proteins at specific membrane sites. The isolated membrane/phagophore is elongated by lipid transfer and eventually closed to form a double-membraned autophagosome enclosing aggregates or damaged organelles. Mature autophagosome merges with lysosomes, forming autolysosomes where lysosomal hydrolases break down the protein aggregates and organelles for further cell reuse (Morishita and Mizushima, 2019).

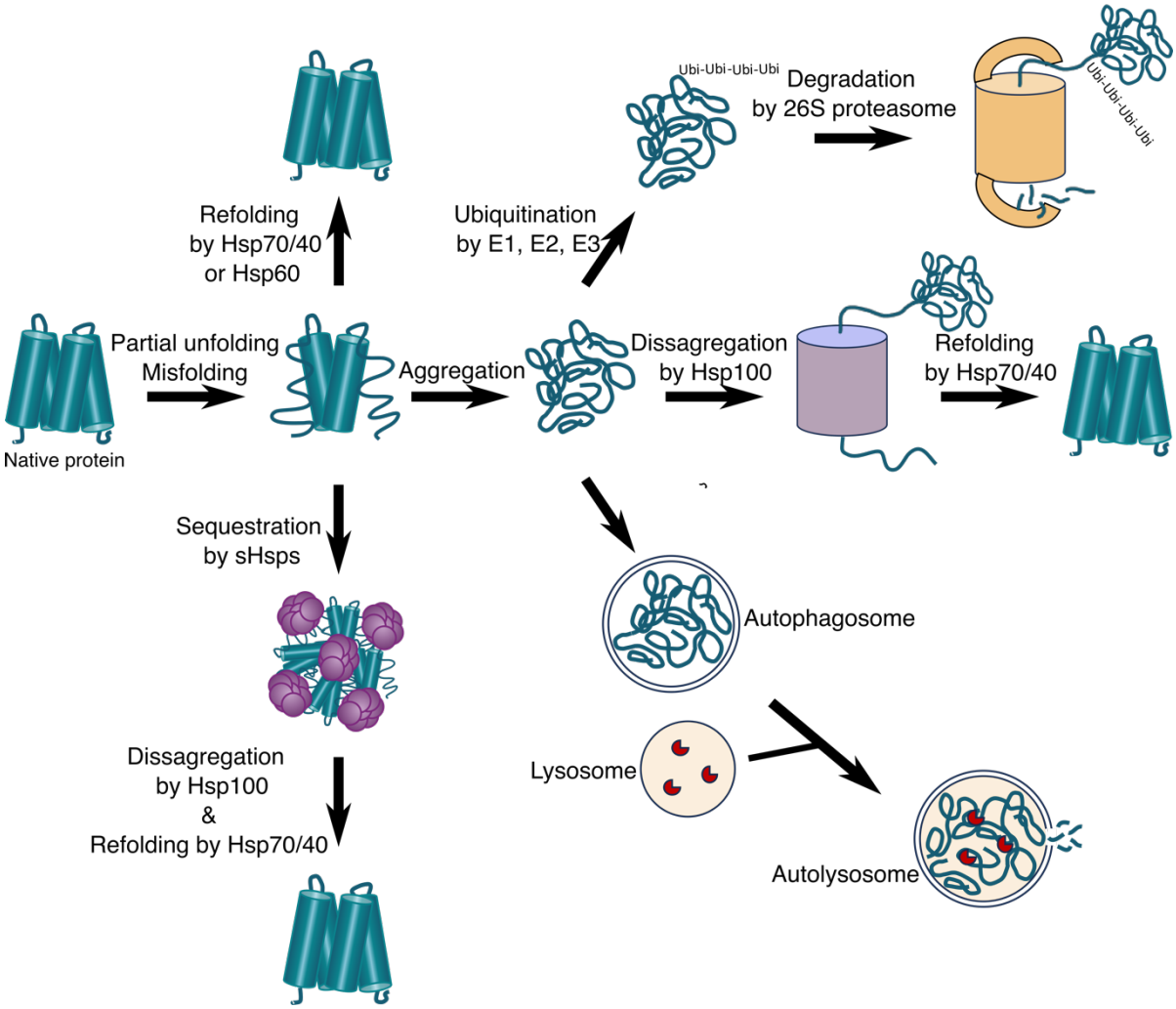

Figure 1. Protein quality control system. Schematic depiction of four major pathways involved in maintaining protein homeostasis by promoting protein refolding or targeting misfolded proteins for degradation.

1.2. Small heat shock proteins: protein sequestrases

One of the discovered mechanisms to sequester misfolded proteins is mediated by the small heat shock protein family (sHsps). sHsps were considered as holdases for a long time: they bind to misfolded proteins and protect them from uncontrolled aggregation by forming small soluble sHsp-substrate complexes (Haslbeck et al., 2005). In addition to the holdase activity, some sHsps were shown to co-aggregate with misfolded proteins, triggering the formation of large microscopically visible inclusions *in vivo* and *in vitro* – a so-called aggregase activity (Specht et al., 2011; Shrivastava et al., 2022). Aggregase activity is seen as a variation of the holdase activity and is speculated to result in a similar molecular organization of sHsp-substrate complexes but of larger size (Reinle et al., 2022). Independent of the size of the formed sHsp-substrate complex, the activity of small heat shock protein can be named sequestrase activity. Some reports show that the stress conditions, substrate identity, and the concentration of sHsps define the size of formed complexes *in vivo* and *in vitro* (Iburg et al., 2019, Ungelenk et al., 2016; Hantke et al., 2019). However, the specific features of small heat

shock proteins and the mechanism that enables some, but not all, sHsps to form large, reversible complexes with misfolded substrates – alongside smaller assemblies – remain to be elucidated.

1.3. Structure of small heat shock proteins

Small heat shock proteins are evolutionarily conserved proteins found in all living organisms, with their number increasing with the organism's complexity: one or two in bacteria, ten in human, and 19 in *Arabidobsis thaliana* (Haslbek et al., 2005). The key to understanding their function is their dynamic structure, which is present in all states from monomeric to larger oligomeric.

Small heat shock proteins have small molecular weights (12–43 kDa) and consist of a conserved α-crystallin domain (ACD) flanked by the non-conserved N- and C-terminal extensions (NTE and CTE) (Fig. 2A). ACD is a central structural element of 90–100 residues, which is made of an IgG-like β-sandwich with seven to eight antiparallel β-sheets. The multiple structures of isolated ACDs of different sHsps available in the public Protein Data Bank display a remarkable structural similarity. NTEs and CTEs are intrinsically disordered regions of varied sequence and length in different organisms. NTEs are especially diverse in length between 24 and 247 residues. Some regions within NTEs are predicted to have α-helices, but the experimental structure determination of NTEs is usually challenging due to its intrinsic disorder. CTEs is as structurally flexible as NTE, although it has a much shorter length of below 20 residues. CTEs contain a conserved I/V-x-I/V motif – Ile or Val residues separated by any other residue (for simplicity, will be called IxI motif in this work).

The distinguishing feature of all small heat shock proteins is their oligomerization to form large assemblies of 2–40 protomers (Janowska et al., 2019). The oligomerization is hierarchical: first, dimers are formed by interactions between the ACD of two protomers, and then multiple interactions between different domains contribute to the formation of the higher-order oligomers. There are two types of how ACDs interact to form dimers: first, in archaea, bacteria, fungi, and plants, by swapping the β6 strand of one ACD and interacting with the β2 strand of the neighboring ACD; second, in metazoan, by the interaction of the extended β6-7 strand of one ACD with the extended β6-7 strand of a partnering ACD (Fig. 2B).

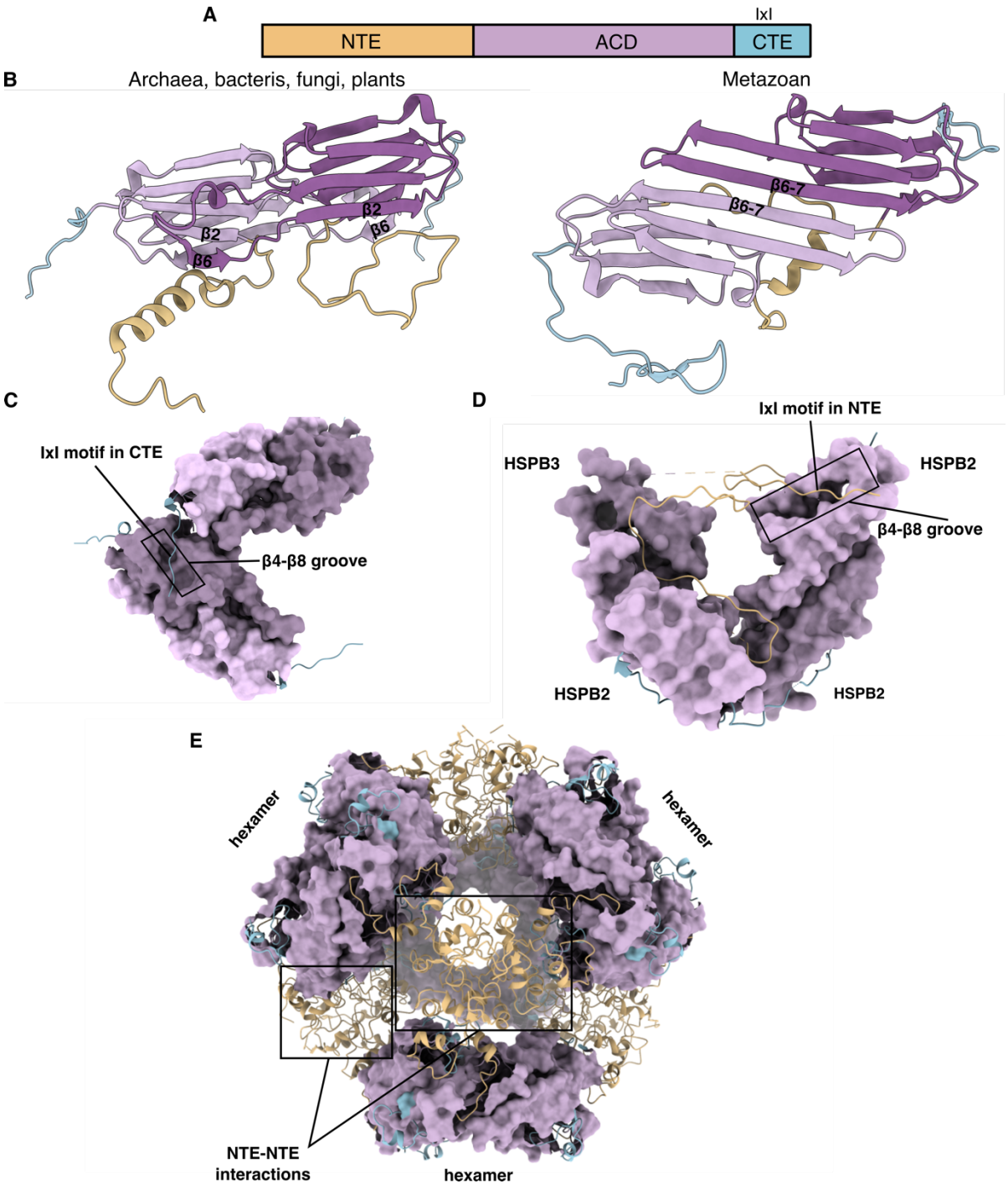

Figure 2. Hierarchical oligomerization of small heat shock proteins. A. Domain organization. **B.** Two types of dimer formation. Left – by swapping the β6 strand of one ACD and interaction with the β2 strand of the neighboring ACD in Hsp16.0 of *S. pombe* (PDB 3W1Z), right - by the interaction of the extended β6-7 strand of one ACD with the extended β6-7 strand of a partnering ACD in Sip1 of *C. elegans* (PDB 4YDZ). **C.** Interaction of the IxI motif of one dimer with the β2-β4 hydrophobic groove of a neighboring dimer in Hsp16.5 in *M. jannaschii* (PDB 1SHS). The ACD dimers are depicted as surface, CTE as ribbon. **D.** Interaction of the IxI-like motif in the NTE of one dimer with the β2-β4 hydrophobic groove of a neighboring dimer in the human HSPB2/B3 hetero-tetramer (PDB 6F2R). The ACD dimers are depicted as surface, NTE and CTE as ribbon. **E.** Structure of human HSPB5 24-mer formed by NTE-NTE interaction between four hexamers. Three hexamers are indicated in the structure, the fourths is located at the back. (PDB 2YGD).

ACD dimers serve as a template that presents several grooves, different in different types of dimers, into which other segments (NTEs and CTEs) of sHsps can bind. Multiple intermolecular interactions have been identified as contributors to higher-order oligomerization. Among these, the most frequently reported is the interaction between the IxI motif of one CTE and the β4-β8 hydrophobic groove in the ACD of an adjacent dimer, which leads to the formation of a tetramer in many sHsps (Fig. 2C) (Kim et al., 1998; van Montfort et al., 2001, Fleckenstein et al., 2015; Mühlhofer et al., 2021). Additionally, certain NTEs contain IxI-like motifs, which can compete with the IxI motif in the CTE for binding to the β4-β8 hydrophobic groove in the ACD, as observed in experimentally resolved structures of the human HSPB2/HSPB3 heterotetramer and HSPB6 (Fig. 2D) (Clark et al., 2018; Sluchanko et al., 2017; Weeks et al., 2014). The structure of a full-length human HSPB6 also revealed an additional ionic interaction between the ^{27}RLFDQRFG^{34} motif in NTE, which is the only NTE conserved motif in human sHSPs, and the β3-β3 hydrophilic groove in ACD (Sluchanko et al., 2017).

NTE-NTE interactions display remarkable versatility. While barely no specific sequence motifs in the NTE have been directly linked to oligomerization, these interactions predominantly contribute to the formation of higher-order oligomers. For instance, NTE-mediated interactions between hexamers of human HSPB5 drive the formation of a tetrahedral 24-mer (Fig. 2E) (Braun et al., 2011). The interaction between different CTEs was also identified to contribute to the tetramer formation in *C. elegans* Hsp16 and human HSPB5 (Fleckenstein et al., 2015; Delbecq et al., 2015).

The above-described interactions are not universally present across all sHsps. For example, the widely studied IxI motif is absent in the ubiquitously expressed human HSPB6 (Sluchanko et al., 2017). This suggests that the unique structural and symmetrical properties of each sHsp arise from a distinct combination of known and yet-to-be-identified interactions. Furthermore, these interactions are likely transient and exhibit varying degrees of stability, enabling sHsps to maintain a dynamic nature and capacity for dissociation.

1.4. Subunit exchange of small heat shock proteins

Most small heat shock proteins simultaneously assemble into an ensemble of oligomers, the equilibrium of which can be shifted. The transient nature of NTE and CTE interactions is believed to be the key to this plasticity. Small changes in environmental conditions often tip the balance in favor of one interaction over another, leading to the formation of a different ensemble of oligomers. These dynamics are achieved by the constant subunit exchange – the process where individual subunits dissociate from and reassociate with oligomeric complexes. Different studies report a time of 20-90 minutes to substitute all subunits and reach equilibrium if two pools of sHsp oligomers are mixed (Aquilina et al., 2005; Hilton et al., 2013; Grousl et al., 2018). Unsurprisingly, the subunit exchange is accelerated by an increased temperature (Bova et al., 2002; Benesch et al., 2010; Baldwin et al., 2011).

Little is known about the mechanism of the subunit exchange. Contrary to earlier assumptions that dimers are the fundamental building blocks, human HSPB5 undergoes subunit exchange via monomers (Delbecq et al., 2015). Recruitment into oligomers depends on interactions with the CTE of existing oligomers, with exchange rates influenced by CTE accessibility.

1.5. Substrate binding of small heat shock proteins

Small heat shock proteins form complexes with a wide range of substrate proteins to prevent their deleterious aggregation. Proteomics-based studies identified the broad substrate promiscuity of sHsps, which is demonstrated by their ability to bind diverse clients: for instance, IbpB in *E. coli* was identified to associate with at least 94 substrate proteins during heat shock (Fu et al., 2013), while the human ubiquitous HSPB1 interacts with at least 109 distinct heat-sensitive clients (Mymrikov et al., 2017). sHsps can sequester multiple substrates simultaneously, forming large sHsp-substrate complexes. Although the precise substrate-binding sites remain unclear, numerous studies suggest that the NTE plays a crucial role in substrate interaction, as its full or partial deletion typically results in a complete loss of chaperone activity (Mauk et al., 2011; Heirbaut et al., 2014; Mainz et al., 2015; Grousl et al., 2018). Substrate recognition by the NTE appears to be driven by hydrophobic and/or electrostatic interactions. The cross-linking study by Jaya et al. (2009) identified multiple hydrophobic substrate-binding sites within the NTE of *P. sativum* Hsp18.1. Additionally, an NMR study by Zhang et al. (2022) demonstrated that the N-terminal region of human HSPB1 interacts with phosphorylated tau fibrils via electrostatic interactions.

The α-crystallin domain has also been implicated in substrate binding. Mymrikov et al. (2015) demonstrated that the ACD of human HSPB5 alone is sufficient to perform its chaperone function toward the amyloid fibril-forming peptide Aβ1-40 *in vitro*. However, the N-terminal extension of HSPB5 was shown to be indispensable for suppressing lysozyme aggregation, suggesting substrate-specific recognition by HSPB5. The hydrophobic β4-β8 groove within the ACD of various sHsps has been identified as a substrate-binding site (Mymrikov et al., 2015; Liu et al., 2018; Baughman et al., 2019). Furthermore, the β5-β7 loop, which connects the β-5 and β-7 strands within the ACD of *A. thaliana* plastid Hsp21, has been shown to form intermolecular contacts with a substrate (Yu et al., 2021).

Substrate binding by the CTE has also been reported in recent years (Ungelenk et al., 2016; Yu et al., 2021). However, the mechanisms mediating these interactions remain poorly understood. Overall, current evidence suggests that all domains of sHsps contribute to substrate recognition and chaperone activity, with their specific roles varying depending on the sHsp and its substrate.

1.6. Regulation of sHsp structure and function

The expression of many small heat shock proteins is induced by environmental stress, i.e., heat shock, or during particular embryonic development stages (e.g., Hsp26 in *S. cerevisiae* and Sip1 in *C. elegans*, respectively). However, some sHsps are constitutively expressed under physiological conditions. In addition to maintaining cellular proteostasis, they perform specialized tissue-specific functions in multicellular organisms. For example, human HSPB1 contributes to cytoskeleton stabilization and apoptosis regulation, while human HSPB5 is involved in membrane stabilization in nervous tissue (Hoffman et al., 2022; Bartelt-Kirbach et al., 2016). Cells have evolved multiple mechanisms to regulate the structural and functional states of both constitutively expressed and stress-inducible sHsps, ensuring their precise activity in the appropriate cellular context and timing.

1.6.1. Thermal regulation

The name of small heat shock proteins implies a significant role of temperature in their activity. In addition to being under the expression control of heat shock element promoters, many small heat shock proteins are activated by elevated temperatures through structural rearrangement. For example, numerous *in vitro* studies have identified small heat shock proteins that are activated to suppress protein aggregation only at elevated temperatures, such as *M. jannaschii* Hsp16.5 or *S. cerevisiae* Hsp26 (Bova et al., 2002; Haslbeck et al., 1999). The common view is that elevated temperatures cause oligomer dissociation into smaller oligomers, which results in the exposure of the main hydrophobic substrate-binding sites in the NTE, thereby activating the sHsps (Eisenhardt, 2013). Conversely, Franzmann et al. (2005) proposed that the dissociation of *S. cerevisiae* Hsp26 into dimers occurs coincidentally simultaneously with a conformational rearrangement in the NTE, but is not required for activation. The recent cryo-EM structure of *M. jannaschii* HSP16.5 demonstrates that temperature-dependent activation induces only subtle structural rearrangements relative to the inactive state. These changes are localized primarily to the NTE, suggesting increased NTE flexibility and, consequently, enhanced subunit exchange dynamics without complete oligomer dissociation (Miller and Reichow, 2025). The impact of temperature on sHsp oligomerization and activation remains a subject of ongoing debate. This discrepancy may arise from the inherent diversity within the sHsp family, implying that thermal responsiveness is likely species-specific. These findings underscore the importance of investigating individual sHsps rather than extrapolating general mechanisms across the entire family.

1.6.2. pH regulation

Numerous studies have shown that a decrease in pH can trigger changes in sHsp oligomerization and activity. This is particularly relevant as cells experience a drop in the pH value under different conditions – disease, heat shock, starvation, in particular tissues, or embryonic development stages (McVicar et al., 2014; Weitzel et al., 1987; Orij et al., 2009; Oka and Futai, 2000; Mathias et al., 1991). Multiple studies suggest that activation of human sHsps happens via protonation of His residues in the ACD upon the pH drop, leading to oligomer destabilization and dissociation (Rajagopal et al., 2015b; Clouser and Klevit, 2017). The small heat shock protein Sip1 from *C. elegans* exhibits optimal activity within a pH range of 5.8 to 6.3, while it remains inactive at pH 7.5 and 8.2, where other *C. elegans* sHsps demonstrate peak activity (Fleckenstein et al., 2015). Similar to human sHsps, Sip1 shifts notably toward smaller oligomeric forms as the pH value decreases.

1.6.3. Regulation by phosphorylation

Post-translational modifications, particularly phosphorylation, have frequently been reported in eukaryotes as a mechanism to regulate sHsp activity. Extensive studies on human HSBP1, HSPB4, and HSPB5 show the phosphorylation at different sites of their NTEs (Sluzala et al., 2025). The phosphorylation substantially decreases the oligomerization size relative to the unphosphorylated variant (Ito et al., 2001; Peschek et al., 2013). In the majority of cases, though not universally, phosphorylation is linked to an enhancement of chaperone activity toward client proteins (Ecroyd et al., 2007; Peschek et al., 2013; Jovcevski et al., 2015). The increased chaperone activity is attributed to the exposure of NTEs upon oligomer dissociation

and, as a result, an enhanced substrate binding. Phosphorylation has also been shown to directly affect the structure of the NTE and its interaction with clients, as demonstrated by Sluchanko et al. (2017). They reported that human dimeric HSPB6 is phosphorylated in its disordered N-terminus, which enhances its interaction with the 14-3-3 protein, leading to a well-defined conformation upon binding.

Recent findings by Mühlhofer et al. (2021) in *C. cerevisiae* Hsp26 identified phosphorylation sites in the ACD and CTE, in addition to the NTE. Consistent with the current understanding of the activation for most of sHsps, they demonstrated that the introduction of negative charges by phosphomimetics at specific positions destabilizes domain interactions and shifts the oligomer ensemble toward smaller assemblies, rendering Hsp26 active.

The extent of phosphorylation matters: for instance, phosphorylation of a single serine in the NTE of human HSPB1 caused partial dissociation of oligomers, whereas triple phosphorylation in the NTE resulted in complete dimer dissociation. The ability of HSPB1 to prevent client aggregation correlated with the extent of dissociation (Jovcevski et al., 2015). An opposite effect was observed for human HSPB5: a single phosphomimetic mutation in the NTE exhibited antiapoptotic effects by inhibiting caspase-3 activity, whereas the triple phosphomimetic variant did not (Morrison et al., 2003).

1.7. The architecture of small heat shock protein – substrate complexes

Numerous efforts have been undertaken to reveal the architecture of small heat shock protein-substrate complexes. Negative-stain electron microscopy (EM) images frequently reveal spherical or elongated particles ranging from 15 to 50 nm in diameter (Mühlhofer et al., 2021; Miller et al., 2024). In cases where sHsps promote regulated aggregation, the resulting assemblies typically appear as amorphous masses of micrometer-scale dimensions (Grousl et al., 2018; Strauch et al., 2021).

The structural heterogeneity (polydispersity) of sHsp oligomers is further exacerbated upon substrate binding, complicating high-resolution structural determination. To date, only one study has resolved the high-resolution structure of an sHsp-substrate complex: Miller and Reichow (2025) used cryo-EM to show that the 24-mer *M. jannaschii* Hsp16.5 encapsulates misfolded lysozyme, thereby preventing its aggregation. The encapsulation of lysozyme begins when the Hsp16.5 oligomer becomes destabilized upon binding to substrate-loaded dimers. As a result, the Hsp16.5–lysozyme complex extends in size, eventually incorporating up to 36 protomers and reaching a length of around 15 nanometers. The dynamic nature of both the NTEs and CTEs of Hsp16.5 facilitates these structural transitions and enables the formation of larger oligomers that enclose the substrate.

The ability of Hsp16.5 to encapsulate misfolded substrate is attributed to the internal positioning of substrate-binding NTEs within the Hsp16.5-substrate complexes. However, this configuration may vary among sHsps. For example, a cryo-EM study of *C. elegans* Hsp17 oligomers, also comprising 24 protomers, revealed that only half of its NTEs are positioned internally in the apo-state, while the remaining face outward, suggesting that substrate binding may also occur at the exterior surface (Strauch et al., 2023). Furthermore, some sHsps exhibit

completely distinct mechanisms of substrate interaction. For instance, *A. thaliana* Hsp21 dissociates from a 24-mer to monomers upon heat stress, to stabilize its natural substrate, 1-deoxy-D-xylulose 5-phosphate synthase (DXPS), and preventing its aggregation (Yu et al., 2021).

Importantly, sHsps that promote aggregation of misfolded proteins may not utilize an encapsulation mechanism at all. These findings collectively suggest that there is no universal model for substrate recruitment to sHsp-substrate complexes. The structural and functional diversity among sHsps, their substrate specificity, and the diversity of substrate-binding modes point to the existence of multiple architectures.

1.8. Dissolution of sHsp-substrate complexes by ATP dependent chaperones

There is evidence that the sequestration of misfolded proteins into sHsp complexes has a cytoprotective function under different stress conditions or aging (Hanktle, et al. 2019; Shrivastava et al., 2022; Iburg et al., 2019). A study by Ungelenk et al. (2016) demonstrated that sHsps such as Hsp26 and Hsp42 bind to substrates in early stages of unfolding, preserving them in near-native conformations.

The findings by Żwirowski et al. (2017) suggest that small bacterial sHsp-substrate complexes are surrounded by a dynamic outer shell composed of the hetero-oligomeric bacterial sHsps IbpA and IbpB (IbpAB). This outer shell is displaced by the bacterial Hsp70 homolog DnaK, which subsequently facilitates the recruitment of the bacterial Hsp100 disaggregase ClpB, leading to substrate disaggregation. The direct physical interactions between sHsps and members of the Hsp70 family have not been conclusively demonstrated. The authors propose that IbpAB displacement occurs through a passive competitive mechanism, wherein DnaK binds to misfolded proteins as sHsps dissociate spontaneously. Such dynamic interactions have been previously observed in plant and cyanobacterial sHsps, including pea Hsp18.1 and *Synechocystis* Hsp16.6, which exhibit their continuous dissociation and reassociation with sHsp-substrate assemblies (Friedrich et al., 2004). However, the lack of knowledge and the potential diversity of sHsp-substrate architectures suggest that additional mechanisms may be involved in the dissolution of sHsp-substrate complexes in other species.

1.9. Hsp42 from *Saccharomyces cerevisiae*

Hsp42 is one of two small heat shock proteins identified in the baker's yeast *S. cerevisiae*. It was the first sHsp discovered to possess aggregase activity, characterized by its ability to sequester misfolded proteins into large peripheral cytosolic inclusions visible under a light microscope – a function not observed for the second yeast sHsp, Hsp26 (Specht et al., 2011). This sequestration activity provides a survival advantage to yeast cells under repeated heat stress, a physiologically relevant stress in natural environments (Ungelenk et al., 2016). In addition, Hsp42 reversibly sequesters misfolding-prone proteins into Hsp42-associated granules upon chronological aging (Lee et al., 2018).

Several *in vitro* studies have shown that Hsp42 can form complexes of varying sizes with substrates, depending on both the nature of the substrate and the stress conditions (Ungelenk

et al., 2016; Grousl et al., 2018). Regardless of complex size, sequestration by Hsp42 facilitates subsequent refolding of client proteins by ATP-dependent chaperones.

Structurally, Hsp42 is distinguished from other sHsps by an unusually long N-terminal extension, which can be subdivided into a prion-like domain (PrLD) and a canonical intrinsically disordered domain (IDD) (Fig. 3A). The PrLD is enriched in glutamine/asparagine and aromatic residues while being depleted of charged amino acids, whereas the IDD is rich in acidic residues and lacks aromatic and aliphatic amino acids. Both N-terminal extensions – except for approximately the first 12 residues in the PrLD – and the C-terminal extension are predicted to be intrinsically disordered, consistent with other sHsps (Fig. 3B). However, the exceptional length of these extensions results in nearly 70% of the Hsp42 sequence being predicted as disordered.

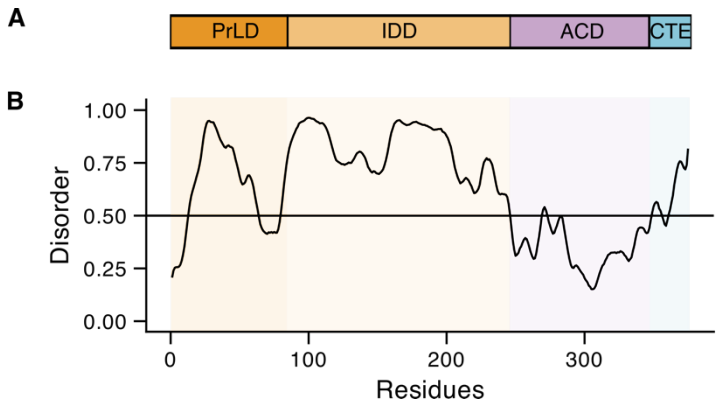

Figure 3. Domain organization of Hsp42 (A) and disorder prediction of Hsp42 monomer by IUPred3 (Erdős et al., 2021).

Despite its importance, structural and mechanistic details of Hsp42 function remain limited. Size-exclusion chromatography coupled with multi-angle light scattering has revealed heterogeneous oligomerization states comprising 12–16 protomers (Haslbeck et al., 2004) or 8–14 protomers (Grousl et al., 2018). The only available structural visualization – negative-stain EM followed by single-particle analysis – was published in 2004 and reported Hsp42 oligomers as ~16.5 nm ring-like particles with a central pore of ~ 4 nm diameter (Haslbeck et al., 2004). However, this analysis used image processing techniques developed in 1996 (van Heel et al.), and thus the findings should be interpreted with caution.

Mechanistically, Hsp42 is known to sequester misfolded proteins in near-native conformations via interactions mediated by the PrLD, while the IDD modulates this activity by preventing excessive sequestration (Grousl et al., 2018). However, the determinants of substrate specificity and the mechanisms governing the formation of Hsp42-substrate complexes of different sizes remain unknown. Furthermore, it is unclear whether activation or conformation-dependent changes in Hsp42, otherwise constitutively active, are responsible for defining the architecture of these complexes.

2. Aims

The sequestrase activity of small heat shock proteins is conserved across all domains of life. However, the extent of substrate sequestration varies considerably between species and under different environmental conditions. The molecular determinants and precise mechanisms that define the size and composition of sHsp-substrate complexes remain poorly understood. In this study, I investigate the small heat shock protein Hsp42 from *Saccharomyces cerevisiae* as a model system to elucidate the structural and functional principles underlying sHsp activity – encompassing both holdase and aggregase functions.

The major aspects of my work include:

- Structural analysis of Hsp42 oligomers

Oligomerization and structural dynamics are central to sHsp function. To characterize the oligomeric architecture of Hsp42 and its conformational plasticity, I employ a combination of biochemical and biophysical methods, imaging techniques such as negative-stain and cryo-electron microscopy, as well as computational structural prediction tools.

- Stress-induced activation of Hsp42

Although Hsp42 is constitutively expressed and functionally active under physiological conditions, it does not form large cytosolic inclusions unless cells are exposed to stress. This observation suggests that Hsp42 activity is tightly regulated to prevent unnecessary sequestration of nascent or partially folded proteins under non-stress conditions. I investigate how heat shock, acidic pH, and post-translational modifications such as phosphorylation influence Hsp42 oligomerization and activity.

- Hsp42-substrate complex formation

Hsp42 forms substrate complexes of variable sizes, depending on the nature of the client protein. I examine the substrate-binding regions of Hsp42 using different model substrates and assess the stability of these interactions. In addition, I explore the roles of specific Hsp42 domains and sequence motifs in substrate recognition and binding.

- Substrate recovery from Hsp42-substrate complexes by ATP-dependent chaperones

To understand the handover of sequestered substrates to the disaggregation machinery, I investigate how Hsp42 cooperates with ATP-dependent chaperones, particularly members of the Hsp70 system. I focus on the contribution of individual Hsp42 domains and motifs to this process and assess direct interactions between Hsp42 and yeast Hsp70.

3. Results

3.1. Hsp42 WT structural characterization

To study Hsp42 *in vitro*, I have developed a protocol for purifying Hsp42 from *E. coli* cultures. To enhance solubility, Hsp42 was fused to a maltose-binding protein (MBP) tag. Following the expression, MBP-Hsp42 was isolated via affinity chromatography using dextrin resin, resulting in a single elution peak (Fig. 4A, 4B). The eluted fractions were incubated overnight with the site-specific HRV 3C (PreScission) protease to remove the MBP tag, leaving a residual five-amino-acid scar (PVPGF) at the N-terminus of Hsp42. Subsequent size-exclusion chromatography (Fig. 4C) effectively separated the cleaved MBP tag from Hsp42.

Despite the purification steps, the final Hsp42 preparation consistently contained a co-purifying contaminant of approximately 60 kDa (Fig. 4D). Mass spectrometry analysis identified this contaminant as the septum site-determining protein MinC from *E. coli*. Although MinC has a theoretical molecular weight of 24.8 kDa, its anomalous migration in SDS-PAGE remains unclear. However, previous studies (e.g., Szeto et al., 2001) have reported the formation of MinC dimers, which could explain the observed discrepancy. Importantly, the amount of contaminating MinC was minor. Furthermore, MinC lacks chaperone activity and is therefore unlikely to influence the outcome of subsequent experiments.

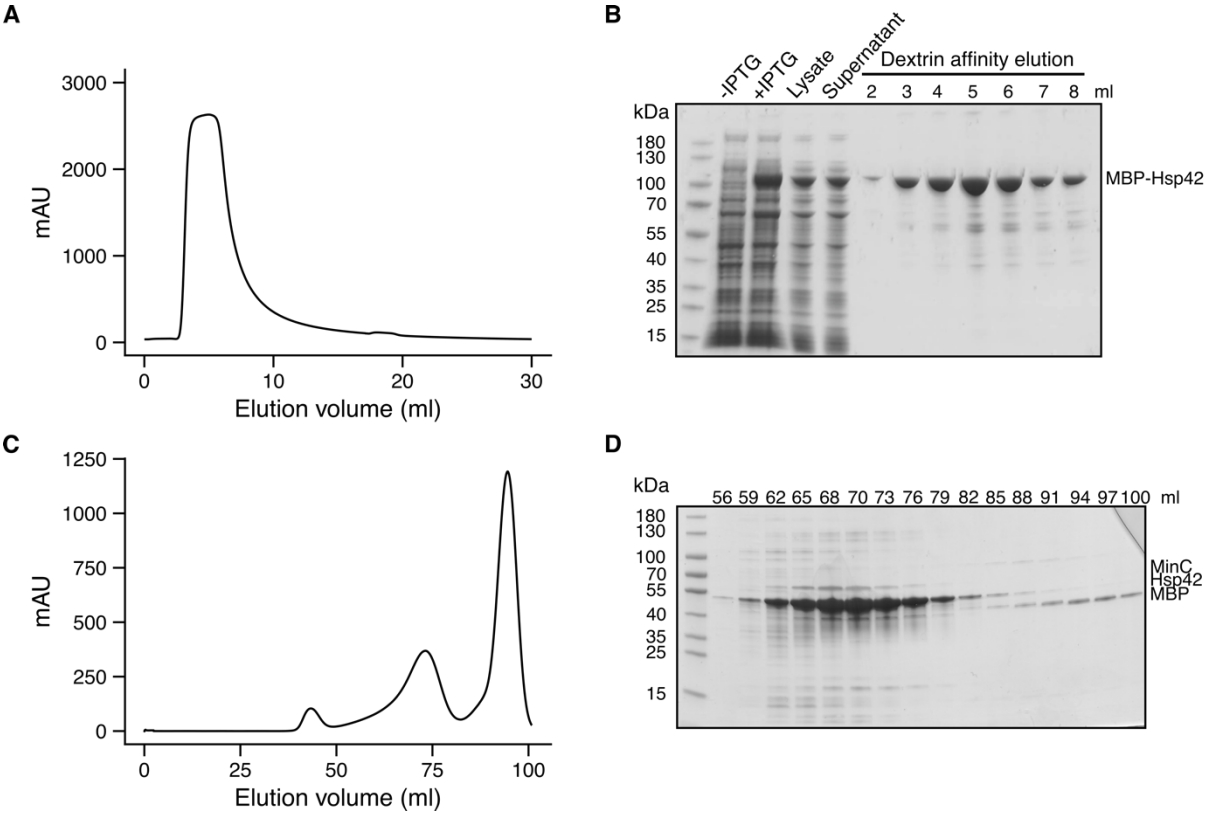

Figure 4. Hsp42 purification. A. Elution chromatogram of the first step of the purification with dextrin resin. **B.** SDS-PAGE analysis of Hsp42 in the cell culture before expression induction (-IPTG), after expression induction (-IPTG), in cell lysate (Lysate), in the cell supernatant applied to dextrin resin (Supernatant), in the eluted from affinity chromatography fractions (2–8 ml). **C.** Size-exclusion chromatogram. **D.** SDS-PAGE analysis of SEC fractions.

3.2. Temperature effects on Hsp42 structure

Although Hsp42 is constitutively active at physiological temperatures, its expression is upregulated in response to heat shock (Haslbeck et al., 2004). Moreover, Hsp42 confers a growth advantage over its small heat shock protein partner Hsp26 under repetitive heat shock conditions (Ungelenk et al., 2016). Additionally, Hsp42 has been shown to sequester misfolded proteins in the cytoplasm into large inclusions upon heat shock (Specht et al., 2011). To investigate Hsp42's thermal stability and potential structural changes upon temperature increase, I employed nano-differential scanning fluorimetry (nanoDSF) combined with dynamic light scattering (DLS) and turbidity measurements to monitor the formation of large aggregates.

NanoDSF detects conformational changes by measuring shifts in the emission spectrum and intensity of intrinsic tryptophan and tyrosine fluorescence, reflecting alterations in their local chemical environment. Hsp42 lacks tryptophan residues but contains 24 tyrosines, 15 of which are located in the PrLD (Fig. 5A). Therefore, fluorescence changes are expected to be dominated by conformational transitions within the PrLD.

The ratio of fluorescence at 350 nm to 330 nm (F350/F330) revealed three distinct conformational transitions (Fig. 5A). The first transition, observed between 25°C and 50°C, was characterized by an increase in F350/F330, suggesting that tyrosines became shielded within a more hydrophobic environment. This reflects local conformational changes that do not lead to protein aggregation, as confirmed by DLS and turbidity measurements (Fig. 5B, 5C). The second conformational transition occurred between 50°C and 62°C, with the mid-transition point at 55.35˚C (SD = 0.8, n = 6), and was marked by a decrease in F350/F330, indicating increased tyrosine exposure to a hydrophilic environment. Despite this transition, no Hsp42 aggregation was detected by DLS or turbidity measurements. The final transition corresponded to tyrosine burial and coincided with the formation of large aggregates, as evidenced by DLS and turbidity measurements. The apparent T_m of Hsp42 determined by nanoDSF is 67.8°C (SD = 0.24, n = 6).

To validate this finding, the melting temperature was determined using an alternative thermal shift assay based on the nonspecific, reversible binding of Sypro Orange dye to hydrophobic residues (Fig. 5D). Sypro Orange fluorescence increases upon binding to hydrophobic amino acids as the protein unfolds or changes its confirmation. Interestingly, the assay showed minimal fluorescence transition up to 40°C, which may support the burial of tyrosine residues, as indicated by nanoDSF. The most pronounced transition occurred between 40°C and 60°C, with an inflection point at 55.6°C (n = 1), coinciding with the second transition observed in nanoDSF and being in line with an increased exposure of tyrosines. The final transition, with a T_{onset} of 64.1°C (n = 1), was marked by a decrease in fluorescence, likely resulting from the uncontrolled interaction of exposed hydrophobic amino acids, ultimately leading to Hsp42 aggregation.

Taken together, the thermal stability analysis demonstrated that Hsp42 is an extremely thermostable protein, with an apparent T_m of 67°C. These findings suggest that temperature induces structural rearrangements within Hsp42. However, the precise nature of these

transitions requires further investigation. Notably, the first transition is of particular interest, as it occurs within the thermotolerance range of *S. cerevisiae*.

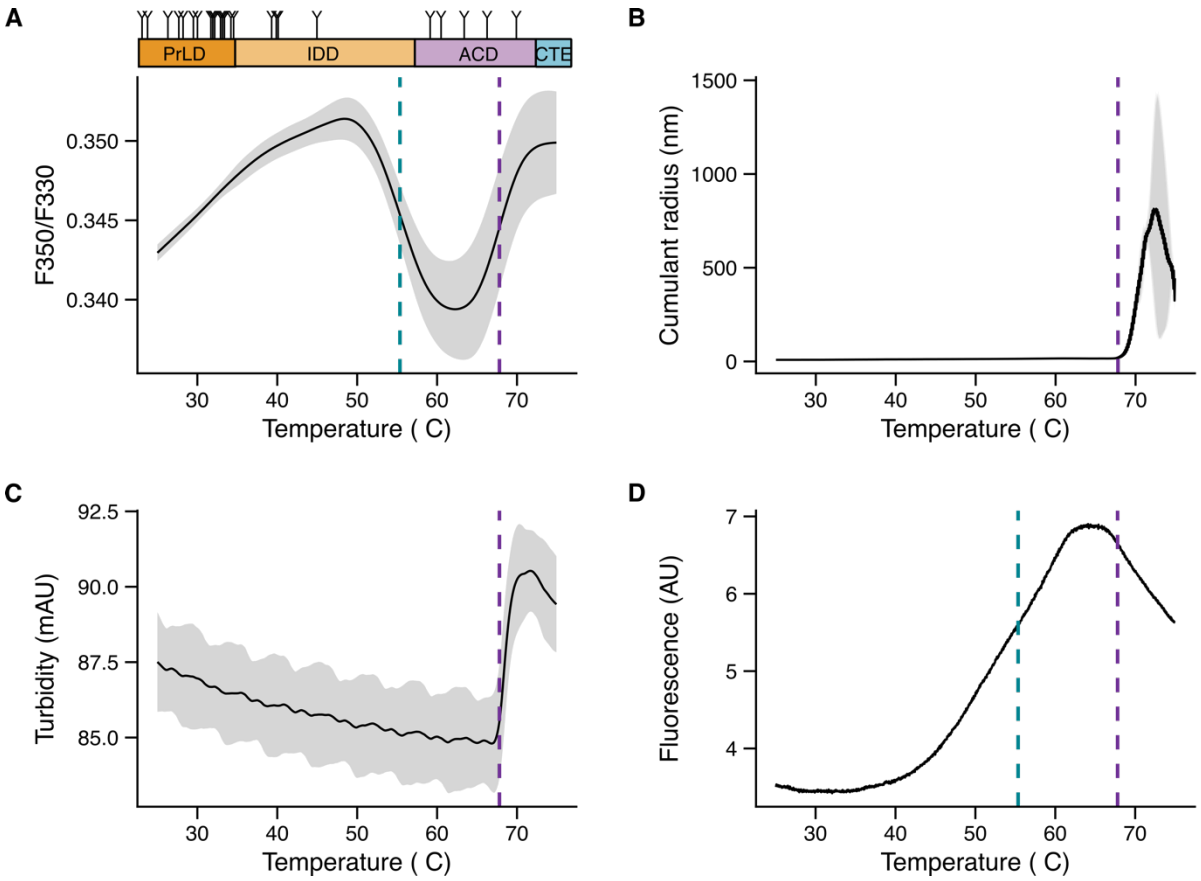

Figure 5. Impact of temperature on Hsp42 structure. All measurements are done at 10 µM Hsp42. Shadow represents standard deviation. **A.** Domain organization and tyrosine distribution within Hsp42. The ratio of fluorescence at 350 nm to fluorescence at 330 nm shows three transition points upon Hsp42 melting. Dashed lines indicate the second and the third transition points (n = 6). **B.** Cumulant radius of Hsp42 at upon melting. The dashed line shows the aggregation onset (n = 6). **C.** Turbidity upon Hsp42 melting. The dashed line indicated the onset of aggregation (n = 6). **D.** Fluorescence of Sypro Orange dye at 465-580 nm upon binding to Hsp42 upon melting (n = 1). The dashed lines indicate transition temperatures determined in the recording F350/F330 in A.

3.3. Hsp42 forms heterogeneous oligomers

A defining characteristic of all small heat shock proteins is their ability to form diverse homo- (or hetero)-oligomers. Oligomerization directly impacts the sHsp activity by determining the substrate binding site position. To investigate the oligomerization of Hsp42, I analyzed it using multiple techniques.

Dynamic light scattering measurements at 10 µM revealed a single peak with a hydrodynamic radius (R_h) of 7.59 nm (SD = 0.04, n = 20) and a polydispersity index (PDI) of 0.14 (SD = 0.01, n = 20) (Fig. 6A). The PDI indicates the degree of size homogeneity among the measured particles. In the case of Hsp42, the observed PDI suggests the presence of multiple oligomeric species coexisting in the solution.

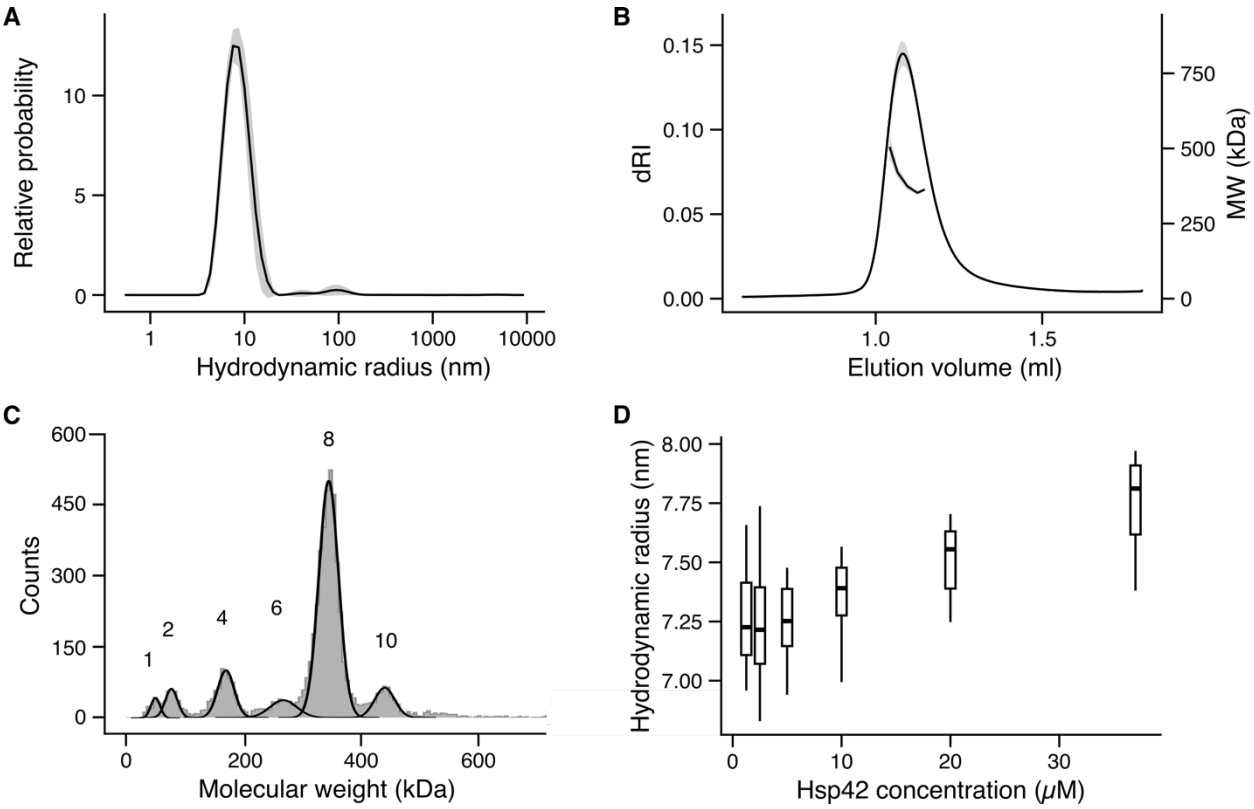

Figure 6. Hsp42 oligomerization. A. Relative probability of hydrodynamic radius distribution in 10 µM Hsp42 sample determined by DLS. Shadow represents standard deviation (n = 2). **B.** Size exclusion chromatography coupled to multi-angular light scattering of eluted 2.75 µM Hsp42. Shadow represents standard deviation (n = 2). **C.** Mass photometry of 100 nm Hsp42. Numbers indicate the number of protomers per Hsp42 oligomers. **D.** Hydrodynamic radius of Hsp42 at different concentrations determined by DLS (n = 20 for each concentration).

To further assess polydispersity, size-exclusion chromatography coupled with multi-angle light scattering (SEC-MALS) was performed using an injected protein concentration of 10 µM. Hsp42 eluted at a final concentration of 2.75 µM (SD = 0.07, n = 2) as a single peak with

a minor right shoulder (Fig. 6B). The molecular mass determined at the half-height of the peak ranged from 350 to 450 kDa, corresponding to oligomers of 8–10 protomers, which is consistent with the previously published 8–14 protomers by Grousl et al., (2018) but smaller than 12–16 protomers determined by Haslbeck et al., (2004).

Mass photometry was employed to precisely identify the oligomeric species by determining their molecular mass distribution. However, a limitation of this method is a low sample concentration required, making direct comparison with SEC-MALS results challenging. Mass photometry measurements at 100 nM showed a distribution of mass peaks in multiples of dimers, with the predominant species being octamers (68%) (Fig. 6C). This result aligns with the SEC-MALS data.

Given the concentration differences across the techniques, I performed DLS measurements of Hsp42 at concentrations ranging from 2.5 to 37 µM (Fig. 6D). The results indicated a slight increase in R_h with increasing concentration, suggesting that Hsp42 forms predominantly octamers and decamers at 2.75 µM, whereas decamers are scarcely present at 100 nM. Therefore, Hsp42 appears to simultaneously form diverse oligomeric states which the equilibrium being concentration-dependent.

3.4. Factors affecting Hsp42 oligomerization

3.4.1. Temperature

Numerous studies have demonstrated that the oligomeric equilibrium of small heat shock proteins can shift in response to various stimuli (Fleckenstein et al., 2015; Shashidharamurthy et al., 2005). Among environmental factors, temperature has been the most extensively studied determinant of sHsp oligomerization. Many sHsps undergo oligomer dissociation upon temperature elevation, which enhances their chaperone activity by exposing key substrate-binding sites within the N-terminal extension (Eisenhardt, 2013). Although Hsp42 is constitutively expressed and active at physiological temperatures (Haslbeck et al., 2004) – up to 30°C in *S. cerevisiae* – it has also been implicated in cellular fitness during recurrent physiological heat stress (Ungelenk et al., 2016).

Conformational changes in Hsp42 oligomers, detected by nanoDSF within a temperature range of 25–50°C, suggest PrLD rearrangement in the absence of aggregation (Fig. 5A). These observations indicate that Hsp42 undergoes structural reorganization, either independently or in conjunction with oligomer dissociation. To further investigate its oligomeric status under increasing temperatures, mass photometry was performed. Due to instrumental constraints, the temperature was increased to a maximum of 35°C. At this temperature, the predominant octameric species dissociated into tetramers (Fig. 7A). This transition was reversible, as tetramers reassembled into octamers upon cooling. The 20-minute incubation between measurements suggests a rapid dissociation/association rate.

Interestingly, analysis of Hsp42's hydrodynamic radius upon mild temperature elevation revealed an apparent contradiction: despite oligomer dissociation into smaller tetramers, the hydrodynamic radius reversibly increased (Fig. 7B). This discrepancy could be explained by

the exposure of disordered N- and C-terminal extensions, which contribute to an overall expansion in molecular dimensions. It should be also mentions that the discrepancy may stem form the concentration difference used in mass photometry (100 nM) and DLS (10 µM).

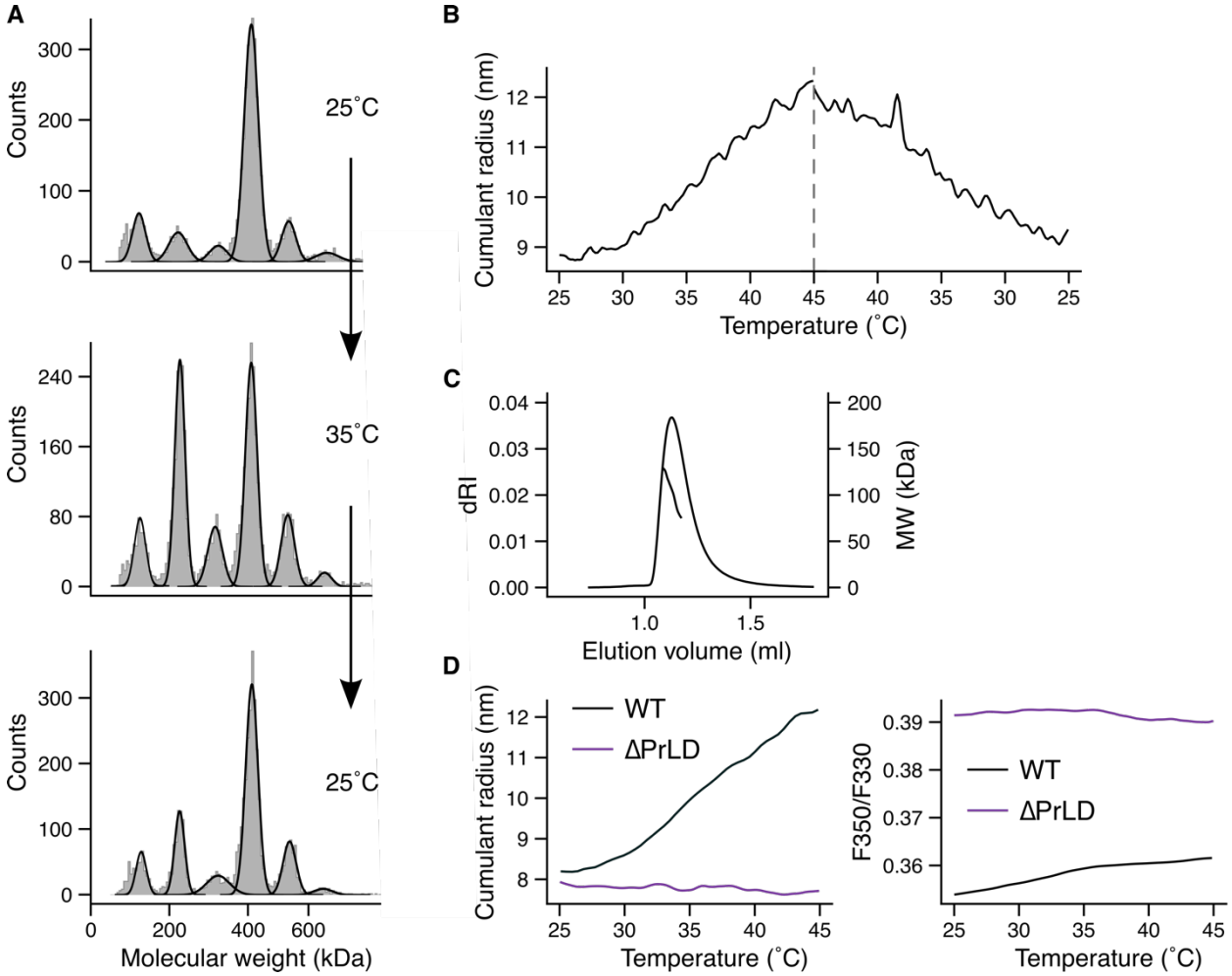

Figure 7. Temperature-dependent oligomerization of Hsp42. A. Mass photometry of 100 nM Hsp42. The sample was measured consecutively at 25˚C, 35˚C, and 25˚C with 20 min incubation in between each measurement. **B.** Cumulant radius of 10 Hsp42 upon mild temperature increase and decrease (n = 1). **C.** Size exclusion chromatography coupled to multi-angular light scattering of the eluted 4.4 µM Hsp42ΔPrLD (n = 1). **D.** Comparison of the cumulant radius and the ratio of fluorescence at 350 nm to fluorescence at 330 nm of Hsp42 wild-type (WT) and Hsp42ΔPrLD upon mild temperature increase (n = 1).

Additionally, nanoDSF analysis indicated increased shielding of the PrLD within a more hydrophobic environment upon temperature elevation up to 50°C (Fig. 5A). To further elucidate the behavior of the PrLD under these conditions, I purified the Hsp42 variant with the deleted PrLD domain. SEC-MALS analysis at 25°C showed that Hsp42ΔPrLD predominantly forms tetramers (120–160 kDa with a protomer 33.2 kDa), implying the involvement of PrLD contacts in high oligomer formation (Fig. 7C). Notably, the temperature-

dependent radius expansion observed in the wild-type protein was abolished in Hsp42ΔPrLD and no conformational changes were detected by nanoDSF (Fig. 7D).

These findings suggest that Hsp42 undergoes oligomer dissociation in response to a mild temperature increase, accompanied by an extension of the PrLD or other disordered regions which become less restrained in smaller oligomers, and contribute to the observed increase in hydrodynamic radius. Despite this extension, tyrosine residues within the PrLD become shielded within a hydrophobic environment, likely engaging in interactions with neighboring PrLD tyrosines.

3.4.2. pH decrease

The findings of Lee et al. (2018) that Hsp42 reversibly sequesters misfolded proteins into Hsp42-associated granules during chronological aging in *S. cerevisiae* raise the question of whether this specific function of Hsp42 is linked to its activation by cytoplasmic acidification, a phenomenon observed in yeast during the stationary phase. To investigate this, the pH-dependent oligomerization of Hsp42 as a potential indicator of its activation was analyzed using analytical size-exclusion chromatography. Hsp42 was buffer-exchanged into solutions of varying pH, with pH 6.0 representing the lowest condition, as this pH decrease has been reported to occur in stationary-phase yeast (Cimprich et al., 1995). SDS-PAGE analysis of the eluted fractions revealed that Hsp42 undergoes a structural transition toward larger oligomeric species (Fig. 8A). The observation that Hsp42 eluted in the void volume at pH 6.0, combined with the diminished intensity of the dimeric band, suggests that Hsp42 may form large aggregates that stick to the resin during size-exclusion chromatography.

To assess the reversibility of these aggregates, the Hsp42 sample was first buffer-exchanged to pH 6.0 and subsequently returned to pH 7.5, followed by oligomer size analysis via size-exclusion chromatography. Notably, Hsp42 fully reverted to its original oligomeric size, demonstrating that the pH-dependent changes in Hsp42 oligomerization are reversible (Fig. 8B).

Taken together, the pH drop effects the Hsp42 oligomerization towards large assemblies. However, the exact natures of these assemblies require further studies.

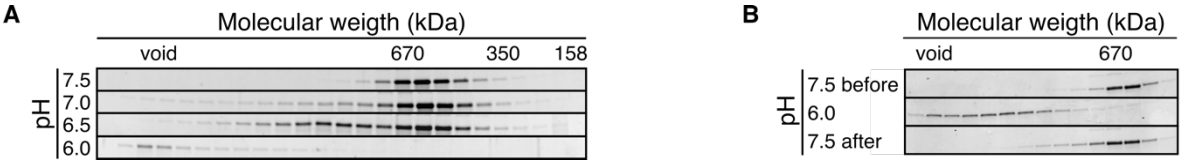

Figure 8. pH-dependent Hsp42 oligomerization. A. SDS-PAGE analysis of size exclusion chromatography fractions of Hsp42 at different pH values. The injected concentration is 10 µM. **B.** SDS-PAGE analysis of size exclusion chromatography fractions of Hsp42 measured consecutively at the pH values 7.5, 6.0, and 7.5. The injected concentration is 10 µM. The pH change was achieved by the buffer exchange with the total incubation time after the buffer exchange and the SEC measurement of 2 hours.

3.4.3. Phosphorylation

Hsp42 undergoes hyperphosphorylation in response to osmotic stress, heat shock, and aging (Ahmadpour et al., 2023). Phosphorylation of Hsp42 has been identified in multiple proteome-wide studies. Analysis of these studies, as compiled in the Eukaryotic Phosphorylation Site Database (EPSD), revealed 21 phosphorylation sites, including 15 serine residues (out of 23), 5 threonine residues (out of 18), and 1 tyrosine residue (out of 24) (Table 1). The common view is that phosphorylation triggers dissociation of oligomers to smaller species.

To test this, the most frequently identified phosphorylated residues were mutated to mimic a constitutively phosphorylated state, followed by purification and *in vitro* characterization. Serine residues were substituted with aspartate, while threonine residues were replaced with glutamate (Table 1, Fig. 9A). In two cases where the modified residues were in close proximity, they were mutated simultaneously, generating the S116D/S118D/S123D and SSS213-215DDD variants. Phosphorylation of consecutive residues can significantly alter local charge distribution, potentially inducing more pronounced conformational changes. In all but one case, the mutations were located in the N-terminal region (including both the PrLD and IDD), consistent with the most of the experimental data on other small heat shock proteins, where phosphorylation in the N-terminus induces structural changes. One mutation, T344D, was located within the ACD.

The experimental analysis of Hsp42 phosphomimetic variants was conducted by Tobias Beschauner – a Bachelor thesis student. The Hsp42 phosphomimetic variants were purified and initially analyzed to assess their oligomerization. All variants, except Hsp42-S232D, exhibited an elution profile in size-exclusion chromatography purification step comparable to the wild type (WT), suggesting a similar oligomerization state (data not shown). In contrast, Hsp42-S232D severely aggregated upon MBP-tag cleavage, indicating that the introduction of a single negative charge at serine 232 disrupts Hsp42 structure. Due to the inability to purify Hsp42-S232D to a sufficient concentration and purity, it was excluded from further characterization.

To further investigate oligomerization, the purified Hsp42 phosphomimetic variants were analyzed using dynamic light scattering, while their thermal stability was assessed by nanoDSF. The hydrodynamic radius of both phosphomimetic and wild-type Hsp42 ranged between 7.5 and 9 nm (Fig. 9B). Although the differences were statistically significant (not shown), variability arising from imprecise concentrations and differences in handling temperatures may have contributed to these variations. Additionally, polydispersity index values ranged from 0.14 to 0.2, indicating the presence of heterogeneous oligomers. Given that the R_h of wild-type Hsp42 is influenced by temperature and concentration, the DLS data suggest that phosphomimetic Hsp42 variants assemble into oligomers similar to the wild type.

Position	Residue	Domain	Number of citations	Hsp42 variant
2	S	PrLD	1	
9	S	PrLD	1	
11	Y	PrLD	1	
18	S	PrLD	1	
21	T	PrLD	1	
81	S	PrLD	3	S81D
116	S	IDD	3	S116D/S118D/S123D
118	S	IDD	4	
123	S	IDD	2	
129	T	IDD	1	
141	S	IDD	1	S141D
182	S	IDD	20	S182D
192	T	IDD	2	
205	S	IDD	3	S205D
213	S	IDD	45	SSS213-215DDD
214	S	IDD	46	
215	S	IDD	49	
223	S	IDD	47	S223D
232	S	IDD	10	S232D
236	T	IDD	6	
344	T	ACD	5	T344E

Table 1. Phosphorylation sites of Hsp42 identified by proteome-based studies. Source: *https://epsd.biocuckoo.cn/View.php?id=EP0025484* (27.03.25). The positions colored grey are mutated to phosphomimetic variants.

The thermal stability analysis of the phosphomimetic Hsp42 variants revealed a melting behavior comparable to that of the wild type (Fig. S1, Fig. 5A). Similar to wild type Hsp42, all phosphomimetic variants exhibited three transitions with the same second mid-transition temperature of 55˚C and the aggregation temperature of 67˚C which was consistent with the wild-type protein, as monitored by DLS (Fig. 9C, 9D).

Overall, the initial characterization of the selected Hsp42 phosphomimetic mutants suggests that phosphorylation at the chosen sites does not alter Hsp42 oligomerization. Although rare, some studies indicate that certain small heat shock proteins can acquire functionality without changes in their oligomeric state (Franzmann et al., 2005).

To assess potential functional effects, the Hsp42 phosphomimetic variants were tested for their ability to suppress the thermal aggregation of luciferase or malate dehydrogenase, as well as their capacity to facilitate the refolding of Hsp42-Luciferase complexes by the Hsp70/Hsp100 chaperone machinery under neutral pH conditions. None of the variants exhibited any differences compared to the wild type in these assays. The corresponding data are presented in Appendix 1.

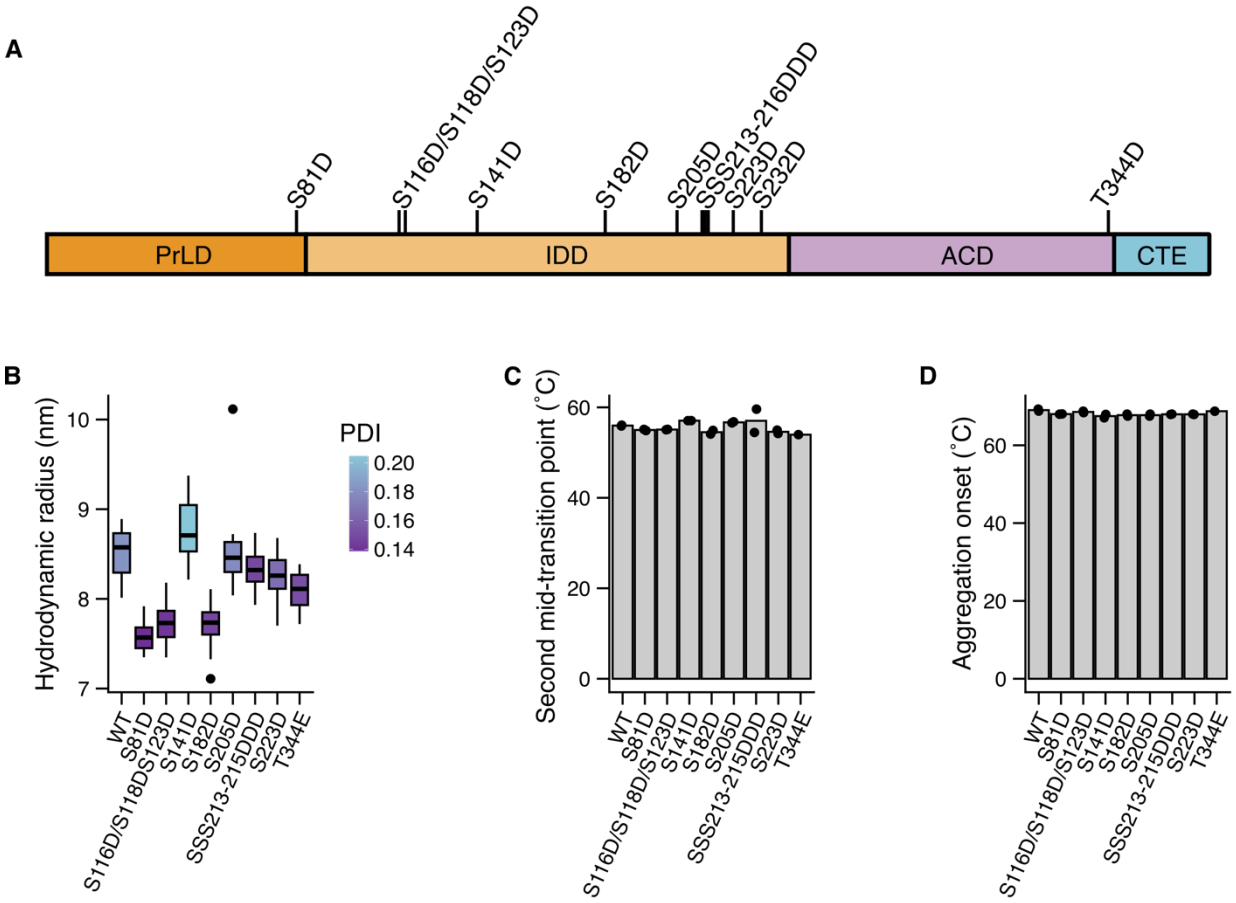

Figure 9. Hsp42 phosphomimetic variants characterization. **A.** Scheme of residues mutated to glutamate (D) or aspartate (E). **B.** Hydrodynamic radius of 10 μM Hsp42 determined by DLS (n = 20) **C.** Second mid-transition point determined by of 10 μM Hsp42 nanoDSF (n = 2). D. Aggregation onset temperature of 10 μM Hsp42 determined by DLS (n = 2).

3.5. Hsp42 subunit exchange

The results presented above demonstrate that Hsp42 exhibits dynamic behavior and can reversibly alter its oligomerization state in response to changes in concentration (Fig. 6D), temperature (Fig. 7A), and pH (Fig. 8A). Previous studies have shown that the dynamics of sHsps are driven by continuous subunit exchange (Delbecq et al., 2015; Aquilina et al., 2005).

To investigate the kinetics of Hsp42 subunit exchange, I developed a Förster resonance energy transfer (FRET)-based assay. A single native cysteine residue (C127) within IDD was selectively labeled with either the donor fluorophore Alexa Fluor 488 (Hsp42-D) or the acceptor fluorophore Alexa Fluor 594 (Hsp42-A) with the 100% labeling efficiency – one fluorophore per each protomer (Fig. 10A). The Hsp42 oligomers had a maximum diameter of 18 nm and, therefore, the distance between the IDDs falls into the FRET distance restrain of 10 nm.

Equimolar concentrations of donor- and acceptor-labeled Hsp42 oligomers were mixed, and the subunit exchange was monitored by recording acceptor fluorescence over time (Fig. 10B). The increase in acceptor fluorescence followed at least a third-order exponential association

function; however, residuals of this fit still exhibited deviations (Fig. 10C). This suggests that the observed exchange mechanism involves more than simple exchange of identical oligomeric units, e.g., dimers, and likely includes simultaneous or sequential subunit association, as well as the incorporation of higher-order oligomeric species (e.g., tetramers or larger complexes).

Interestingly, subunit exchange occurred rapidly. The first exchange event appears to be the primary determinant of the overall kinetics, as the rates of subsequent steps are at least an order of magnitude slower. The fast association rate was concentration dependent which suggests that subunit association is a rate-limiting step. (Fig. 10D).

To investigate subunit dissociation, I first formed heterogeneous oligomers by incubating the equimolar concentrations of Hsp42-D and Hsp42-A (Hsp42-D/A) for one hour. These pre-formed oligomers were then mixed with a five-fold excess of non-labeled Hsp42, and subunit exchange was monitored via the decline in acceptor fluorescence (Fig. 10E). This fluorescence decrease indicates that subunit exchange resulted in the formation of oligomers with a lower labeling density. The dissociation kinetics followed at least a third-order exponential function, suggesting a concurrent and sequential dissociation of main subunits along with other oligomeric species (Fig. 10F).

Surprisingly, the rapid phase of dissociation was also concentration-dependent (Fig. 10G). This observation challenges the conventional view of association and dissociation as separate events, instead suggesting that they occur simultaneously within Hsp42 oligomers: labeled Hsp42 subunits dissociate simultaneously with association of non-labeled Hsp42. The apparent concentration dependence of dissociation may therefore reflect an ongoing dynamic equilibrium between subunit release and re-association. Overall, these findings demonstrate that Hsp42 undergoes rapid subunit exchange, with complete turnover occurring within minutes.

The labeled cysteine is located within the IDD and thus, the observed FRET signal could reflect local conformational changes in the IDD rather than genuine subunit exchange. To test this hypothesis, I engineered the Hsp42-C127A/T254C variant, in which the native cysteine in the IDD was replaced with alanine, and a foreign cysteine was introduced into the α-crystallin domain by substituting threonine at position 254 (Fig. 10H). Structural predictions indicate that this threonine residue is positioned on the exterior of the ACD in the Hsp42 oligomer, with its side chain oriented outward and not involved in stabilizing interactions with other residues, making it an ideal site for labeling (see further chapters). As the fluorophores are attached to the ACD, this FRET pair reports on Hsp42 subunit association and dissociation.

Mass photometry confirmed that the oligomerization profile of Hsp42-C127A/T254C was identical to that of the wild-type protein (Fig. 10I). Kinetic analysis of the association phase revealed that the exchange dynamics of the Hsp42-C127A/T254C variant closely resembled those of the wild-type protein (Fig. 10J, 10K). These findings demonstrate that the FRET signal originates from Hsp42 subunit exchange rather than conformational changes within the IDD.

It remains challenging to assign specific kinetic phases to discrete oligomeric species, particularly given the concentration-dependent shift in oligomeric equilibrium. This experiment may suggest that the smallest exchanging unit is a monomer as FRET may occur between ACDs within the same dimer. Indeed, mass photometry of both wild-type Hsp42 and the Hsp42-C127A/T254C variant detected a minor population of free monomers in solution. However, a distinct pattern of addition of a dimer to pre-existing oligomers and no oligomers with the odd number of protomers (e.i, three or five) would rather suggest a dimer as the main exchanging subunit and FRET occurring between ACDs of two different dimers. Further experiments will be necessary to definitively identify the smallest exchanging unit.

Figure 10. Subunit exchange analysis of Hsp42. A. Position of C127 IDD, which was labelled with a fluorophore donor or acceptor. **B.** Cartoon of the association FRET experiment by mixing Hsp42-D and Hsp42-A at different concentrations and recording the acceptor fluorescence. The shadow indicated standard deviation (n = 3). **C.** Fitting deviation for first-, second-, and third-order exponential association models for FRET fluorescence at different Hsp42-D and Hsp42-A concentrations. **D.** The fast rate of the Hsp42-D and Hsp42-A association was calculated by fitting the raw FRET data into the third-order exponential association model (n = 3). **E.** Cartoon of the dissociation FRET experiment by hetero Hsp42-D/A with the excess of the non-labelled Hsp42 at different concentrations and recording the acceptor fluorescence. The shadow indicated standard deviation (n = 3). **F.** Fitting deviation for first-, second-, and third-order exponential dissociation models for FRET fluorescence at different Hsp42-D/A concentrations. **G.** The fast rate of the Hsp42-D and Hsp42-A dissociation was calculated by fitting the raw FRET data into the third-order exponential dissociation model (n = 3). **H.** Position of cysteine 127, which was mutated to alanine (A), and threonine 245, which was mutated to cysteine and labeled with a fluorophore donor or acceptor (C). **I.** Mass photometry of 100 nM of Hsp42-C127A/T254C. **J.** Cartoon of the association FRET experiment by mixing Hsp42-C127A/T254C-D and Hsp42-C127A/T254C-A at different concentrations and recording the acceptor fluorescence. The shadow indicated standard deviation (n = 3). **K.** The fast rate of the Hsp42-C127A/T254C-D and Hsp42-C127A/T254C-A association was calculated by fitting the raw FRET data into the third-order exponential association model (n = 3). (next page)

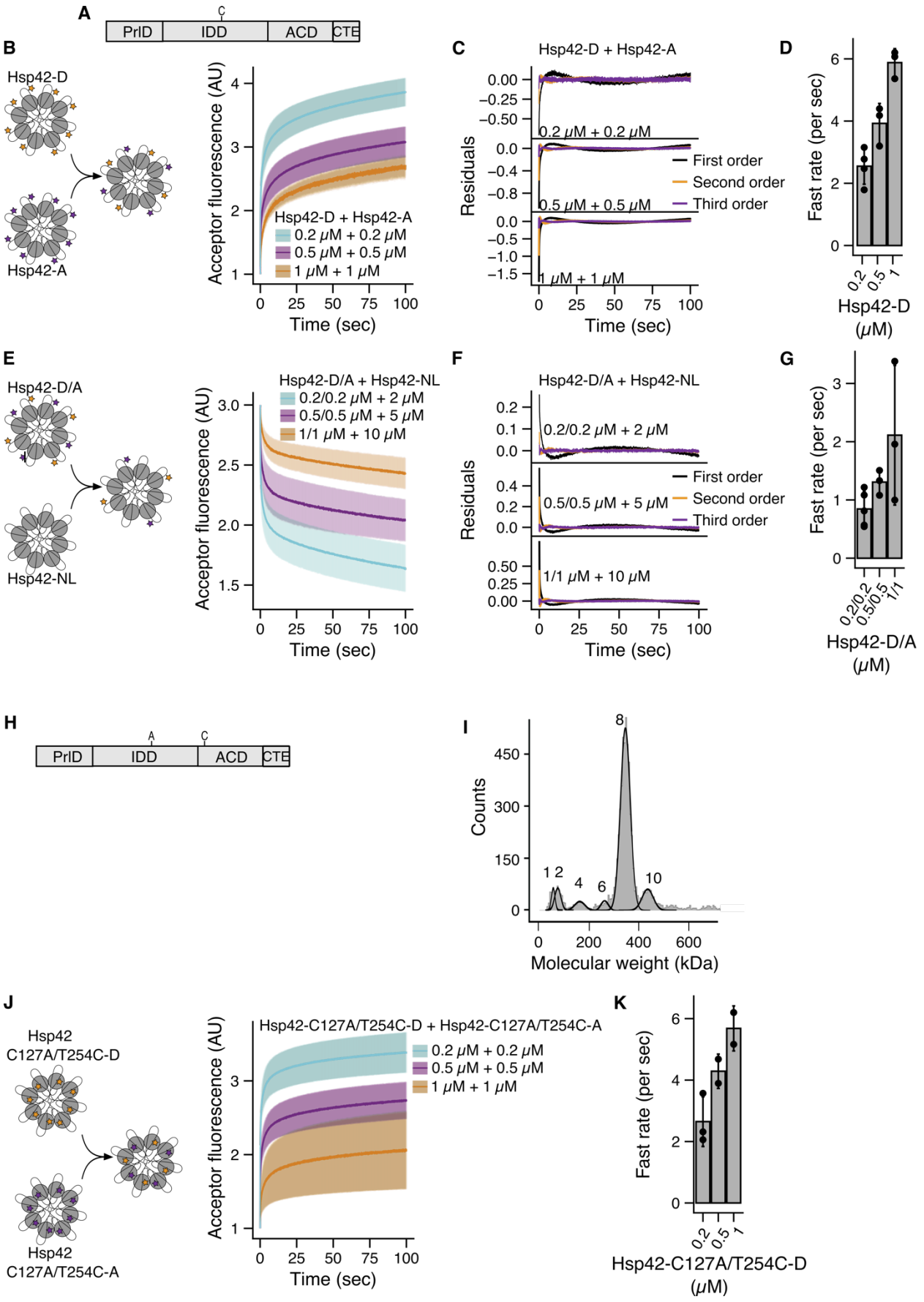
A
C
PrID
IDD
ACD
CTE
B
Hsp42-D
Hsp42-A
Acceptor fluorescence (AU)
Hsp42-D + Hsp42-A
0.2 μM + 0.2 μM
0.5 μM + 0.5 μM
1 μM + 1 μM
Time (sec)
C
Hsp42-D + Hsp42-A
Residuals
0.2 μM + 0.2 μM
0.5 μM + 0.5 μM
1 μM + 1 μM
First order
Second order
Third order
Time (sec)
D
Fast rate (per sec)
Hsp42-D (μM)
E
Hsp42-D/A
Hsp42-NL
Acceptor fluorescence (AU)
Hsp42-D/A + Hsp42-NL
0.2/0.2 μM + 2 μM
0.5/0.5 μM + 5 μM
1/1 μM + 10 μM
Time (sec)
F
Hsp42-D/A + Hsp42-NL
Residuals
0.2/0.2 μM + 2 μM
0.5/0.5 μM + 5 μM
1/1 μM + 10 μM
First order
Second order
Third order
Time (sec)
G
Fast rate (per sec)
Hsp42-D/A (μM)
H
A
C
PrID
IDD
ACD
CTE
I
Counts
1 2
4
6
8
10
Molecular weight (kDa)
J
Hsp42 C127A/T254C-D
Hsp42 C127A/T254C-A
Acceptor fluorescence (AU)
Hsp42-C127A/T254C-D + Hsp42-C127A/T254C-A
0.2 μM + 0.2 μM
0.5 μM + 0.5 μM
1 μM + 1 μM
Time (sec)
K
Fast rate (per sec)
Hsp42-C127A/T254C-D (μM)

3.6. Electron microscopy of Hsp42

Determining the structure of small heat shock protein oligomers remains a significant challenge in the field. While several sHsp structures have been resolved using X-ray crystallography and cryo-electron microscopy (cryo-EM), the success of these methods has often been attributed to the intrinsic tendency of the selected sHsps to have short disordered regions and to form relatively homogeneous oligomers (Kim et el., 1998; Strauch et al., 2022).

To resolve the structure of Hsp42 oligomers, I employed single-particle cryo-EM analysis and optimized experimental conditions to minimize oligomer heterogeneity. Data acquisition was performed in collaboration with Dr. Dirk Flemming (BZH). The computational analysis was conducted by the group of Prof. Dr. Stefan Pfeffer (ZMBH). We explored multiple cross-linking strategies and purification techniques, including size-exclusion chromatography and ultracentrifugation, with the goal of obtaining a homogeneous oligomeric sample. Despite these efforts, achieving the required sample homogeneity proved unsuccessful, precluding the construction of a high-resolution structural model of Hsp42. Consequently, this section provides an overview of the methodologies attempted and the challenges encountered rather than a detailed structural description.

Initial negative-stain electron microscopy revealed circular particles with low internal density (Fig. 11A). However, transitioning to cryo-EM presented immediate difficulties: Hsp42 oligomers exhibited a strong affinity for the carbon layer and failed to remain suspended in vitreous ice. To address this issue, we employed grids coated with an additional carbon layer and performed imaging directly on the carbon support. The oligomers consistently appeared as circular particles, often with a small, distinct density at their periphery (Fig. R8B). Unfortunately, the resulting 3D reconstruction had a resolution of approximately 30 Å, which was insufficient for meaningful structural interpretation.

To improve oligomer homogeneity, we applied the Gradient Fixation (GraFix) method (Stark, 2010), in which Hsp42 oligomers were cross-linked with glutaraldehyde and subsequently separated via ultracentrifugation. While this approach improved sample homogeneity to some extent, the resolution of the reconstructed 3D model remained insufficient (Fig. 11C). We hypothesized that this limitation originated from the choice of cross-linker: glutaraldehyde reacts primarily with lysine residues, but the N-terminal domain of Hsp42, containing both the prion-like domain and intrinsically disordered domain, lacks lysine residues. As a result, while cross-linking stabilized the ACD-CTD core oligomer, the NTD remained flexible, likely contributing to particle heterogeneity.

To overcome this issue, I developed a cross-linking protocol targeting lysine residues (using DSSO) and negatively charged amino acids (using DHSO), which are abundant in the N-terminal extension of Hsp42 (details provided in subsequent chapters). The cross-linked oligomers were further purified via size-exclusion chromatography (Fig. 11D), and a fraction with the highest concentration was selected for analysis. However, negative-stain EM screening revealed a persistent high degree of heterogeneity, preventing further structural characterization (Fig. 11E).

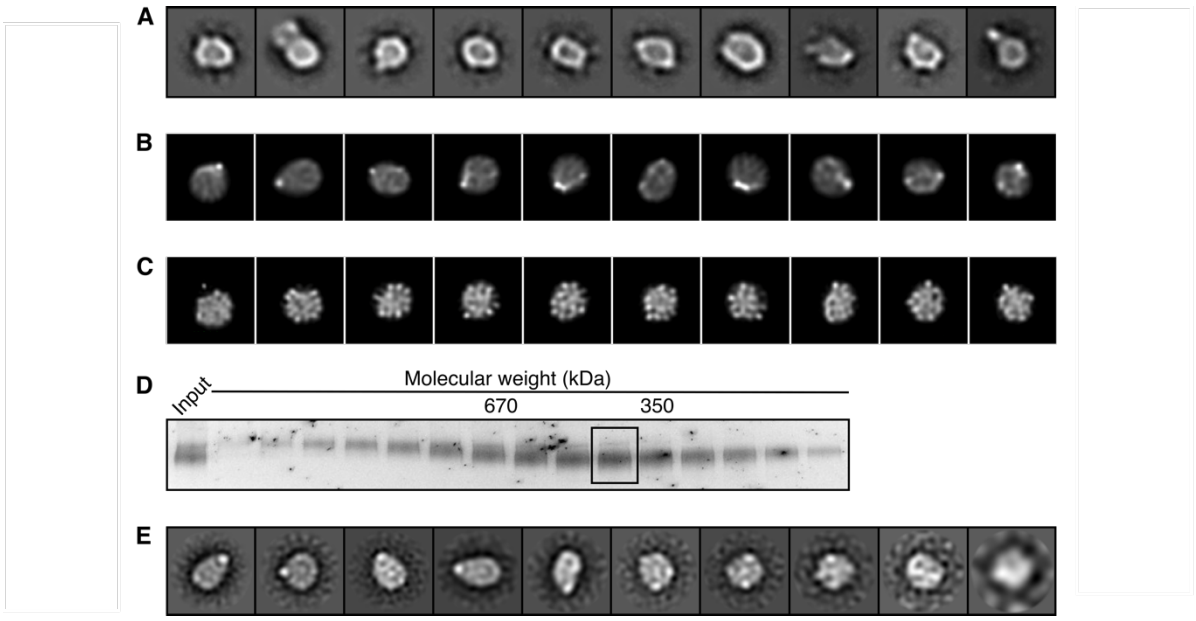

Figure 11. Electron microscopy of Hsp42. **A.** The most populated 2D-class averages of negative-stain EM of Hsp42. **B.** The most populated 2D-class averages of cryo-EM of Hsp42. Images acquired from the carbon surfaces of a grid. **C.** The most populated 2D-class averages of cryo-EM of Hsp42 followed after the gradual fixation protocol. Images were acquired from the carbon surfaces of a grid. **D.** SDS-PAGE analysis of Hsp42 cross-linked with DSSO and DHSO fractions eluted from the size exclusion chromatography. The square indicates the fraction taken for further analysis. **E.** The most populated 2D-class averages of negative-stain EM of Hsp42 followed by cross-linking with DSSO and DHSO, and separation by size-exclusion chromatography.

3.7. Computational prediction of Hsp42 octamer

Recent advancements in computational methodologies, particularly those leveraging artificial intelligence, have significantly enhanced the *ab initio* prediction of macromolecular complex structures. Notably, AlphaFold3 has demonstrated state-of-the-art performance in predicting protein complex architectures, achieving high accuracy (Abramson et al., 2024). Using the default settings on the AlphaFold Server, I modeled the Hsp42 octamer as the predominant oligomeric species. The five predicted models suggested that the structure forms a planar ring made of ACD-CTE dimers. The PrLD was mostly disordered, with an α-helix formed by residue 6-27, primarily located inside the ACD-CTE ring. The IDD was also predicted to contain α-helical regions (residues 141–150 and 87–102), positioned in close proximity to the ACD-CTE ring. The remaining parts of the IDD formed disordered loops that extended outward from the ACD-CTE ring (Fig. 12A).

The Root Mean Square Deviation (RMSD) of Cα atoms between different models was consistently above 7.5 Å. However, this variation was primarily attributed to the intrinsically disordered regions, as the RMSD for the folded ACD domains was below 2.5 Å in the most divergent models, with differences primarily arising from the loops between β-strands. The highest-ranked model was selected for subsequent analysis. All models can be found in the Figure S2.

The predicted model exhibited no steric clashes, with the fraction of disordered regions comprising 52%. The Predicted Template Modeling-score (pTM), which serves as a confidence metric for global structural accuracy, ranged from 0.38 to 0.39 across different protomers. This suggests a low to moderate confidence in the overall fold accuracy. In contrast, the Predicted Local Distance Difference Test (pLDDT) for residues in the ACD domains was 77 (SD = 8.39), indicating a high level of local reliability for these regions (Fig. 12B). While AlphaFold3 confidently predicted the ACD domains, the overall confidence was diminished due to the substantial proportion of intrinsically disordered regions.

To assess the relative positioning of protomers within the octamer, the Predicted Aligned Error (PAE) values were analyzed (Fig. 12C). These values provide insight into the accuracy of the predicted relative positions of different domains (or protomers in the case of the Hsp42 oligomers). The PAE matrix revealed a reasonably high confidence (9.6 Å, SD 5.9) for the relative positioning of ACDs within each dimer, whereas the error for the positioning of ACDs between neighboring dimers was 19.45 Å (SD 3.8). Unsurprisingly, the disordered regions were predicted with an error greater than 20 Å.

AlphaFold predicted oligomeric interactions are consistent with those previously reported in the oligomerization of other small heat shock proteins. In bacteria, archaea, fungi, and plants, dimer formation has been shown to occur via a β6-strand swap of one monomer and its interaction with the β2-strand of a neighboring monomer (Mogk et al, 2019). Interestingly, the PAE values for these regions (residues 297-300 and 247-250) were found to be below the average for the α-crystallin domain, with a mean value of 6.2 Å (SD = 1.29). AlphaFold predicted multiple interactions between these residues, suggesting high confidence in dimer formation via β6-strand swapping (Fig. 12D). Furthermore, the IxI motif within the intrinsically disordered C-terminal extension has been reported to interact with the β4-β8 hydrophobic groove of neighboring dimers, facilitating the assembly of larger oligomers in certain small heat shock proteins (Kim et al., 1998; Delbecq et al., 2012; Yu et al., 2021; Mühlhofer et al., 2021). AlphaFold modeling of Hsp42 predicts interactions between the IxI motif (residues 353–355) and both the β4 strand (residues 269–271) and the β8 strand (residues 324–328), with PAE values of 5.88 Å (SD = 0.97) (Fig. 12E).

Overall, the AlphaFold model predicts a planar ACD ring with moderate confidence, which may be used with caution for subsequent experimental validation. In contrast, the prediction of the intrinsically disordered regions, including the PrLD, IDD, and CTE, exhibited no reliability. Therefore, additional experimental approaches are required to more accurately localize these regions.

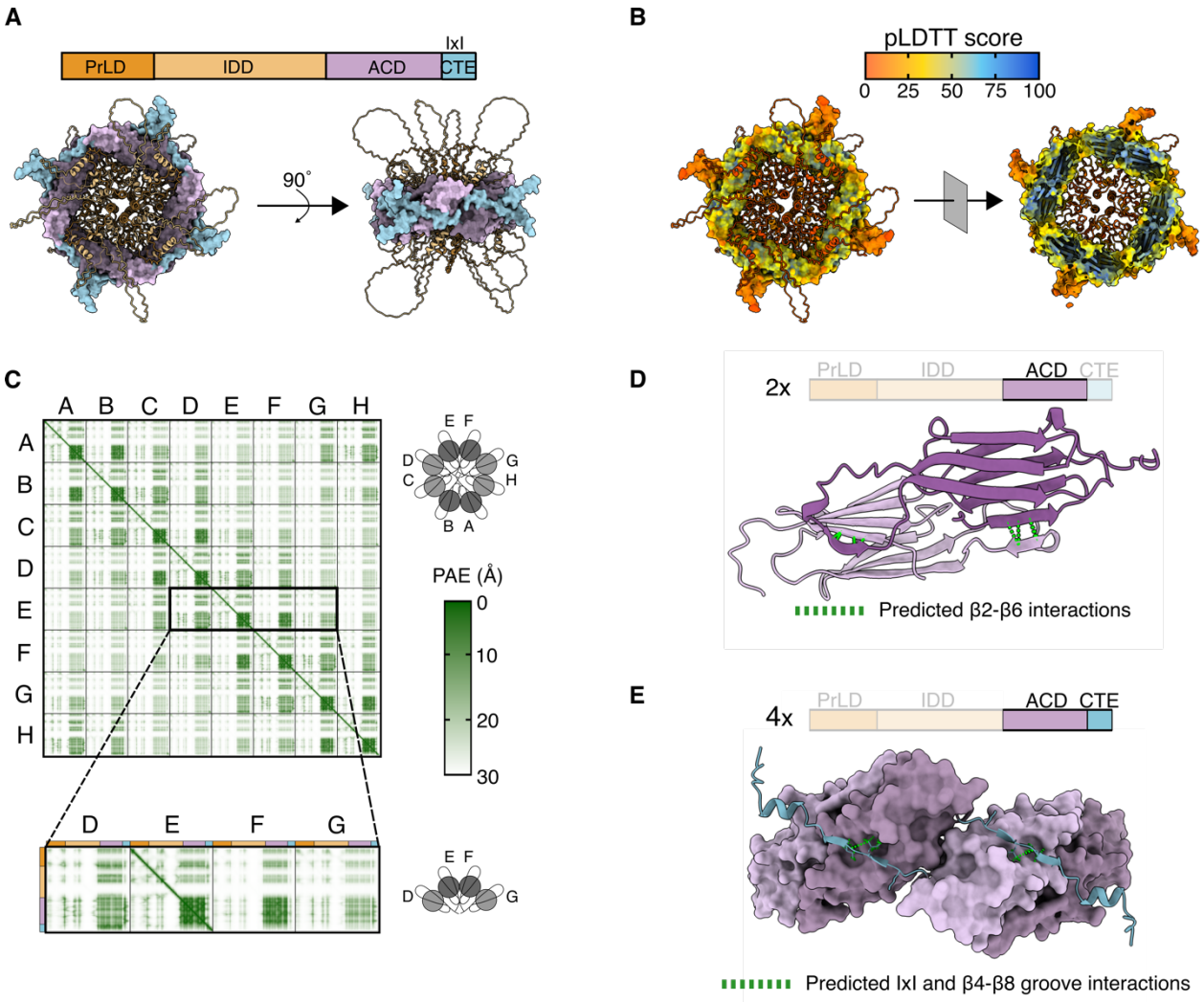

Figure 12. AlphaFold 3 prediction of Hsp42 octamer. A. Color code of Hsp42 domains. Top and side views of Hsp42 octamer. The ACD-CTE ring is depicted as a surface, PrLD and IDD are depicted as ribbon. **B.** Predicted Local Distance Difference Test (pLDDT) of Hsp42 octamer. The top view and the cross-section of the top view. **C.** Matrix of the Predicted Aligned Error (PAE) value of Hsp42 octamers (protomers numbered from A to H). Zoom-in shows the PAE matrix for a tetramer. **D.** Dimer of ACDs with predicted interactions between β2 and β6 strands with a green dashed line. **E.** Tetramer of ACD-CTE with predicted IxI interactions with the β4-β8 grooves strands with a green dashed line. The ACD dimers are depicted as surface, CTE as ribbon.

3.8. Validation of the ACD ring with super-resolution microscopy

To validate the planar ACD ring, which is predicted to consist of a single layer of four ACD dimers in an Hsp42 octamer, I attempted to image ACDs using minimal fluorescence photon fluxes microscopy (MinFlux). MinFlux enables spatial resolution of 2–3 nm, though recent studies have demonstrated resolution capabilities well below 1 nm (Sahl et al., 2024). According to AlphaFold predictions, the ACD-CTD ring has an external diameter of 10–12 nm (Fig. 13A) and is thus suitable for MinFlux.

To introduce a fluorescent dye, the Hsp42-C127A/T254C variant was labeled with Alexa Fluor 647 (hereafter referred to as Hsp42 for simplicity; Fig. 10H). Alexa Fluor 647 has been successfully used in MinFlux imaging in several studies—for example, in Balzarotti et al. (2016), where DNA origami labeled with fluorophores spaced 6 nm apart was imaged. Residue 254C is faced outside the ACD, with an estimated distance between neighboring monomers of ~ 4 nm. Considering the additional ~1 nm size of Alexa Fluor 647, this distance should, in theory, be resolvable by MinFlux. The successful validation of planar ACD arrangement in the Hsp42 octamer should theoretically result in eight dye signals positioned in one plane (± 1.5 nm).

Labeling Hsp42 with Alexa Fluor 647 proved challenging. Following the manufacturer's protocol, labeling efficiency was consistently around 30% after labelling for 2 hours at 25˚C at 150 mM NaCl concentration. Increasing salt concentration, incubation temperature, and time improved the calculated labeling efficiency to 120% based on spectroscopic analysis. However, mass spectrometry revealed that only 41% of Hsp42 molecules were single labeled. A substantial proportion of the molecules were labeled two or three times, and 8% remained unlabeled, and, therefore, the labeling outside the ACD is highly likely (Fig. 13B). This heterogeneity presents a major limitation, as MinFlux localizes fluorophores rather than the protein backbone; precise fluorophore positioning is thus critical. The non-specific labeling renders Alexa 647 unsuitable for precise ACD localization and determination of Hsp42 oligomer organization and size.

As an alternative, I labeled Hsp42 with Alexa Fluor 488, which has been successfully used in the FRET-based assays. Although Alexa Fluor 488 has not been reported for use in MinFlux, it was used for other super-resolution fluorescent microscopy. Mass spectrometry confirmed a labeling profile of ~75% singly labeled molecules (out of a theoretically expected 87%), with 13% double-labeled and no higher-order labeling detected (Fig. 13C). While not ideal, this distribution suggests that many oligomers are correctly labeled in their ACDs, and imaging of multiple oligomers may allow identification of correctly labeled structures.

For imaging, Hsp42 was cross-linked using DSSO to prevent subunit exchange and immobilized on poly-lysine – coated coverslips. MinFlux imaging was conducted in collaboration with Dr. Charlotte Kaplan (BioQuant) and Lucia Svoboda (Bukau lab, ZMBH).

Like all super-resolution techniques, MinFlux relies on fluorophores switching between fluorescent (on) and non-fluorescent (off) states, enabling single-molecule localization. Dye properties – including brightness, on/off duty cycle, photostability, and the number of switching events – are critical for image quality. Because Alexa Fluor 488 molecules in Hsp42

are spaced only 4 nm apart, it is essential that the dye has a sufficiently long off-state (so only one fluorophore per oligomer is in the on-state at any time) and a sufficiently stable on-state for imaging. Unfortunately, Alexa Fluor 488 exhibited a high noise-to-signal ratio, low brightness, and rapid switching, preventing MinFlux image acquisition.

Fluorophore switching behavior can be significantly influenced by the imaging buffer. Standard MinFlux buffers contain an oxygen scavenging system (glucose oxidase and catalase) to reduce photobleaching and blinking by removing dissolved oxygen. Additionally, thiols such as MEA or βME stabilize the off-state by donating electrons. The thiol concentration modulates the on/off ratio: higher concentrations promote longer off-states, minimizing simultaneous emission of several dyes and improving localization. We tested MEA concentrations from 2 to 50 mM and 143 mM βME, but none resulted in sufficient imaging quality, rendering Alexa Fluor 488 unsuitable for this experiment.

Out of curiosity, we also imaged Hsp42 labeled with Alexa Fluor 647 – despite its non-specific labeling outside the ACDs. The same issue persisted: the off/on duty cycle did not permit imaging of individual fluorophores. However, the switching behavior and photon yield per cycle were significantly improved. We were able to image oligomers with a diameter of up to ~20 nm (Fig. 13D), which fits the overall diameter of Hsp42 determined by DLS (Fig. 6A). In rare instances, distinct separation of two fluorophore events measured over time and separated by ~15 nm was observed (Fig. 13E). The preliminary imaging does not validate the planar ACD ring model; however, these preliminary results demonstrate that, with appropriate dye properties, MinFlux has a potential to resolve the ACD ring in Hsp42 and validate the AlpaFold-predicted model.

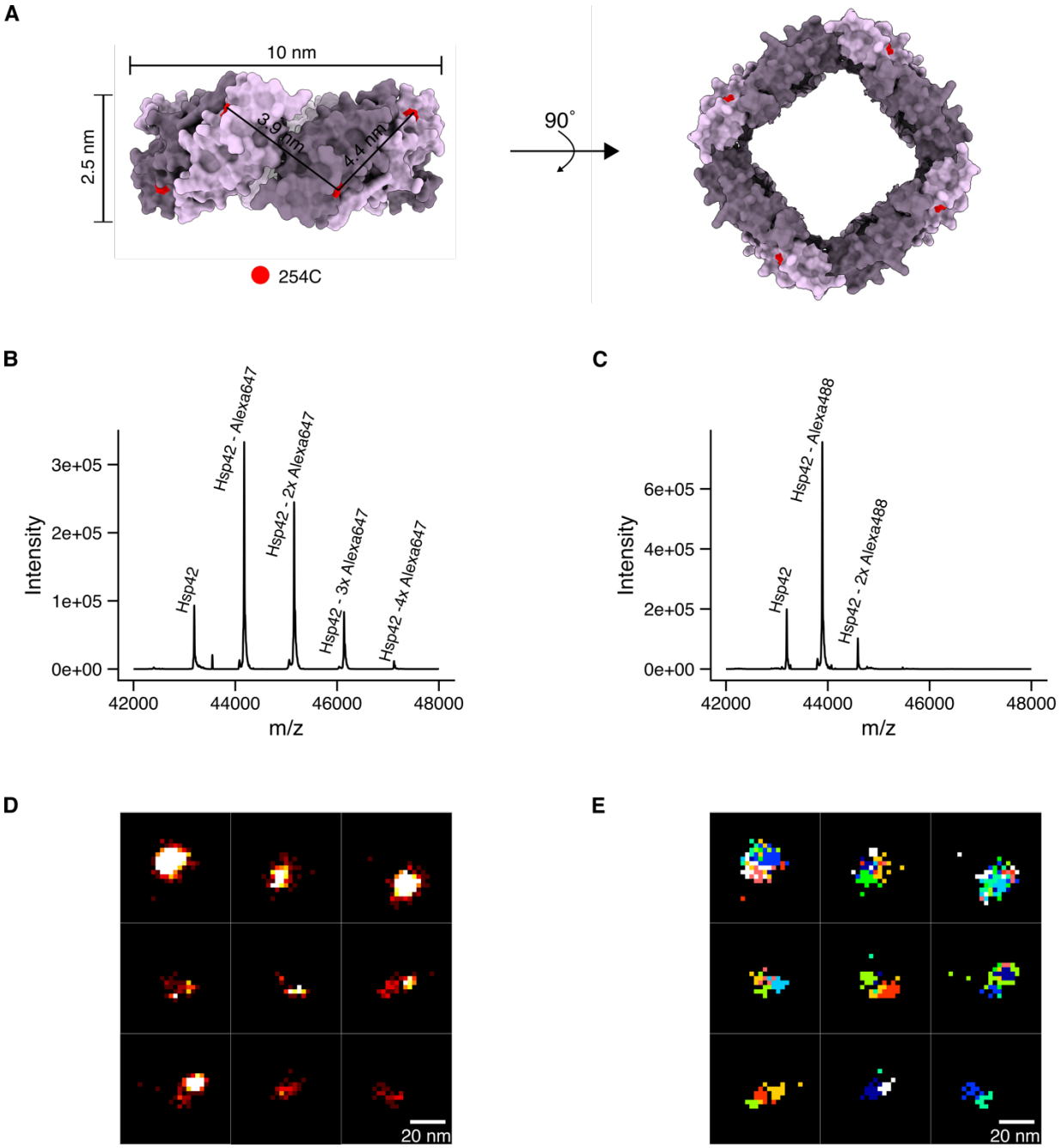

Figure 13. Validation of the planar ACD ring in the Hsp42 octamer using minimal fluorescence photon fluxes microscopy. A. AlphaFold prediction of the ACD ring structure in the Hsp42 octamer. Threonine residues at position 254 were mutated to cysteines and site-specifically labeled with a fluorophore (254C shown in red). **B-C.** Intact mass spectrometry analysis of Hsp42 labeled with Alexa Fluor 647 (B) and with Alexa Fluor 488 (C). **D.** Representative MinFlux images of Hsp42 labeled with Alexa Fluor 647. **E.** Fluorophore events separated in time shown in different colors of MinFlux images from (D).

3.9. Cross-linking mass spectrometry of Hsp42

To validate the predicted AlphaFold model of Hsp42, chemical cross-linking of spatially proximal regions within the octameric assemblies was performed, followed by identification of cross-linked peptides using mass spectrometry. The mass spectrometry was performed by the Core Facility for Mass Spectrometry and Proteomics in ZMBH. To maximize the sequence coverage of Hsp42, two mass spectrometry-cleavable cross-linkers were used – disuccinimidyl sulfoxide (DSSO) and dihydrazide sulfoxide (DHSO). Both reagents are designed to fragment in the gas phase, facilitating the efficient and accurate identification of cross-linked peptides via multistage tandem mass spectrometry (Kao et al., 2010; Gutierrez et al., 2016).

DSSO is a homobifunctional cross-linker that primarily targets the ε-amino groups of lysine residues (K). While the hydroxyl groups of serine (S), threonine (T), and tyrosine (Y) are generally less reactive, the study by Bartolec et al. (2022) demonstrated that approximately 25% of unique cross-linked residue pairs captured by DSSO involve these side chains. Consequently, S/T/Y residues were also considered in the cross-linking analysis of Hsp42. This inclusion is particularly relevant for achieving coverage of the PrLD, which lacks lysines and would otherwise remain uncharacterized (Fig. 14A).

DHSO, similarly homobifunctional, targets the carboxyl groups of aspartate and glutamate residues (D, E). Unlike DSSO, DHSO requires chemical activation of carboxyl groups to facilitate nucleophilic attack by the hydrazide moiety. For this purpose, 4-(4,6-dimethoxy-1,3,5-triazin-2-yl)-4-methylmorpholinium chloride (DMTMM) is used as an activating agent, which is compatible with proteins under physiological pH conditions (Gutierrez et al., 2016). DHSO enables the targeting of negatively charged patches across the Hsp42 sequence, including but not limited to regions within the IDD and CTE (Fig. 14A). Therefore, the combined use of DSSO and DHSO permits a more comprehensive structural interrogation of Hsp42 oligomers.

Despite the theoretical coverage afforded by the distribution of reactive residues, two short segments in PrLD and IDD (residues 62-108 and 135-172) lacked suitable cleavage sites for trypsin digestion, resulting in the absence of detectable peptides from this region in the control not cross-linked sample (Fig. 14A). Alternative proteases, including ProAlanase and chymotrypsin, failed to significantly improve digestion efficiency. As a result, cross-links within these segments could not be detected by mass spectrometry.

Cross-linking of Hsp42 with DSSO yielded large, homogeneous high-molecular-weight oligomers, whereas cross-linking with DHSO in the presence of varying ratios of the activating agent DMTMM resulted in a heterogeneous distribution of cross-linked oligomers, as assessed by SDS-PAGE analysis (Fig. 14B). Importantly, the oligomeric state of Hsp42 was not altered by chemical cross-linking, with the octamer remaining the predominant species, as confirmed by mass photometry. A minor increase in apparent molecular weight was observed, consistent with the contribution of the cross-linker mass (Fig. 14C).

In-solution mass spectrometric analysis of cross-linked Hsp42 identified 73 unique cross-links for DSSO and 20 for DHSO. Mapping these cross-links onto the Hsp42 octamer model posed

a challenge in distinguishing between intra- and inter-molecular interactions, given that Hsp42 forms a homo-octamer.

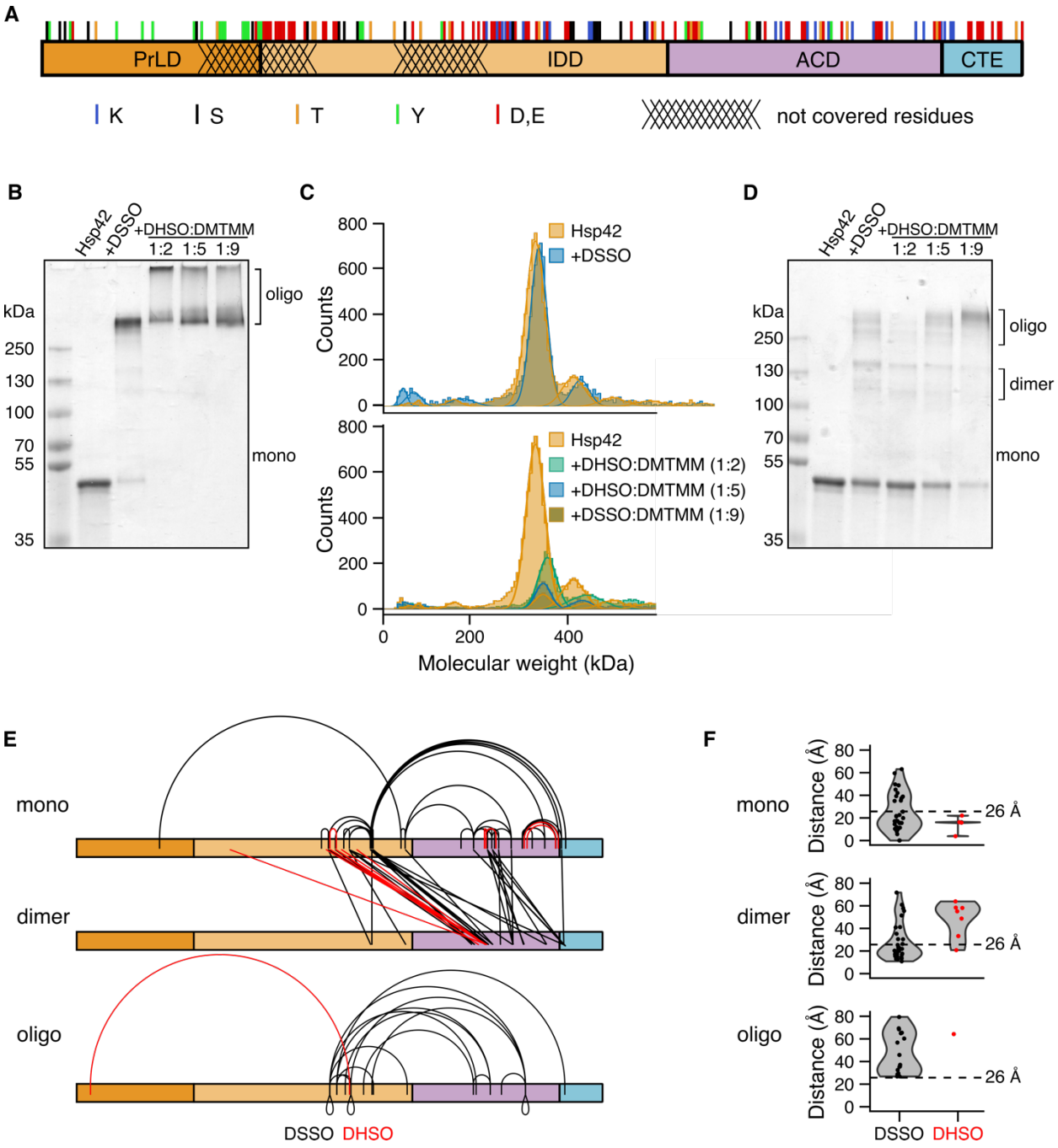

Figure 14. Cross-linking mass spectrometry of Hsp42. A. Distribution of reactive residues accessible for cross-linking with DSSO or DHSO. The grid highlights peptide regions that are not cleaved by trypsin and are therefore not detectable by mass spectrometry. **B.** SDS-PAGE analysis of cross-linked Hsp42 to achieve full cross-linking efficiency. **C.** Mass photometry of Hsp42 cross-linked with DSSO or DHSO:DMTMM at different ratios. Hsp42 concentration 100 nM. **D.** SDS-PAGE of cross-linked Hsp42 at lower concentrations of cross-linkers and a shorter incubation time. **E.** Scheme of the cross-links assigned to monomers, dimers, and higher oligomeric species. Created by XiView online tool (Combe et al (2024). **F.** Quantification of Cα-Cα distances between cross-linked residues mapped on the predicted AlphaFold model. The dashed line indicates a theoretical permissible Cα-Cα distance of DSSO and DHSO.

To address this, cross-linking was repeated under milder conditions – using lower concentrations of cross-linkers and shorter incubation times – to favor the formation of cross-linked monomers and dimers (Fig. 14D). The cross-linked dimers likely appeared as two distinct bands on SDS-PAGE, which may reflect differences in the extent and position of cross-linking, and consequently, variations in electrophoretic mobility. The bands corresponding to monomeric and dimeric species were excised from the gel and subjected to mass spectrometric analysis, following the same workflow as for the in-solution samples. This approach makes possible the identification of intramolecular cross-links within monomeric species, as well as intermolecular cross-links within dimers. Cross-links that were not detected in the monomeric or dimeric gel bands but were present exclusively in the in-solution cross-linked sample were attributed to higher-order oligomeric cross-links (Fig. 14E).

The identified monomeric, dimeric, and oligomeric cross-links were mapped onto the AlphaFold model of Hsp42 octamer as a predominant species. The distances between cross-linked residues were calculated and used as an additional criterion to assess whether the cross-links support the predicted oligomeric model. Each cross-linker has a defined spacer arm length – the distance between its two reactive groups – which imposes spatial constraints on the cross-linked amino acids. The cross-linker DSSO has a spacer arm length of approximately 10.1 Å, while DHSO spans around 12.4 Å. Given that amino acid side chains can adopt various conformations due to flexibility around side chain dihedral angles (rotamers), Cα-Cα distances were measured, as backbone atoms are more spatially constrained and their relative positions more reliably predicted. The permissible Cα-Cα distance ranges are approximately 20–26 Å for both DSSO and DHSO.

Monomeric cross-links fell into two categories: those that satisfied the distance constraint were located within the ACD, while longer cross-links were identified within the IDD or between the intrinsically disordered IDD and either the ACD or the CTE (Fig. 14F, 15A). The observation that all cross-links within the ACD met the distance constraint indicates that this domain is accurately predicted. In contrast, the failure of cross-links within disordered regions to meet the constraint was expected, as these regions lack a stable conformation and are likely to occupy a larger spatial volume than represented in the structural model. Nevertheless, transient interactions in these flexible regions can still be captured by chemical cross-linking.

Similar to the monomeric cross-links, dimeric cross-link distances exhibited a bimodal distribution. Cross-links that fell within the allowed distance were primarily located between ACDs (Fig. 14F), whereas those exceeding the distance threshold originated from connections between the IDD and the ACD, and likely do not represent the true spatial position of the IDD within the dimer. Dimeric cross-links involving the ACD were found both within individual dimers and between adjacent dimers, suggesting that ACDs from neighboring dimers are in close proximity (Fig. 15B). Additionally, several cross-links were detected between the β2 strand of one monomer and the vicinity of the β6-strand of the adjacent monomer within a single dimer, consistent with the formation of a dimer via β6-strand swapping.

The IxI motif and the β4-β8 groove contain relatively few reactive residues. However, the predicted interaction between the IxI motif and the β4-β8 groove was experimentally supported by the identification of a cross-link between K350 in the CTE of one dimer and K283, which are located in close proximity to the IxI motif and the β4-β8 groove of the

neighboring dimer, respectively (Fig. 15D). This provides direct evidence that the IxI motif was predicted correctly by AlphaFold and contributes to the formation of higher-order oligomers.

All cross-links identified in higher-order oligomers exceeded the distance constraint. In almost every case (15 out of 18), at least one of the cross-linked residues was located within the IDD or the PrLD (Fig. 14D). Despite this, a substantial number of cross-links were observed between the IDD and the ACD. In all oligomeric states, the majority of cross-links were formed between IDD loops and the top surface of the ACD-CTE ring (Fig. 15C). No cross-links were detected between the IDD loops and either the outer surface or the interior of the ring, despite the presence of reactive residues in both regions. Several cross-links were identified between the extreme C-terminus of the IDD and the interior of the ACD (Fig. 15C), corresponding to the transition point between the IDD and the start of the ACD sequence.

Cross-linking mass spectrometry identified only two cross-links involving the PrLD (Fig. 15E). The first cross-link was detected between S60 in a disordered region of the PrLD and K233 in the IDD. This cross-link is categorized as monomeric and satisfies the distance restraint (15.9 Å) (Fig. 14E). Both residues are located in close proximity to the ACD surface inside the ACD-CTE ring. Notably, the interaction of the NTE with the inner surface of the ACD in the *M. jannaschii* 24-mer Hsp16.5 was previously reported by Miller and Reichow (2025). This supports the possibility that S60 is indeed located inside the ring. The second cross-link was detected between D12, located in the α-helix of the PrLD, and E195, which resides in an IDD loop situated outside the ACD-CTE ring. This cross-link did not meet the distance restraint, suggesting that the extreme N-terminus of the PrLD may in fact extend outside the ACD-CTE ring.

Taken together, cross-linking mass spectrometry of Hsp42 oligomers validated the predicted formation of ACD monomers and ACD dimers through the β6 strand swapping. Additionally, cross-links between ACDs in neighboring dimers suggest that the tetramer adopts a planar arrangement, rather than a stacked positioning, with the IxI motif facilitating further dimer-dimer interactions. The long stretch of IDD (residues 160–213), which appears as a loop in the AlphaFold model, was confirmed to localize on both the top and bottom surfaces of the ACD ring. Its flexibility is supported by the identification of cross-links spanning distant regions of the ACD ring. Nevertheless, the IDD loop does not appear to extend to the ring's exterior, as no cross-links with the outer surface of the ACD-CTE ring were detected. Experimental validation of the full extent of the PrLD, which is predicted to reside within the ACD-CTE ring, remains inconclusive due to the limited number of cross-links involving this domain. Only the region surrounding S60 appears to be localized within the ACD-CTE ring. However, the precise spatial arrangement of the remaining portions of the PrLD within the oligomer remains unresolved.

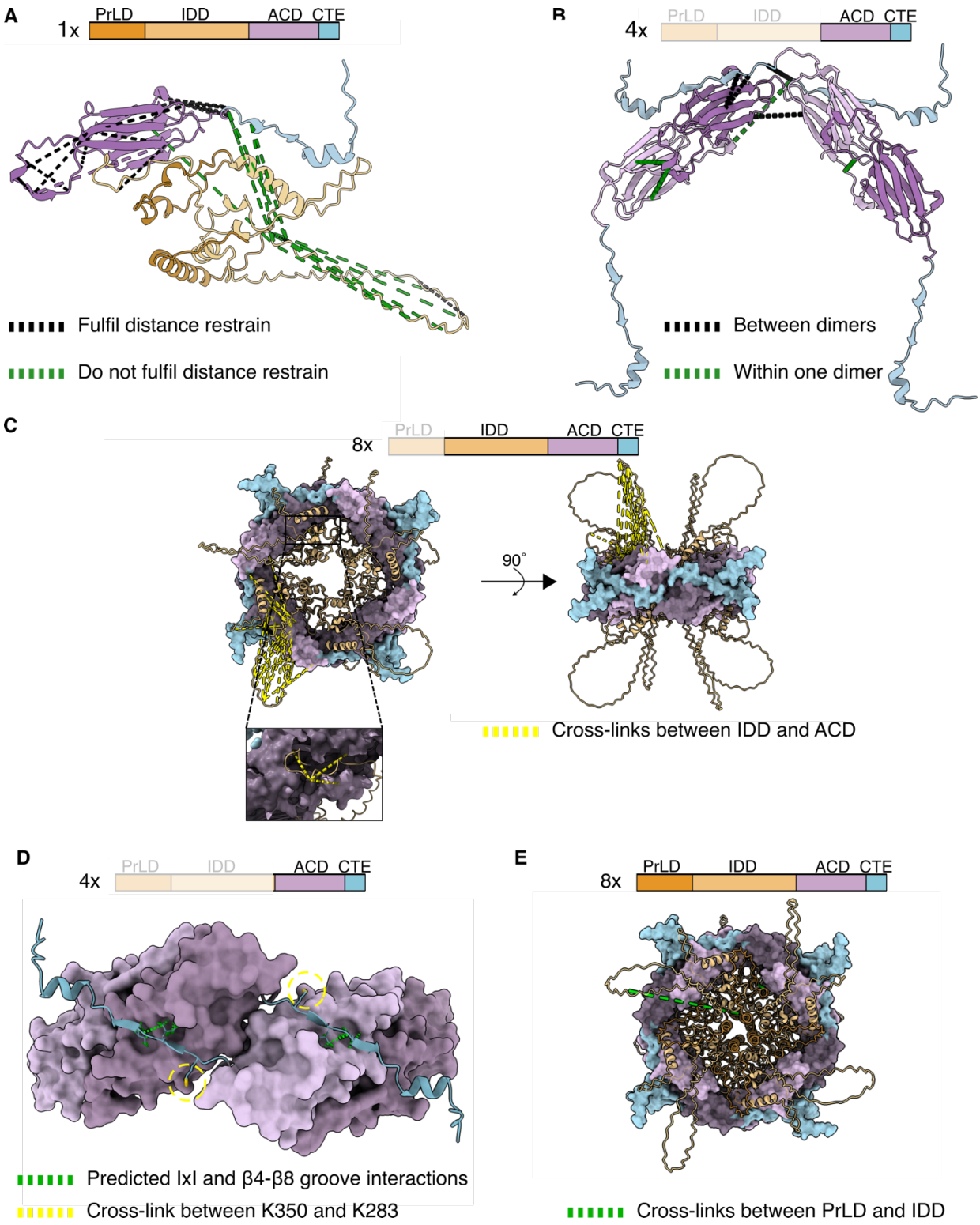

Figure 15. Cross-links identified by mass spectrometry on the Hsp42 octamer AlphaFold model. A. Hsp42 monomer with cross-links detected in the monomeric band of the incomplete Hsp42 cross-linking. **B.** Tetramer of ACD-CTE with cross-links detected in the dimeric bands of the incomplete Hsp42 cross-linking. **C.** Top and side views of Hsp42 octamer (without PrLD) with cross-links between IDD and the ACD-CTE ring. Zoom-in on the cross-links located inside the ACD-CTE ring interior. The cross-links for only one IDD are depicted for better visualization. The ACD-CTE ring is depicted as surface, IDD as ribbon. **D.** Tetramer of ACD-CTE. Predicted (green) and experimental (yellow) interactions between the IxI motif and the β4-β8 groove vicinity. ACD dimers are depicted as surface, CTE as ribbon. **E.** Top view of Hsp42 octamer and two cross-links between PrLD and IDD in green.

3.10. Limited proteolysis of Hsp42

The PrLD contains the substrate-binding site and must, therefore, be accessible to misfolded client proteins. However, the PrLD is predicted by AlphaFold to locate within the ACD–CTE ring. If this is the case, it remains unclear how the PrLD could interact with misfolded substrates. Given that the internal dimension of the ring is predicted approximately 6x3 nm and appears densely occupied by the predicted PrLD and IDD regions, it is plausible that only very small substrates could be accommodated within this space. Two scenarios could explain this: (1) the AlphaFold prediction inaccurately places the PrLD inside the ring, and in reality, it is positioned externally, or (2) the PrLD becomes transiently exposed through subunit exchange, thereby enabling interaction with misfolded proteins.

Since the former crosslinking approach did not allow to determine the positioning of the PrLD, I assessed the accessibility of the PrLD by limited proteolysis coupled with mass spectrometry (LiP-MS). Hsp42 was incubated with a low concentration of Proteinase K for a short duration. Proteinase K is a broad-spectrum serine protease that cleaves peptide bonds adjacent to the carboxyl groups of aliphatic and aromatic amino acids. With 168 potential cleavage sites in Hsp42, the enzyme theoretically cleaves every 2–3 residues, enabling comprehensive sequence coverage. However, the brief incubation time allows targeting and cleavage of only surface-exposed and/or disordered regions, whereas buried or folded domains typically require prolonged exposure for digestion. One limitation of this approach for structural analysis is that Hsp42 oligomers undergo continuous subunit exchange, which may transiently expose regions that are otherwise protected from proteolytic cleavage. As a result, limited proteolysis probes Hsp42 in its native, dynamic state rather than capturing only the rigid oligomeric conformation.

Hsp42 was incubated with Proteinase K for 30 minutes, with samples taken at 5-minute intervals (Fig. 16A). The full-length Hsp42 was progressively digested into smaller fragments over time. To identify the digested and protected regions, peptides were analyzed and quantified in the non-digested sample (0 minutes) and after 5- and 15-minutes using mass spectrometry. To enable mass spectrometry analysis, all Hsp42 fragments were additionally digested with trypsin. Consequently, two types of peptides were generated: fully-tryptic peptides, with both termini cleaved by trypsin, and semi-tryptic peptides, where one terminus resulted from Proteinase K cleavage during limited proteolysis and the other from trypsin cleavage. No semi-tryptic peptides were expected in the 0-minute control sample. The fully tryptic peptides for residues 1–25, 62–108, and 132–179 were not detected in any of the samples likely due to the lack of trypsin cleavage sites (Fig. 16B).

To quantify changes in fully tryptic peptides upon Proteinase K treatment, the relative abundance of these peptides in the 15-minute sample was divided by their abundance in the 0-minute control sample. For more clear data representation the relative peptide abundances were presented as $\log_2$ values and therefore the ratio as $\log_2(15\ \text{min}) - \log_2(0\ \text{min})$ (Fig. 16C). Fully tryptic peptides with the ratio below 0 were digested by Proteinase K, indicating they are located in surface-exposed and/or flexible regions of the Hsp42 oligomer. These peptides were predominantly mapped to IDD consistent with the AlphaFold prediction and the cross-

linking mass spectrometry data collaborating that IDD is disordered and exposed on the outer surface of the oligomeric ring.

Fully tryptic peptides with the ratio above 1 exhibited increased abundance following Proteinase K treatment, implying that these peptides were initially protected from trypsin cleavage in the control sample but became accessible upon proteolysis. This suggests their structural shielding was altered by Proteinase K, potentially exposing previously buried tryptic sites. These peptides were primarily located in PrLD (residues 25–61), as well as across ACD and CTE.

Although the residues 25-61 in PrLD are disordered, they are partially internalized in the AlphaFold model and shielded by IDD (Fig. 16D). Additionally, S60 within this region was previously identified in cross-linking experiments as cross-linking with the residue S233 in IDD, located within the ACD–CTE ring. This cross-linking may further account for the protection from Proteinase K digestion. Taken together, these findings suggest that residues 25–61 of the PrLD are internalized within the Hsp42 oligomer and remain shielded even during subunit exchange.

As expected, the ACD was poorly digested by Proteinase K, consistent with its compact, folded structure. Surprisingly, the CTE was also resistant to Proteinase K proteolysis despite its surface-exposed position in the model. This resistance may be explained by its interaction with the β2-β4 groove of the neighboring ACD as well as the predicted interactions with other CTE regions in the AlphaFold oligomeric model.

The qualitative analysis of semi-tryptic peptides presents several challenges. First, semi-tryptic peptides were detected throughout the entire Hsp42 sequence, indicating that even structurally protected and folded regions of the oligomer are at least partially susceptible to Proteinase K cleavage. Second, regions containing fully tryptic peptides that are initially protected but become exposed over time may subsequently be cleaved by Proteinase K, thereby contributing to the pool of semi-tryptic peptides. Third, the significantly larger number of semi-tryptic peptides resulted in substantial overlap across their sequence, making it difficult to draw definitive conclusion.

For the semi-tryptic peptides, I calculated the ratio of the $\log_2$ relative peptide abundance at 5 minutes versus the $\log_2$ relative peptide abundance at 15 minutes ($\log_2$(5 min) – $\log_2$(15 min)) (Fig. 16E). The ratio below 0 indicates that the abundance of these peptides increased over time, suggesting that the corresponding regions are more accessible to Proteinase K, consistent with localization to IDD regions, as observed in previous experiments.

Taken together, the most significant insight from the limited proteolysis data is that large parts of the IDD are exposed, while residues 25–61 of the PrLD are buried within the Hsp42 oligomer. However, the structural positioning of the remaining regions of the PrLD still remains unresolved.

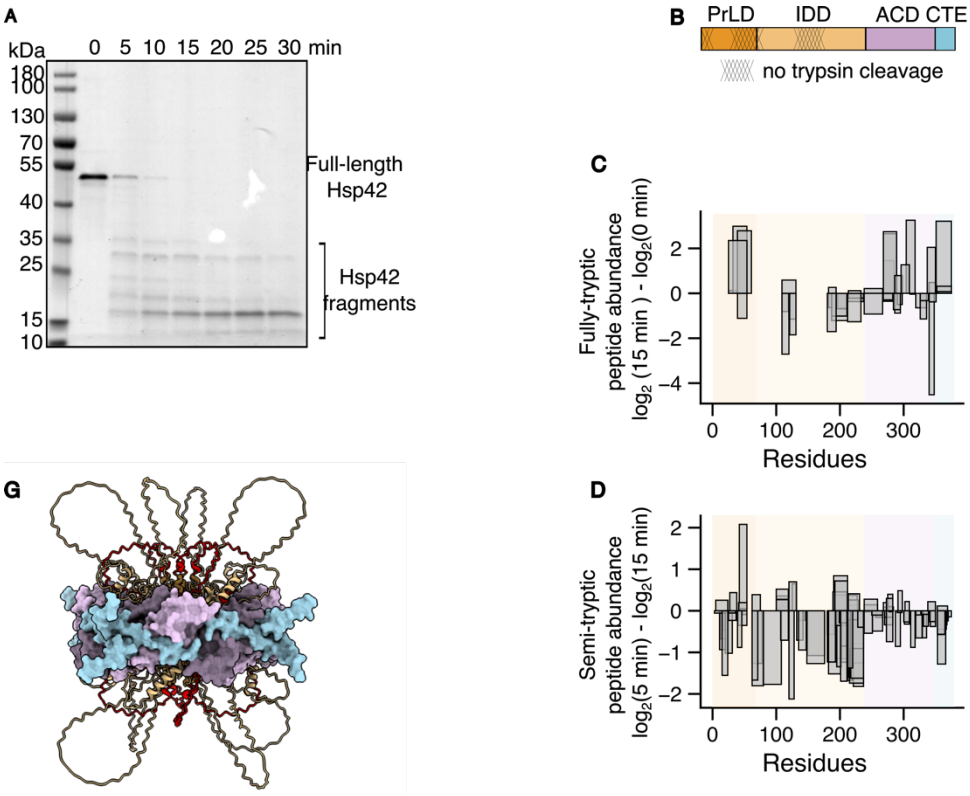

Figure 16. Limited proteolysis of Hsp42. A. SDS-PAGE analysis of Hsp42 subjected to limited proteolysis by Proteinase K over time. **B.** Schematic representation of Hsp42 domain organization and regions lacking fully tryptic peptides, due to the absence of trypsin cleavage sites. **C.** Ratio of fully-tryptic peptides abundance identified after 15 minutes of Proteinase K digestion to their abundance in the untreated control sample at 0 minutes calculated as a ratio of log2 values. Each bar represents a single peptide. **D.** AlphaFold prediction of Hsp42 octamer with residues 25-61 in PrLD in red. **E.** Ratio of semi-tryptic peptides abundance identified after 15 minutes of Proteinase K digestion to their abundance in the untreated control sample at 0 minutes calculated as a ratio of log2 values. Each bar represents a single peptide.

3.11. Hsp42 functional characterization

To characterize the ability of purified Hsp42 to interact with misfolded proteins and form complexes, I conducted a series of light scattering assays using various client proteins. Firefly luciferase (Luci) is a thermolabile protein that unfolds and forms large light-scattering aggregates at increased temperatures. An equimolar concentration of Hsp42 completely suppressed the light scattering signal of aggregated luciferase at 37°C (Fig. 17A). DLS analysis confirmed that this suppression resulted from the formation of small Hsp42-Luci complexes with a hydrodynamic radius of 35 nm (SD = 0.62, n = 2) (Fig. 17B). Similarly, Hsp42 partially suppressed the aggregation of an alternative temperature-sensitive substrate, citrate synthase, at 45˚C (Fig. 17C). However, the suppression was less efficient, and the addition of a molar excess of Hsp42 did not further suppress aggregation. These findings demonstrate that Hsp42 functions as a classical small heat shock protein, preventing protein aggregation by forming small Hsp42-substrate complexes.

Miller et al. (2015) demonstrated that Hsp42 facilitates the formation of cytosolic inclusions upon heat shock, while Ungelenk et al. (2016) reconstituted the formation of large Hsp42-substrate complexes *in vitro* using thermolabile malate dehydrogenase (MDH) as a model substrate. MDH is slowly unfolded at 41 °C without causing significant light scattering. However, in the presence of Hsp42, the resulting Hsp42–MDH complex becomes large enough to scatter light measurably. I reproduced the formation of large MDH-Hsp42 complexes at sub-stoichiometric and equimolar concentrations of Hsp42, as evidenced by increased MDH light scattering in the presence of Hsp42 (Fig. 17D) and the detection of complexes measuring 100 nm in radius by DLS (Fig. 17E). However, at a molar excess of Hsp42, MDH aggregation was not suppressed in contrast to finding by Ungelenk et al. (2016); instead, even larger MDH-containing complexes were formed. This discrepancy may be attributed to the highly negatively charged FLAG-tag fused to Hsp42 in the study by Ungelenk et al. or differences in buffer conditions. Additionally, I established a light scattering assay using Lysozyme (Lys). The structure of Lysozyme is stabilized by four disulfide bonds, which are reduced by a treatment with a reducing agent and lead to Lysozyme unfolding and aggregation, which can be monitored by recording light scattering. Lysozyme was reduced with TCEP and its aggregation was even accelerated in the presence of Hsp42 at 30˚C (Fig. 17F). Collectively, these results demonstrate that, in addition to forming small Hsp42-substrate complexes, Hsp42 is also capable of assembling into large, turbid complexes with its clients.

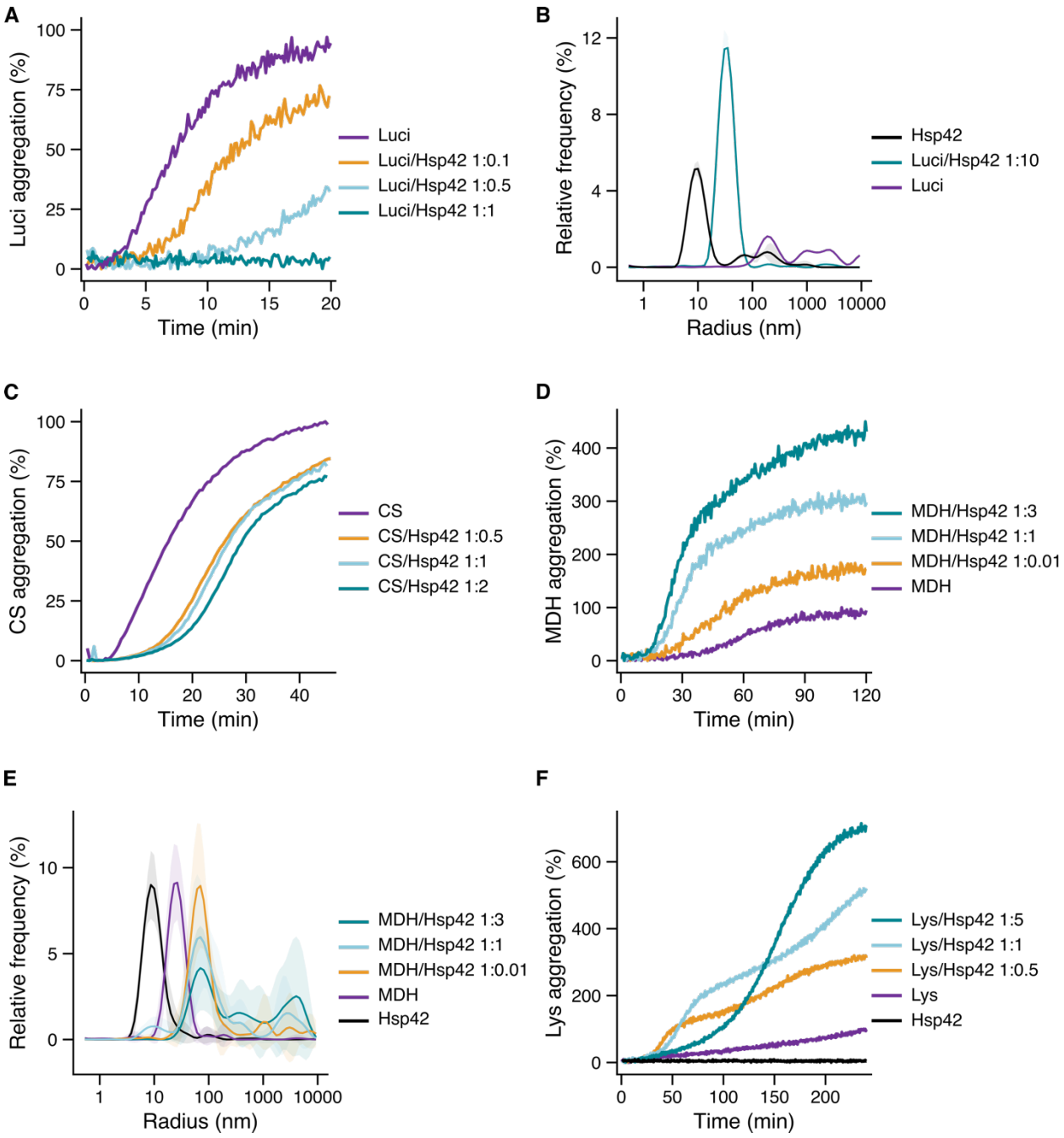

Figure 17. Hsp42-substrate complex formation with various substrates. A. Light scattering percent of Luci aggregation in the absence of presence of Hsp42 at different Luci/Hsp42 ratios at 37˚C. Turbidity of Luci aggregates was set as 100%. **B.** Relative frequency of hydrodynamic radii of Luci in the absence of presence of 10-fold molar excess of Hsp42 after 20 minutes incubation at 43˚C measured by DLS (n = 2). **C.** Light scattering percent of CS aggregation in the absence of presence of Hsp42 at different CS/Hsp42 ratios at 45˚C. Turbidity of CS aggregates was set as 100%. **D.** Light scattering percent of MDH in the absence of presence of Hsp42 at different MDH/Hsp42 ratios at 41˚C. Turbidity of MDH aggregates was set as 100%. **E.** Relative frequency of hydrodynamic radii of MDH in the absence or presence of different MDH/Hsp42 ratios after 60 minutes incubation at 41˚C measured by DLS (n = 2). **F.** Light scattering percent of Lys in the absence of presence of Hsp42 at different Lys/Hsp42 ratios at 30˚C. Turbidity of Lys aggregates was set as 100%.

3.12. Conformational flexibility is required for Hsp42 activity

The dynamic behavior of sHsps, including oligomer dissociation and subunit exchange, is considered a key prerequisite for their chaperone activity, as it enables the exposure of substrate-binding sites required for the recognition of misfolded client proteins. To investigate the role of subunit exchange in Hsp42 function, I chemically cross-linked Hsp42 oligomers using DSSO and assessed their ability to suppress the thermal aggregation of Luciferase. As anticipated, cross-linked Hsp42 lost its chaperone activity and was no longer able to prevent Luciferase aggregation (Fig. 18). This contrasts with certain other small heat shock proteins, such as human HSPB5, which also undergo subunit exchange but retain their chaperone activity in preventing client protein aggregation, even after non-specific amine–amine cross-linking (Aquiline et al., 2003; Johnson et al., 2020). It is important to note, however, that the loss of Hsp42 function may also result from the inhibition of conformational flexibility beyond subunit exchange, as DSSO cross-links are distributed across the entire Hsp42 sequence. Nevertheless, these results support the conclusion that Hsp42 does not interact with substrates as a rigid oligomer but requires conformational rearrangements for its chaperone function.

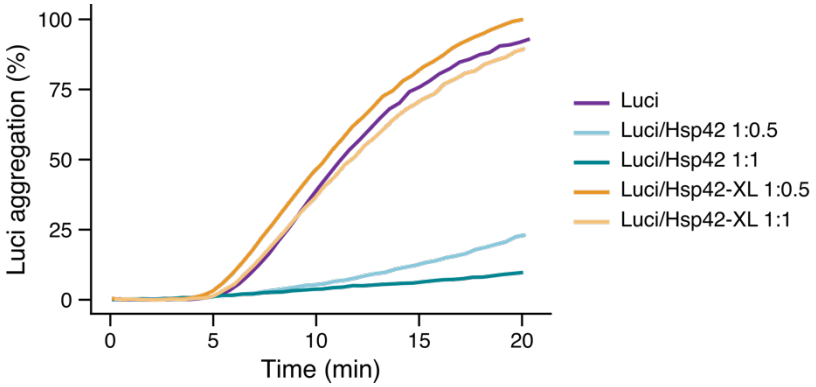

Figure 18. Light scattering measurements of Luci aggregation at 37 °C in the absence or presence of Hsp42 at varying Luci/Hsp42 molar ratios. Hsp42-XL refers to Hsp42 chemically cross-linked with the DSSO cross-linker. The turbidity of Luci aggregates in the absence of chaperone was set to 100% and used as a reference.

3.13. Activity of Hsp42 at different temperatures

Many small heat shock proteins undergo structural rearrangement and activation upon heat shock (Veinger et al., 1998; Haslbeck et al., 1999; Bova et al., 2002). Hsp42 dissociates into tetramers and undergoes conformational changes within its prion-like domain over a physiologically relevant temperature range of 25–45 °C (Fig. 7A, 7D), raising the question of whether these processes are functionally coupled.

To address this, I employed an established model of protein aggregation using insulin (Ins) as a substrate at various temperatures. Insulin relies on three disulfide bonds to maintain its native structure; reduction of these bonds by dithiothreitol (DTT) leads to protein unfolding and subsequent aggregation. Insulin aggregation was monitored by recording light scattering in the presence and absence of Hsp42 at 25, 35, and 45 °C (Fig. 19).

At 25 °C, Hsp42 effectively suppressed insulin aggregation, forming small complexes unable to scatter light. Notably, increasing the temperature revealed a shift in Hsp42 activity: at 35 and 45 °C, Hsp42 promoted the formation of larger, light-scattering complexes with Insulin.

This suggests that elevated temperature induces structural changes in Hsp42 that are necessary for the formation of higher-order complexes with client proteins. It is also worth mentioning that at higher temperatures, Insulin aggregates more rapidly, which may affect its interaction with Hsp42.

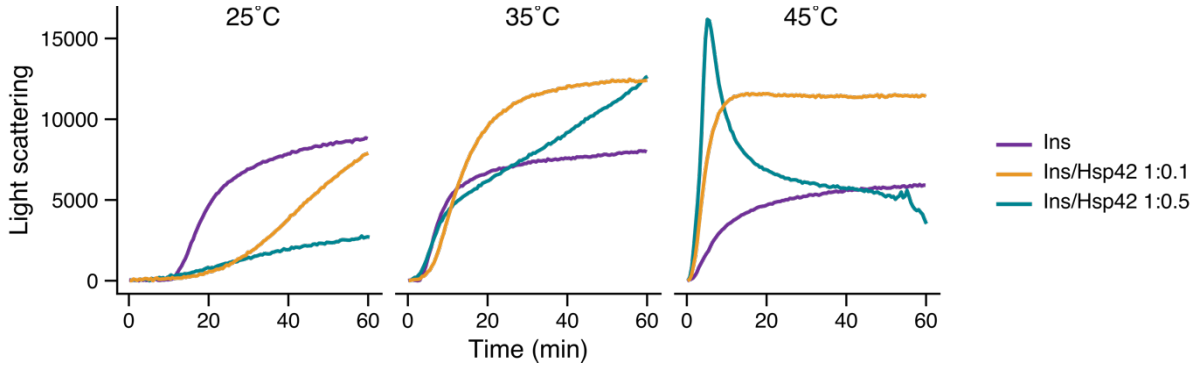

Figure 19. Hsp42 complex formation with Insulin at different temperatures. Insulin aggregation was triggered with DTT in the absence or presence of different ratios of Insulin to Hsp42.

3.14. Activity of Hsp42 at lower pH values

To test the hypothesis that the increased size of Hsp42 assemblies at pH 6.0 correlates with enhanced chaperone activity (Fig. 8A), I evaluated the ability of Hsp42 to suppress substrate aggregation under these conditions by monitoring light scattering. Initially, Luciferase was used as a model substrate at pH 7.5 in Fig, 16A. However, its aggregation behavior varied substantially across pH values, rendering it unsuitable for reliable comparisons at pH 6.0 (Fig. 20A).

Citrate synthase, a well-established substrate for assessing small heat shock protein activity at acidic pH (as low as 5.8; Fleckenstein et al., 2015), was therefore employed as an alternative. Nonetheless, CS also exhibited pH-dependent differences in aggregation between pH 7.5 and pH 6.0 (Fig. 20B). Despite these differences in CS behavior, Hsp42 did not demonstrate enhanced chaperone activity at pH 6.0 compared to pH 7.5. Moreover, Hsp42 alone at pH 6.0 scattered light.

Taken together, the Hsp42 assemblies formed at pH 6.0 are sufficiently large to scatter light on their own, rendering light scattering-based aggregation assays unsuitable under these conditions. Furthermore, an alternative substrate must be identified whose intrinsic aggregation behavior is not significantly influenced by pH, to allow reliable assessment of pH impact on Hsp42 chaperone activity.

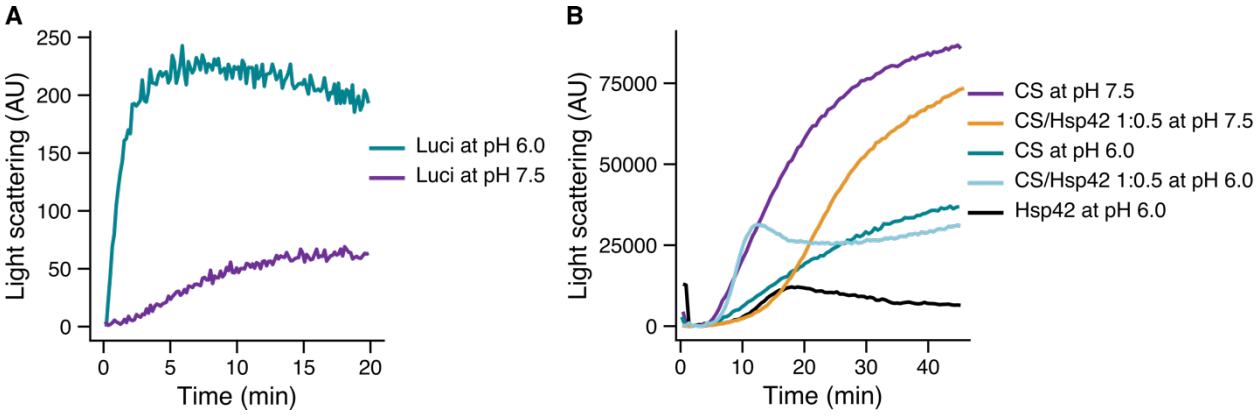

Figure 20. pH-dependent activity of Hsp42. A. Light scattering of Luci aggregation at different pH values at 37˚C. **B.** Light scattering of CS aggregation in the presence or absence of Hsp42 at different pH values at 45˚C.

3.15. Hsp42 substrate binding sites

The prion-like domain of Hsp42 has been shown to mediate substrate binding and chaperone activity, as its deletion results in a complete loss of function both *in vivo* and *in vitro* (Grousl et al., 2018). Grousl et al. further demonstrated that replacing all tyrosine residues in the PrLD with serines abolishes its sequestration function *in vivo*. Additionally, using a cross-linking approach, they identified tyrosine 11 within ≤10 Å of the substrate in Hsp42-MDH complexes formed upon MDH unfolding, highlighting its direct involvement in substrate interaction.

Tyrosine 11 is located within a hydrophobic patch spanning residues 10–17. Furthermore, four additional hydrophobic patches within the PrLD have yet to be investigated for their role in substrate binding (Fig. 21A). To assess these regions, along with the contribution of other Hsp42 domains to substrate binding, I performed cross-linking experiments using DSSO and DHSO as cross-linkers. Hsp42-substrate complexes were first formed by incubating Hsp42 with Luciferase at 37°C for 15 minutes or with malate dehydrogenase (MDH) at 41°C for 60 minutes, followed by cross-linking for 2 hours at 25°C (Fig. 21B, 21D). These experimental conditions resulted in distinct Hsp42-substrate assemblies – smaller complexes with Luciferase and larger ones with MDH – which were selected to investigate whether different substrate binding sites are engaged depending on the client protein, and whether the specific binding interface influences the size of Hsp42-substrate complexes. Light scattering analysis confirmed that the extended cross-linking period did not induce nonspecific or excessive aggregation of either substrate (Fig. 21C, 21E). The cross-linking sites were subsequently identified by mass spectrometry, enabling the mapping of potential substrate-binding regions. The DHSO cross-linker proved ineffective in this experiment, as no cross-links were detected. Therefore, only the results obtained with DSSO are presented below.

The analysis revealed a number of cross-linking sites with luciferase (Fig. 21F). The sites in Luciferase span the entire sequence were crosslinked. This argues for almost complete unfolding of Luciferase. Residues Y59 and S60 within the PrLD formed abundant cross-links with unfolded luciferase, confirming the involvement of the hydrophobic patch spanning residues 57–59 in substrate interaction. Interestingly, that S60 was also identified to cross-link with IDD in an oligomer suggesting competitive mode of this PrLD region in substrate interaction (Fig. 14E). The fact that S60 is buried in the ACD-CTD interior of the Hsp42, as observed in the limited proteolysis without a substrate, leaves the mechanism of its exposure to a substrate unclear.

No additional substrate-binding sites were identified in the PrLD. The amino acid sequence spanning residues 62–86, which contains two hydrophobic patches, was not covered by mass spectrometry due to the absence of trypsin cleavage sites, as trypsin was the protease used in the analysis. Therefore, alternative approaches will be required to probe these two potential substrate-binding sites, such as using a different protease.

My analysis did not confirm the involvement of the 10–17 hydrophobic patch in substrate binding, as previously reported by Grousl et al. (2018). However, this region was found to mediate interactions within the Hsp42 octamer (Fig. 14E). This suggests that the site may become exposed for substrate recognition upon octamer dissociation or as a result of other yet unidentified conformational changes.

Several residues within the α-crystallin domain were cross-linked with unfolded luciferase. Due to the spacer length of the cross-linker between side chains of 10.1 Å, it is not possible to assign substrate-binding interactions to specific secondary structure elements within the ACD (Fig. 21H). Also, these cross-links may result from the close spatial proximity of the ACD to the substrate during sequestration by the PrLD, rather than reflecting a direct or functional interaction between the ACD and the substrate.

Cross-linking of Hsp42 with MDH at 41°C resulted in only four cross-links, all with low confidence scores (Fig. 21G). In contrast to Luciferase, only the C-terminal sites in MDH were crosslinked. This is consistent with findings from Ungelenk et al., 2016, implying unfolding of only the C-terminal region in MDH. All identified residues in Hsp42 were located within the ACD. However, as observed with Luciferase, precise localization of the substrate-binding site within the ACD is not feasible due to the long spacer length of the DSSO cross-linker.

Together, my cross-linking mass spectrometry analysis identified the hydrophobic patch comprising residues ^{57}PLY^{59} as a substrate binding site. However, incomplete sequence coverage of the PrLD by mass spectrometry prevented the confirmation of additional potential substrate interaction sites in the PrLD, highlighting the need for alternative proteases to trypsin for improved sequence coverage. Unfortunately, this analysis did not permit discrimination between substrate binding sites associated with the holdase versus aggregase functions of Hsp42.

Figure 21. Cross-linking of Hsp42 with Luciferase and MDH. A. Schematic representation of hypothetical substrate-binding sites (shown in blue) within the PrLD of Hsp42. **B.** SDS-PAGE followed by Coomassie staining and western blot analysis of Hsp42–Luci cross-linking reactions, probed with anti-Hsp42 and anti-Luciferase antibodies. **C.** Light scattering analysis of Hsp42–Luci complexes. Complexes were formed at 37 °C for 15 minutes, followed by addition of cross-linkers and incubation for 2 hours. **D.** SDS-PAGE followed by Coomassie and western blot analysis of Hsp42–MDH cross-linking reactions, probed with anti-Hsp42 and anti-MDH antibodies. **E.** Light scattering analysis of Hsp42–MDH complexes. Complexes were formed at 41 °C for 60 minutes, followed by addition of cross-linkers and incubation for 2 hours. **F.** Cross-links identified between Hsp42 and Luciferase. **G.** Cross-links identified between Hsp42 and MDH. **H.** AlphaFold prediction of the Hsp42 ACD dimer, with residues identified in cross-linking with Luciferase and MDH shown in red as atomic representations (next page).

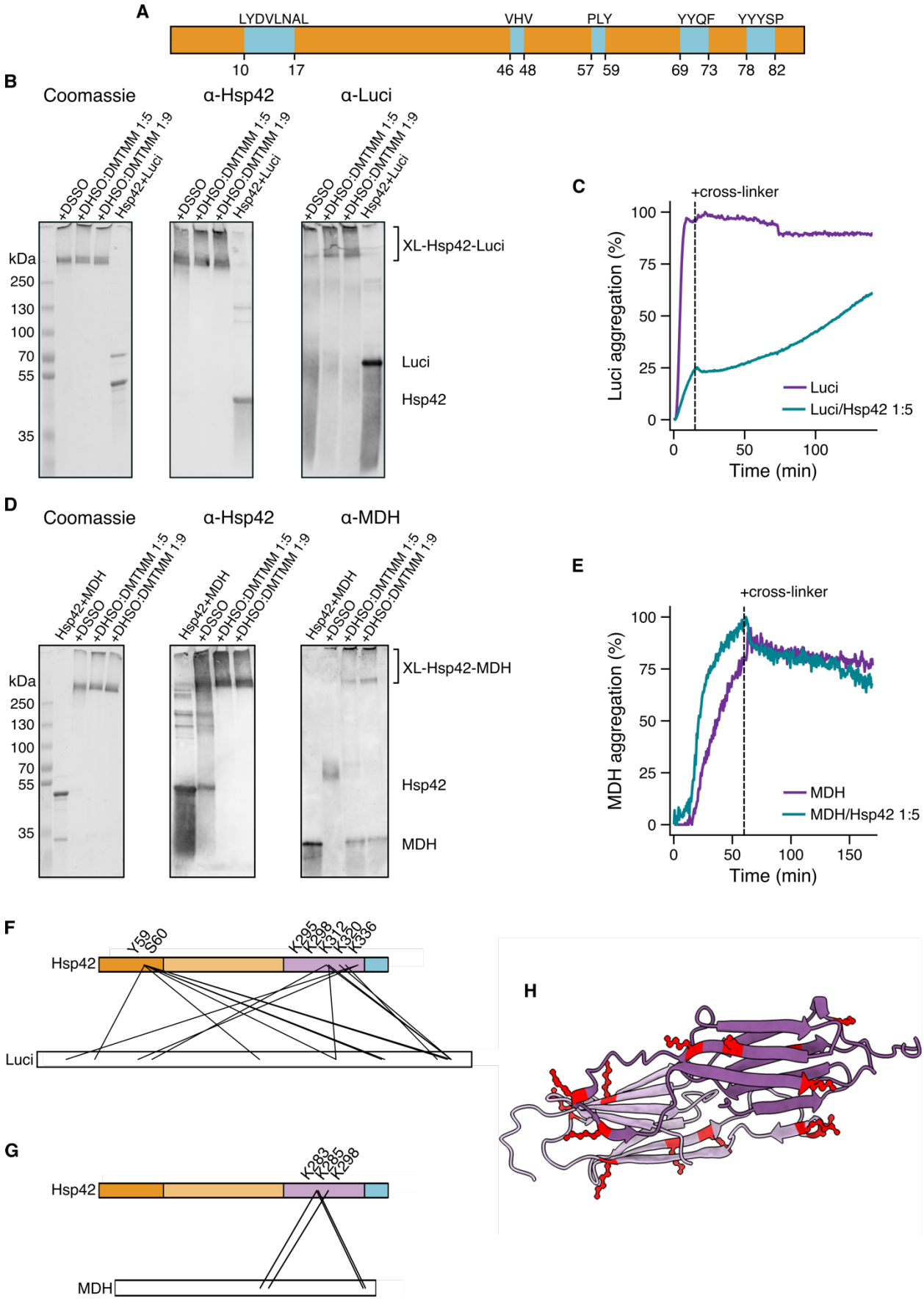
A
LYDVLNAL
VHV
PLY
YYQF
YYYSP
10
17
46
48
57
59
69
73
78
82
B
Coomassie
α-Hsp42
α-Luci
+DSSO
+DHSO:DMTMM 1:5
+DHSO:DMTMM 1:9
Hsp42+Luci
kDa
250
130
100
70
55
35
XL-Hsp42-Luci
Luci
Hsp42
C
+cross-linker
Luci aggregation (%)
100
75
50
25
0
Luci
Luci/Hsp42 1:5
0
50
100
Time (min)
D
Coomassie
α-Hsp42
α-MDH
Hsp42+MDH
+DSSO
+DHSO:DMTMM 1:5
+DHSO:DMTMM 1:9
kDa
250
130
100
70
55
35
XL-Hsp42-MDH
Hsp42
MDH
E
+cross-linker
MDH aggregation (%)
100
75
50
25
0
MDH
MDH/Hsp42 1:5
0
50
100
150
Time (min)
F
Y59
S60
K295
K298
K312
K320
K336
Hsp42
Luci
G
K283
K285
K298
Hsp42
MDH
H

3.16. Dynamics of Hsp42 interaction with its substrate

To investigate the dynamics of Hsp42 oligomers within Hsp42-substrate complexes, I employed the previously established FRET assay. Luciferase was aggregated with a donor fluorophore-labeled Hsp42 (Hsp42-D) at a 1:1 molar ratio, a condition that fully suppresses Luciferase aggregation at 37°C for 10 minutes. The resulting Luci-Hsp42-D complexes were then mixed with an equimolar concentration of an acceptor fluorophore-labeled Hsp42 (Hsp42-A), and donor emission fluorescence was recorded (Fig. 22A).

The increase in the acceptor fluorescence in the presence of aggregated Luciferase followed third-order association kinetics similar to that observed in the absence of Luciferase (Fig. 22A). However, the exchange rates were reduced by 1.3 times in the presence of Luciferase in comparison to no Luciferase. Notably, FRET still occurred. I excluded the possibility that Hsp42-D dissociates from Luciferase and subsequently binds to Hsp42-A in solution (Fig. 22C, see next paragraph for explanation). The most plausible explanation of still ongoing FRET increase is that Hsp42-A interacts (or associates) with Hsp42-D already bound to Luciferase. When the concentrations of both Hsp42-D and Hsp42-A were reduced, the exchange rate also significantly dropped by 3.1 times in the presence of Luciferase in comparison to no Luciferase (Fig. 22B). This finding is in agreement with the previous report by Friedrich et al. (2004) that the added pea Hsp18.1 or Synechocystis Hsp16.6 to pre-formed sHsp-substrate complexes continue to exchange with subunits in sHSP-substrate complexes.

Interestingly, when a complementary FRET assay was performed using Luci-Hsp42-D-Hsp42-A complexes at a 1:0.4:0.4 ratio, with an excess of non-labeled Hsp42 to assess dissociation kinetics, no decrease in the FRET signal was observed (Fig. 22C). This contrasts with the behavior of Hsp42 oligomers alone, where subunit exchange occurs readily (Fig.10E). When Hsp42-Luci complexes were formed with a molar excess of Hsp42 (at a 1:1:1 ratio or 2:2:1), no FRET drop was still observed indicating that all Hsp42 molecules are stably bound (Fig. 22D, E). These findings indicate that Luci-bound Hsp42-D-A do not undergo subunit exchange with non-labeled Hsp42, suggesting that Hsp42 is not spontaneously released from Luciferase-bound complexes.

A similar experiment conducted with large MDH-Hsp42 complexes at 41°C revealed comparable kinetics and almost no detectable subunit exchange (Fig. 22F). This suggests that, regardless of the substrate type or the size of the resulting complexes, Hsp42 remains stably associated with a misfolded substrate.

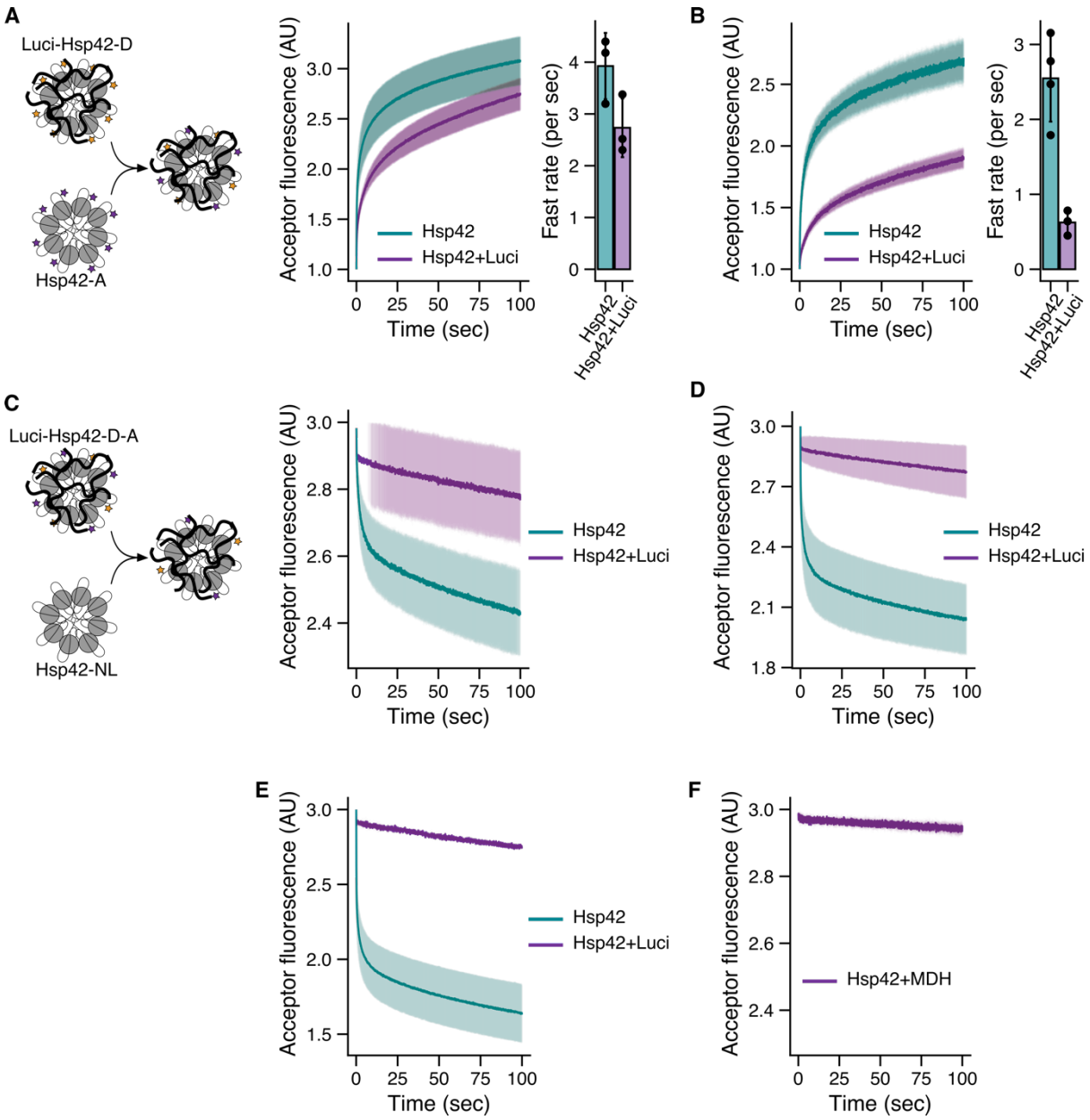

Figure 22. Dynamics of Hsp42 interaction with its substrate. A - B. Cartoon of the association FRET experiment by mixing Luci-Hsp42-D complexes and Hsp42-A at different Hsp42 concentrations (A – D = A = 0.5 μM, B – D = A = 0.2 μM) and recording acceptor fluorescence; the quantification of the fast rate from the third-order exponential association models is provided. The shadow indicates standard deviation (n = 3). **C.** Cartoon of the dissociation FRET experiment by mixing Luci-Hsp42-D-A complexes (0.5 μM + 0.2 μM + 0.2 μM) and non-labeled Hsp42 (2 μM) and recording the acceptor fluorescence. The shadow indicates standard deviation (n = 3). **D.** The dissociation FRET experiment by mixing Luci-Hsp42-D-A complexes (0.5 μM + 0.5 μM + 0.5 μM) and non-labeled Hsp42 (5 μM) and recording the acceptor fluorescence. The shadow indicates standard deviation (n = 3). **E.** The dissociation FRET experiment by mixing Luci-Hsp42-D-A complexes (1 μM + 1 μM + 0.5 μM) and non-labeled Hsp42 (10 μM) and recording the acceptor fluorescence. The shadow indicates standard deviation (n = 3). **F.** Recording acceptor fluorescence of MDH-Hsp42-D-A complexes upon mixing with an excess of non-labeled Hsp42 (n = 1).

3.17. Hsp42 facilitates substrate recovery from aggregates

Hsp42-substrate complexes are reversible. *In vivo* the cytosolic inclusions fuse into one and dissolve with time after a stress relieve in an Hsp104-dependent manner (Specht et al., 2011, Grousl et al., 2018). *In vitro* this dissolution can be reconstituted by incubating the Hsp42-complexes in the presence of ATP-dependent chaperones, namely the family of Hsp70 chaperones, Hsp40 chaperones (JDPs), and the Hsp104 disaggregase (Ungelenk et al., 2016). I reproduced this assay using Luciferase as a substrate. The formed Luci-Hsp42 complexes were incubated with the yeast chaperones – Ssa1, Hsp104 and either Ydj1 or Sis1, as common representatives of the class A and the class B of the JDP family, respectively. Although both J-domain proteins support effective protein refolding they engage aggregated substrates through distinct mechanisms. Ydj1 adheres to the conventional Hsp70 cycle, initially binding the substrate before transferring it to Hsp70. In contrast, Sis1 has a different cooperation with Hsp70 which involves additional interaction with the EEVD motif of Hsp70, which delays chaperone complex formation at the substrate (Faust et al., 2020). However, once assembled, this complex recruits significantly higher amounts of Ssa1 and Hsp104 resulting in more efficient substrate refolding (Wyszkowski et al., 2021).

Refolding of heat-aggregated Luciferase alone resulted in only ~18% and 25% recovery of activity with Sis1 and Ydj1, respectively (Fig. 23A, 23B). Both JDPs facilitated refolding; however, contrary to the previous report, the overall refolding efficiency in the presence of Sis1 was lower compared to Ydj1. This difference, however, was not statistically significant. The initial refolding rate – determined from the linear phase at the beginning of the reaction – was also similar between Sis1 and Ydj1 (Fig. 23C), indicating that under the conditions used in the assay, the previously reported differences in refolding kinetics by different JDPs were not reproduced.

When Luciferase was sequestered within Hsp42 complexes, nearly complete refolding was observed after a two-hour reaction, reaching ~75% and ~95% recovery in the presence of Sis1 and Ydj1, respectively (Fig. 23A, 23B). Most of the refolding occurred within the first 100 minutes, after which the reaction plateaued. These results indicate more efficient transfer of misfolded Luciferase to the Hsp70-Hsp40-Hsp104 system for subsequent refolding. Given that Hsp42 does not spontaneously release Luciferase under the tested buffer and temperature conditions – as shown by the FRET-based assay (Fig. 22C, 22D) – and that the identity of the JDP does not significantly alter refolding kinetics or efficiency, the molecular mechanism underlying this handover remains to be elucidated.

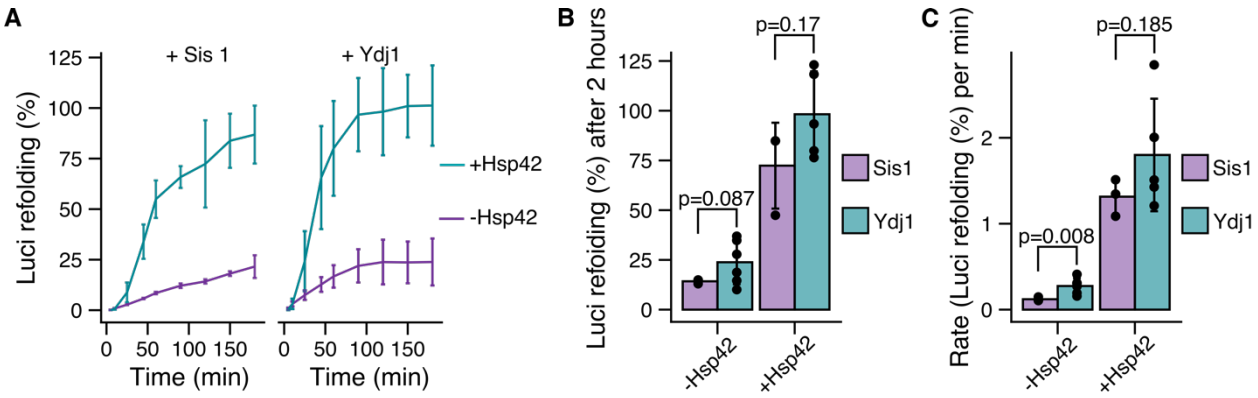

Figure 23. Refolding of Luciferase alone or within Hsp42–Luciferase complexes by Ssa1, Hsp104, and either Ydj1 or Sis1 in the presence of an ATP regeneration system. Error bars represent standard deviations (SD). Luciferase refolding was normalized to the activity of the native protein. **A.** Time-course of Luciferase refolding (n = 3). **B.** Refolding yield of Luciferase after 2 hours of incubation (n = 3-5). **C.** Initial refolding rate of Luciferase, calculated as the slope of the linear phase between 0 and 60 minutes (n = 3-5). Statistical significance was assessed using Welch's two-sample t-test.

3.18. Possible interaction between Hsp42 with Ssa1

The mechanism by which small heat shock proteins are displaced from sHsp-substrate complexes remains incompletely understood. The prevailing view posits that sHsps do not directly interact with other chaperone families, including Hsp70s. Instead, surface exposed sHsps in sHsp-substrate complexes are thought to quickly bind to and dissociate from substrates, thereby allowing Hsp70 to competitively engage the misfolded protein, initiate disaggregation via Hsp100, and promote refolding (Żwirowski et al., 2017).

However, my findings challenge this model. No Hsp42 molecules appear to be passively released from Hsp42-Luci or Hsp42-MDH complexes, as demonstrated using a FRET-based assay (Fig. 22C, 22D). However, this discrepancy may rise from a different Hsp42-substrate architecture, which may be in bacterial sHsps. To examine whether Hsp70 actively displaces Hsp42, I employed the same FRET-based assay using Ssa1 and its co-chaperone Ydj1. Complexes containing Luci-Hsp42-D-Hsp42-A (at a 1:0.4:0.4 ratio) were assembled at 37°C for 20 minutes. Displacement of Hsp42-D-A was initiated by adding Ssa1 and Ydj1 in the presence of ATP and a fivefold molar excess of non-labeled Hsp42. If labeled Hsp42 is displaced, it is expected to oligomerize with non-labeled Hsp42, resulting in decreased acceptor fluorescence.

Indeed, a pronounced drop in acceptor fluorescence was observed (data not shown). However, control experiments revealed that this effect was substrate-independent: Ssa1 could induce a similar decrease in fluorescence upon mixing with pre-formed Hsp42-D-A oligomers (Fig. 24A). Notably, this effect was independent of the J-domain protein Ydj1, and ATP (and ATP with Ydj1) only modestly influenced the overall FRET change.

These observations suggest that Ssa1 induces either the dissociation of Hsp42 to smaller oligomers (or even dimers) or a conformational change in the IDD, where the labeled cysteine

resides. To assess Hsp42 dissociation, I analyzed the oligomeric state of Hsp42 by mass photometry. Co-incubation with Ssa1 did not alter the molecular weight distribution of Hsp42 (Fig. 24B), ruling out dissociation. Surprisingly, a specific conformational change in the IDD was also excluded. A similar decrease in fluorescence was observed using the Hsp42-C127A/T254C-D-A variant, in which the fluorophore is located in the ACD (Fig. 24C).

Additional experiments, including chemical cross-linking and bio-layer interferometry, failed to detect a direct interaction between Ssa1 and Hsp42 (Fig. 24D, 24E). The basis for the Ssa1-induced fluorescence decrease therefore remains unclear.

Figure 24. Hsp42 interaction with Ssa1. A. FRET analysis of pre-formed Hsp42-D-A oligomers (D = A = 0.2 µM) upon addition of Ssa1 alone or together with ATP or Ydj1. Acceptor fluorescence was recorded over time. Voltage = 670. **B.** Mass photometry of Hsp42 and Ssa1 mixtures (Hsp42: 50 nM; Ssa1: 10 nM), compared to Hsp42 or Ssa1 alone at the same concentrations. **C.** FRET analysis using Hsp42-C127A/T254C-D-A oligomers (D = A = 0.2 µM) in the presence of Ssa1 alone or with ATP or Ydj1. Acceptor fluorescence was recorded. Voltage = 617. **D.** Chemical cross-linking of Hsp42 and Ssa1 (0.4 µM and 1 µM, respectively) using DSSO. Samples were collected at 30-minute intervals and analyzed by SDS-PAGE and western blotting using antibodies against Hsp42 (α-Hsp42) and Ssa1 (α-Ssa1). **E.** Bio-layer interferometry analysis. His-tagged Ssa1 was immobilized on the BLI sensor, washed, and then probed for interaction with Hsp42 (next page).

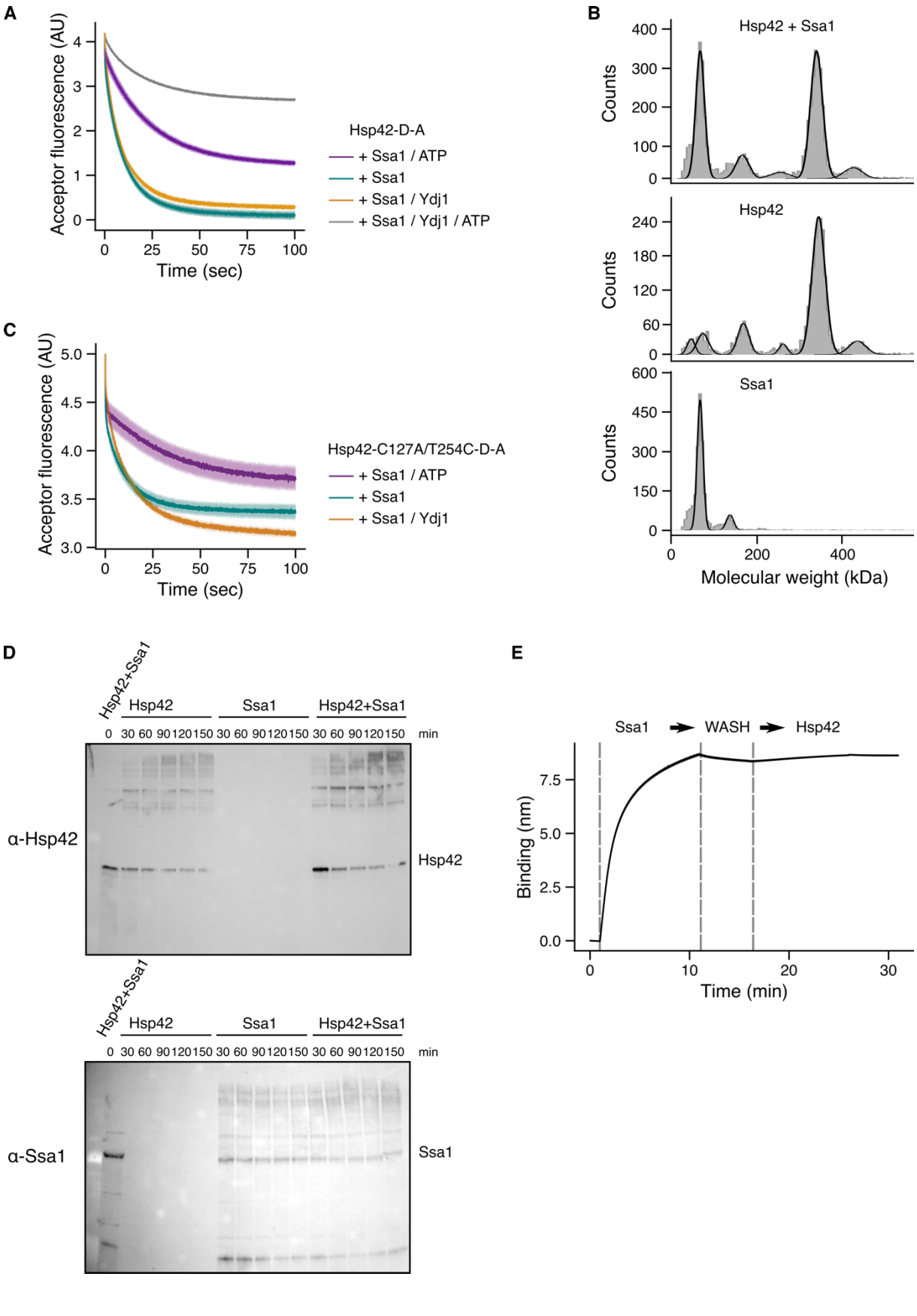
A
Acceptor fluorescence (AU)
Time (sec)
Hsp42-D-A
+ Ssa1 / ATP
+ Ssa1
+ Ssa1 / Ydj1
+ Ssa1 / Ydj1 / ATP
B
Hsp42 + Ssa1
Hsp42
Ssa1
Counts
Molecular weight (kDa)
C
Acceptor fluorescence (AU)
Time (sec)
Hsp42-C127A/T254C-D-A
+ Ssa1 / ATP
+ Ssa1
+ Ssa1 / Ydj1
D
Hsp42+Ssa1
Hsp42
Ssa1
Hsp42+Ssa1
0 30 60 90120150 30 60 90120150 30 60 90120150 min
α-Hsp42
Hsp42
α-Ssa1
Ssa1
E
Ssa1
WASH
Hsp42
Binding (nm)
Time (min)

3.19. Hsp42 variants

To investigate the role of specific motifs and domains of Hsp42 in activation, substrate interaction, and cooperation with Hsp70/Hsp100 chaperone systems, I engineered and purified a series of Hsp42 variants, alongside the wild-type (WT) protein, from *E. coli* cells (Fig. 25A).

Building on previous finding that highlighted the importance of the N-terminal extension for sequestrase activity (Grousl et al., 2018), I generated two deletion mutants: ΔPrLD (Δ-86) and ΔIDD (Δ87-242), each specifically removing a defined segment of the NTE. In contrast to the earlier study, where ΔPrLD was generated by deleting residues 1-99 (thus incorrectly removing part of the IDD), my constructs were designed with higher precision. Notably, the additional 13 residues (87-99) deleted in the previous ΔPrLD variant are negatively charged, with 11 of 13 residues being either glutamates or aspartates (Fig. 25B). Given that the division of the NTE into PrLD and IDD is partly based on the enrichment of particular residues in either of the subdomains, it is important to avoid misallocating this negatively charged region to the PrLD. Negatively charged amino acids, such as glutamates and aspartates, have been proposed to sense pH fluctuations through protonation events, leading to reversible local conformational changes in proteins (Franzmann et al., 2018; Cereghetti et al., 2024). To specifically investigate the role of this acidic segment, I created an additional variant lacking residues 87-99 (ΔDE). Similarly, the CTD of Hsp42 contains a cluster of negatively charged residues (356-367). Complete deletion of this region led to severe aggregation during purification. Therefore, I selectively reduced the negative charge by substituting several acidic residues (E356, E357, D360, E361, E362, and E364) with alanines (DE/A variant). In addition, a positively charged region (residues 348-352) within the CTD, which could potentially mediate electrostatic interactions with the acidic patches to stabilize oligomer formation, was deleted (ΔKR variant). To maintain the flexibility of the disordered regions upon deletion, the missing sequences were replaced with a flexible GGSGG linker. An Hsp42 variant lacking the entire CTD was also constructed for complete analysis.

The interaction of the C-terminal IxI motif with the β4-β8 groove in the Hsp42 octamer was predicted by AlphaFold and experimentally validated by cross-linking mass spectrometry (Fig. 15D). In other sHsps, disruption of the IxI motif typically results in smaller oligomeric assemblies, but with divergent functional consequences: deletion of the IxI motif in *M. jannaschii* Hsp16.5 enhanced chaperone activity (Quinlan et al., 2013), whereas deletion of the corresponding motif in Hsp14.0 from *S. tokodaii* abolished its ability to prevent client protein aggregation (Saji et al., 2008). To explore the functional role of the IxI motif in Hsp42, I mutated the isoleucine residues to glycines (GxG variant) and assessed the structural and functional consequences.

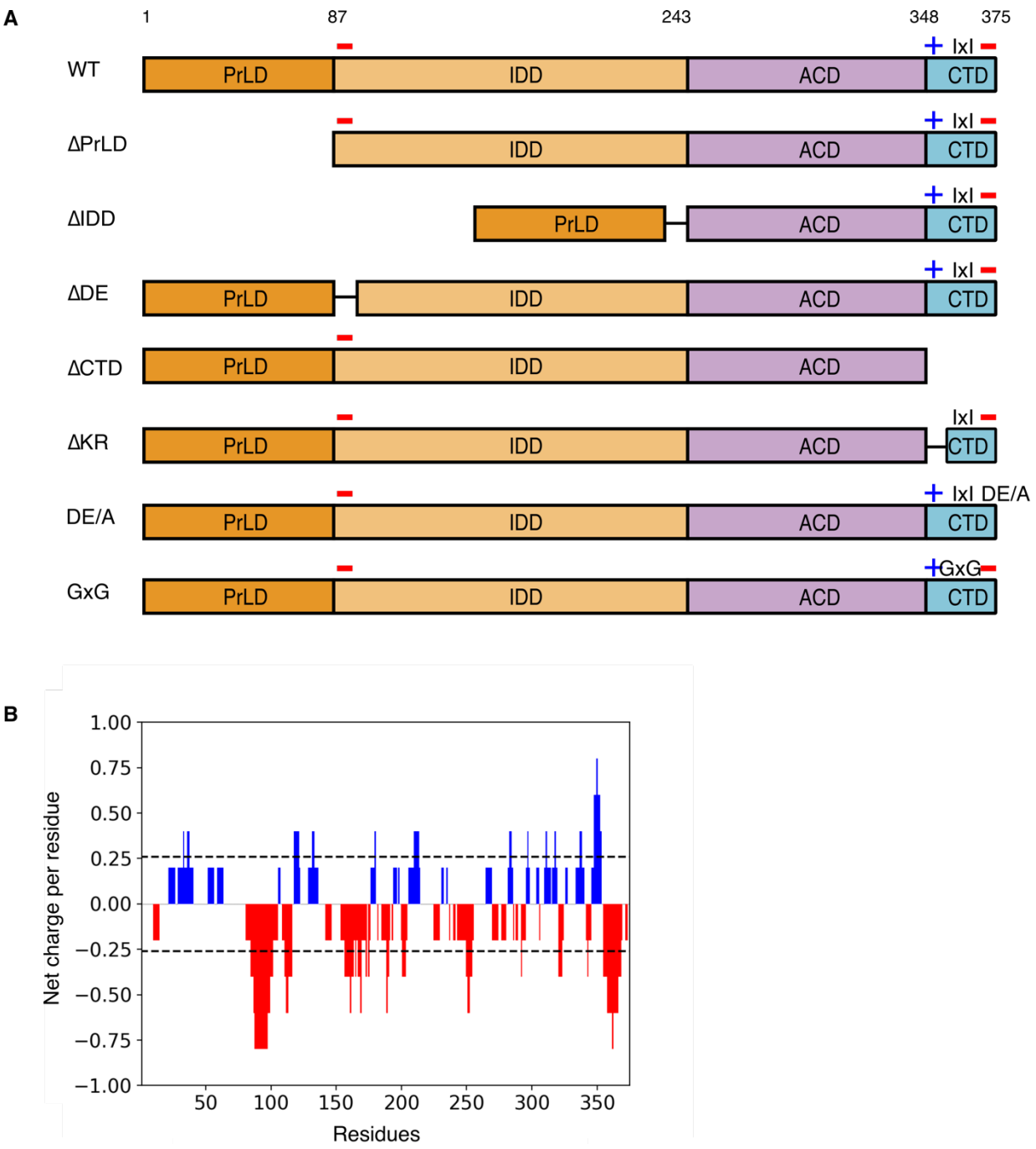

Figure 25. Hsp42 variants domain organization. A. Scheme of Hsp42 variants. + depicted the highly acidic peptide stretch, - highly negative. **B.** Charge distribution within the Hsp42 sequence calculated by CIDER (Das and Pappu, 2013).

3.20. Hsp42 variants characterization

The introduced mutations affected Hsp42 oligomerization and stability. During purification, it was immediately apparent that the ΔDE and ΔCTD variants exhibited reduced solubility, as evidenced by aggregation following MBP tag cleavage. Furthermore, almost all Hsp42 variants displayed altered elution profiles during size exclusion chromatography (SEC), indicating distinct oligomerization states (Fig. 26A).

SEC coupled with multi-angle light scattering (SEC-MALS) revealed that only the ΔPrLD variant eluted at a smaller size compared to wild-type Hsp42, corresponding to a molecular weight of approximately 120-160 kDa, consistent with an average tetramer (Fig. 7C), and the DE/A variant exhibited an elution profile comparable to wild-type Hsp42 (Fig. 26A). All other variants eluted earlier during SEC, suggesting the formation of larger assemblies. Notably, the ΔDE, ΔIDD, and ΔCTD variants were estimated to consist of up to 76, 81, and 120 protomers, respectively, based on the SEC-MALS analysis. However, these unusually high protomer numbers should be interpreted cautiously, because the variants eluted near the void volume, and aggregation may have skewed the measurements.

Dynamic light scattering further confirmed the increased size of the Hsp42 variants and revealed that all variants – except DE/A – exhibited elevated polydispersity index (PDI) values, indicating increased sample heterogeneity (Fig. 26B). Interestingly, when the molecular weights of the Hsp42 variants were measured by mass photometry at 100 nM (in contrast to ~2.5 µM used in SEC-MALS and 10 µM in DLS), most variants – again excluding DE/A – tended to dissociate into smaller oligomeric species. This suggests that the introduced mutations weaken intermolecular interactions within the oligomers, making them more susceptible to dissociation under dilute conditions (Fig. 26C).

Thermal stability was also affected by the mutations. While the overall unfolding profiles determined by nanoDSF were generally comparable to that of the wild-type (WT), distinct differences were observed. These primarily involved the first thermal transition between 25 °C and 50 °C, as well as the third transition occurring between 60 °C and 75 °C. In contrast, the second transition remained largely unchanged across variants with a minor variation in the inflection point between 50.2˚C and 56˚C (Fig. 26D).

Interestingly, although the DE/A variant exhibited a fluorescence ratio (F350/F330) of the first and second transitions similar to WT, it aggregated at approximately 50 °C, as evidenced by turbidity measurements. This aggregation event corresponded with the second transition in the nanoDSF profile (Fig. 26E).

Aggregation for the ΔIDD, ΔCTD, and GxG variants was also shifted to lower temperatures. Notably, the ΔIDD variant showed a gradual increase in turbidity rather than a sharp transition, suggesting a less abrupt aggregation process. The ΔPrLD variant did not show any measurable turbidity change across the entire temperature range tested. Altogether, the introduced mutations in Hsp42 affected its oligomerization behavior and/or thermal stability.

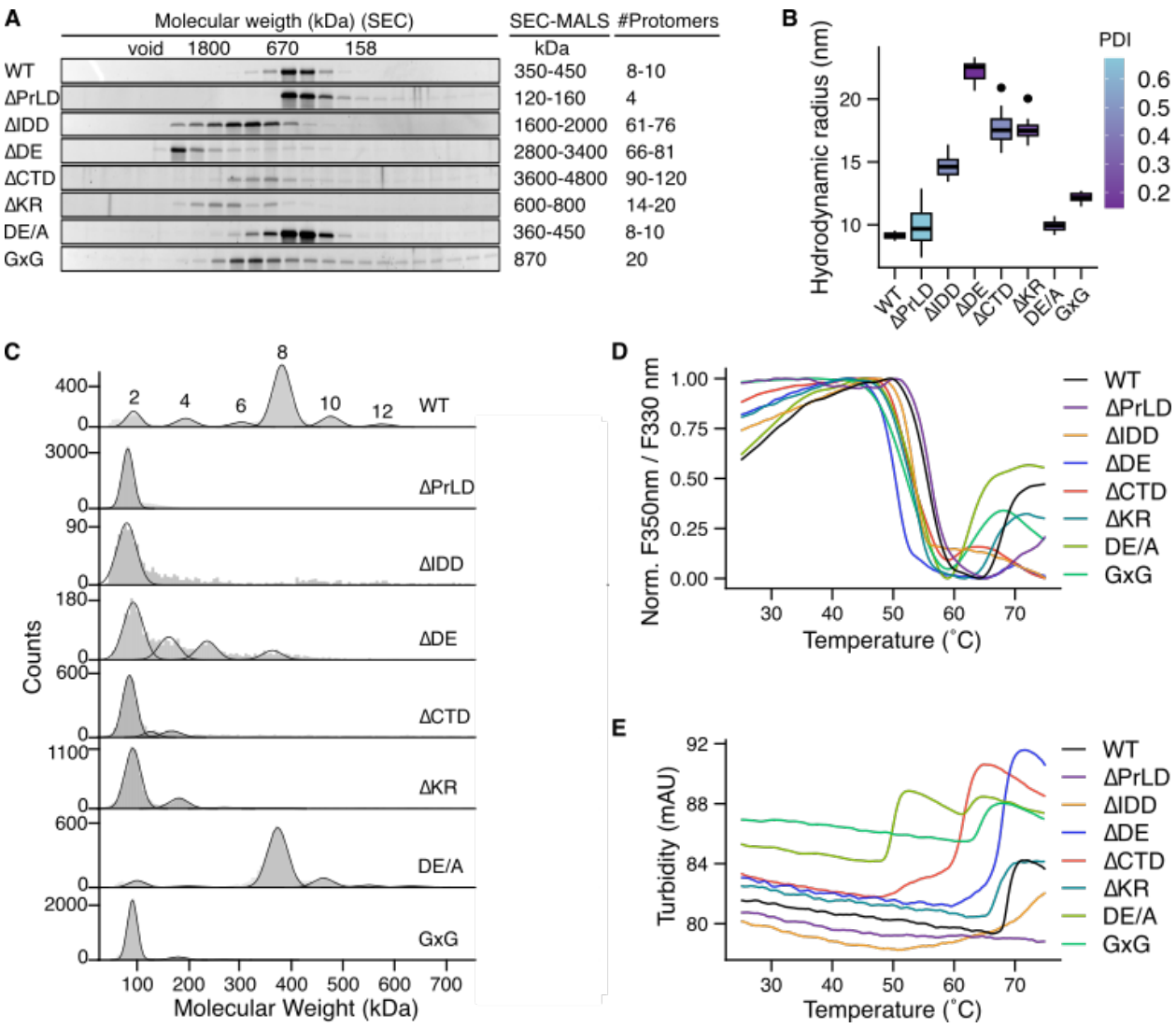

Figure 26. **Oligomerization and temperature stability of Hsp42 variants.** **A.** SDS-PAGE analysis of fractions from size exclusion chromatography of Hsp42 variants, along with their molecular weight estimation by SEC-MALS and the theoretical number of protomers per Hsp42 oligomer. **B.** Hydrodynamic radii of Hsp42 variants at 10 µM determined by dynamic light scattering (n = 20). C. Mass photometry of 100 nM of Hsp42 variants. Numbers indicate the number of protomers per oligomeric species. **D.** Normalized fluorescence ratio (F350/F330) of Hsp42 variants at 10 µM as a function of temperature, measured by nanoDSF. **E.** Turbidity measurements of Hsp42 variants at 10 µM during temperature increase.

3.21. Functional characterization of Hsp42 variants

The interaction between Hsp42 variants and the unfolded substrate Luciferase was assessed by measuring light scattering and determining the hydrodynamic radii of Hsp42-Luci complexes via dynamic light scattering at 37 °C (Fig. 27A, 27B). The ΔIDD, ΔDE, ΔKR, and GxG variants suppressed Luciferase aggregation to a similar extent as wild-type Hsp42. Furthermore, DLS revealed that the hydrodynamic radii of complexes formed by these variants were even smaller than those formed by WT Hsp42, indicating efficient complex formation.

In contrast, incubation of Luciferase with the ΔPrLD variant failed to prevent light scattering, suggesting a loss of chaperone activity. Although the PrLD domain harbors several identified Luciferase-binding sites, additional interaction sites remain in the ACD, which may still facilitate interaction with Luciferase (Fig. 21F). However, DLS analysis showed that the ΔPrLD-Luciferase mixture exhibited similar particle sizes to aggregated Luciferase alone, indicating that ΔPrLD is likely unable to interact with Luciferase, despite the presence of additional binding sites in the ACD (Fig. 27C).

Unexpectedly, the DE/A variant enhanced light scattering of unfolded Luciferase and formed complexes with an average hydrodynamic radius of ~150 nm. These complexes were still smaller than fully aggregated Luciferase, suggesting a regulated assembly process rather than uncontrolled co-aggregation. Although the onset of DE/A aggregation was observed at a lower temperature (50 °C) compared to WT, the experiments here were conducted at 37 °C – well below the aggregation threshold (Fig. 26E). The DE/A variant alone did not scatter light at 37˚C under these experimental conditions (not shown), however, it does not exclude a possibility of minor unfolding events that are exacerbated by the presence of misfolded Luciferase. The mechanism by which the DE/A variant promotes the formation of larger complexes with Luciferase requires further investigation.

Finally, the ΔCTD variant exhibited reduced capacity to suppress Luciferase aggregation, indicating that the C-terminal domain contributes to chaperone function either by direct cooperation with Luciferase or by stabilizing the correct Hsp42 oligomeric form.

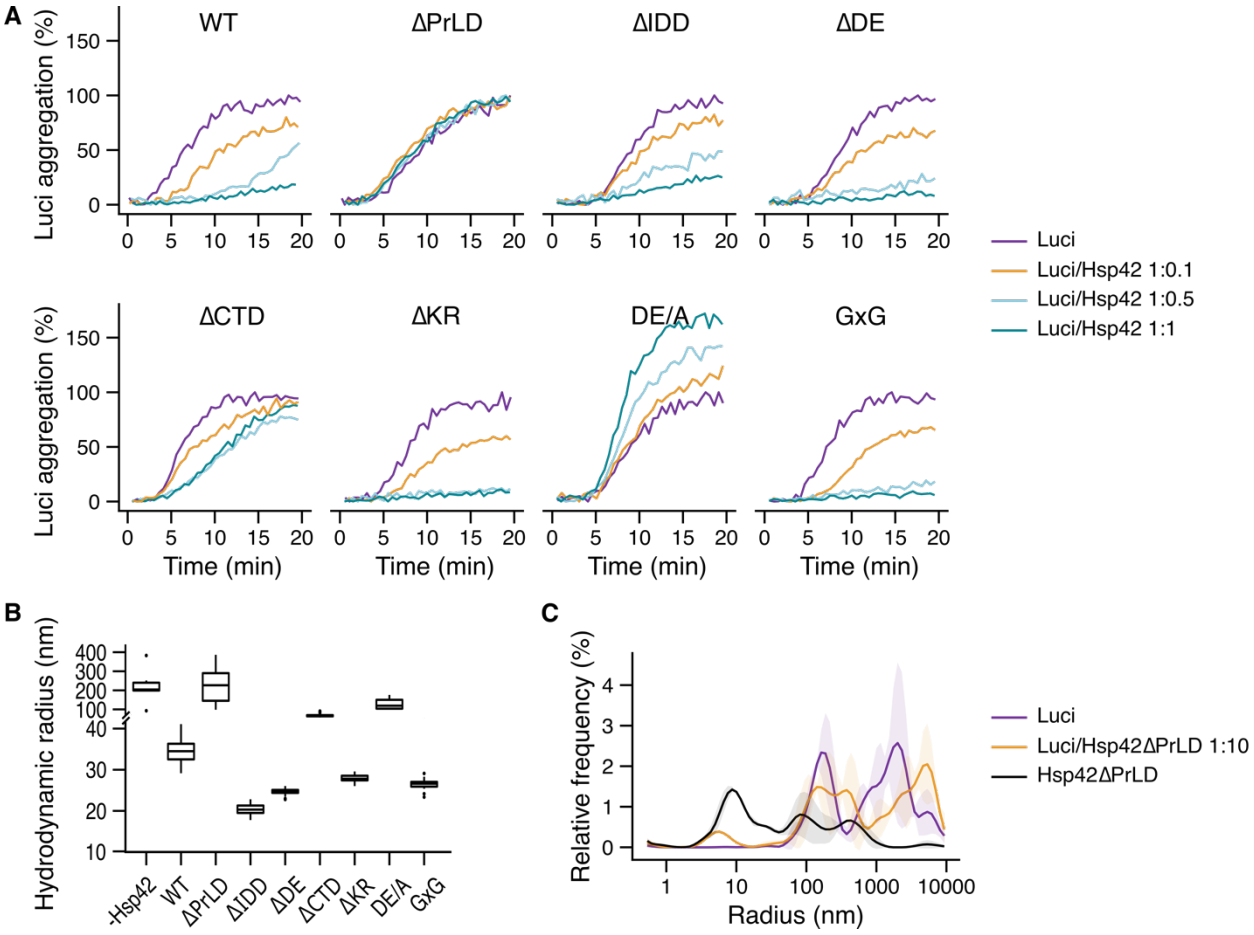

Figure 27. Interaction of Hsp42 variants with unfolded Luciferase. A. Light scattering percent of Luci aggregation in the absence of presence of different Hsp42 variants at different Luci/Hsp42 ratios at 37˚C. **B.** Hydrodynamic radii of Luci in the absence (-Hsp42) or presence of 10-fold molar excess of Hsp42 variants after 20 minutes incubation at 43˚C measured by DLS (n = 20). **C.** Relative frequency of hydrodynamic radii of Luci in the absence of presence of 10-fold molar excess of Hsp42ΔPrLD after 20 minutes incubation at 37˚C measured by DLS (n = 2).

The alternative substrate MDH, previously shown to form larger Hsp42-MDH complexes at 41 °C, was also examined in the presence of Hsp42 variants. All variants, except for ΔPrLD and ΔIDD, formed large complexes with MDH, resembling the behavior of the wild-type Hsp42 (Fig. 28A).

In contrast to Luciferase, analysis of the hydrodynamic radii of ΔPrLD-MDH complexes indicated that ΔPrLD retains the ability to interact with MDH – its hydrodynamic radius shifted from 23-30 nm (MDH alone) toward larger defined sizes in a concentration-dependent manner. Notably, no free ΔPrLD was detected at lower concentrations (Fig. 28B), suggesting its incorporation into MDH-containing complexes and the involvement of substrate-binding regions outside the PrLD. However, these interactions were not sufficient to perform its chaperone function of forming large complexes with MDH. Cross-linking mass spectrometry analysis of MDH-Hsp42 complexes formed at 41˚C indeed identified ACD substrate binding

site but none in PrLD (Fig. 21G). But regardless of the substrate binding sites, PrLD appears to be indispensable to form large complexes with MDH.

The ΔIDD variant failed to form complexes with MDH of sufficient size to scatter light. Nevertheless, similar to ΔPrLD, ΔIDD interacted with misfolded MDH, as evidenced by the formation of ΔIDD-MDH complexes with increased hydrodynamic radii (Fig. 28C). These findings indicate that both the PrLD and IDD are essential for the formation of large Hsp42–MDH complexes.

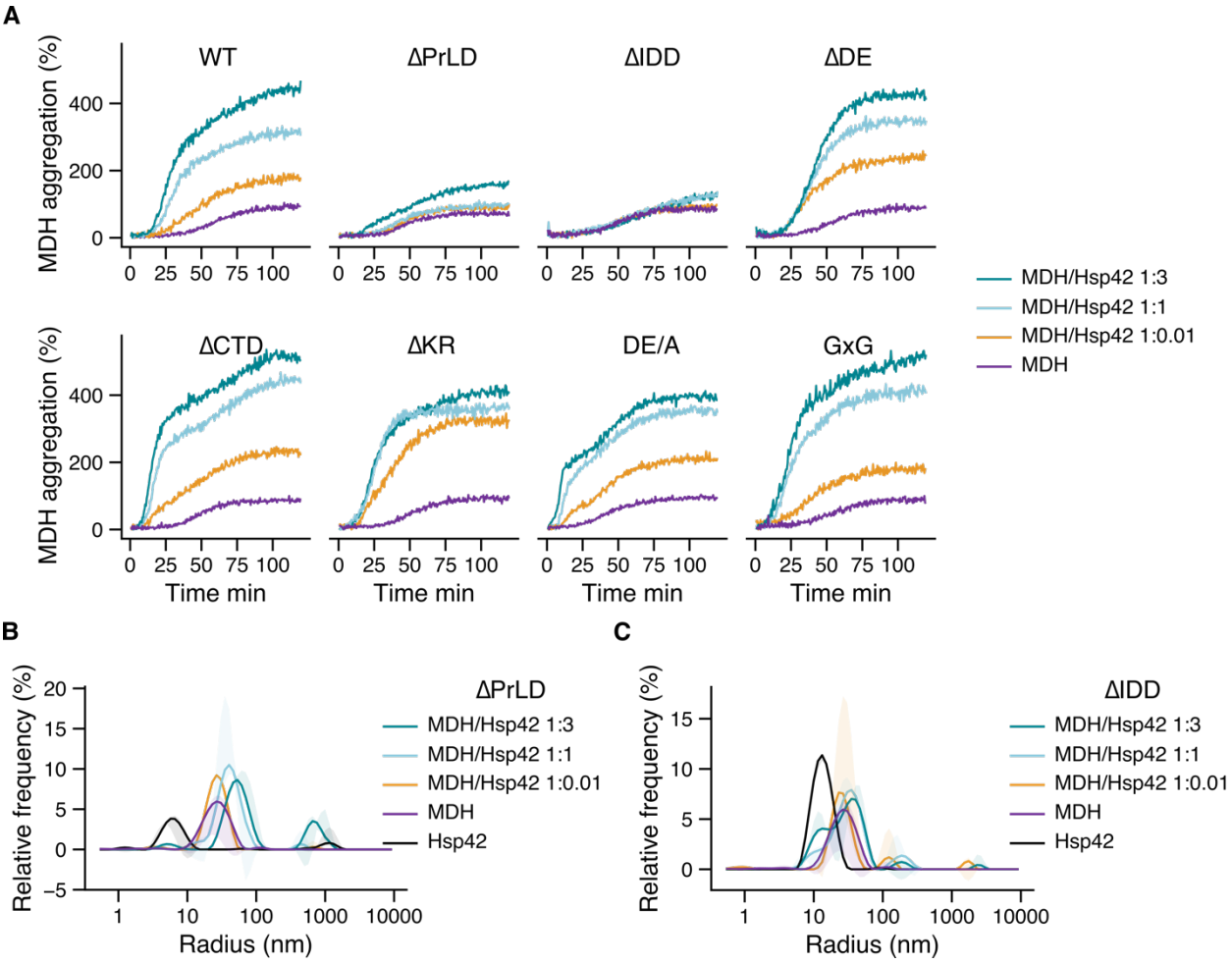

Figure 28. Interaction of Hsp42 variants with misfolded MDH. A. Light scattering percent of MDH aggregation in the absence or the presence of different Hsp42 variants at different MDH/Hsp42 ratios at 41˚C. Turbidity values of aggregated MDH was set as 100%. **B.** Relative frequency of hydrodynamic radii of MDH in the absence of presence of Hsp42ΔPrLD after 60 minutes incubation at 41˚C measured by DLS (n = 2). **C.** Relative frequency of hydrodynamic radii of MDH in the absence of presence of Hsp42ΔIDD after 60 minutes incubation at 41˚C measured by DLS (n = 2).

3.22. The role of IDD and PrLD in aggregase activity of Hsp42

I further investigated the roles of the PrLD and IDD in the formation of large complexes by testing their interactions with an additional substrate – Insulin. Insulin aggregation, triggered by the reduction of its disulfide bonds using DTT, was efficiently suppressed by Hsp42WT at 25 °C. However, at elevated temperatures, Hsp42 exhibited strong aggregase activity toward insulin (Fig. 19). Deletion of the PrLD completely abolished its aggregase activity, highlighting its essential role in mediating interactions with Insulin (Fig. 29A). Notably, deletion of the IDD abolished the aggregase activity of Hsp42, further supporting the critical function of the IDD in driving the formation of large Hsp42-substrate assemblies (Fig. 29B).

A similar function of the IDD was observed during the aggregation of MDH at 47 °C. Consistent with results obtained at 41 °C (Fig. 28A), Hsp42WT promoted MDH aggregation, whereas the IDD deletion variant suppressed it in a concentration-dependent manner and instead formed complexes of defined size (Fig. 29C, 29D). These findings reinforce the role of the IDD in enabling aggregase activity and suggest that temperature-induced conformational changes – such as oligomer dissociation observed at intermediate temperatures – modulate Hsp42 activity in a substrate-specific manner.

The ΔPrLD variant also facilitated the formation of large complexes with MDH, albeit with slower kinetics at lower Hsp42ΔPrLD concentrations, further confirming the contributory role of the ACD in aggregase activity (Fig. 29D).

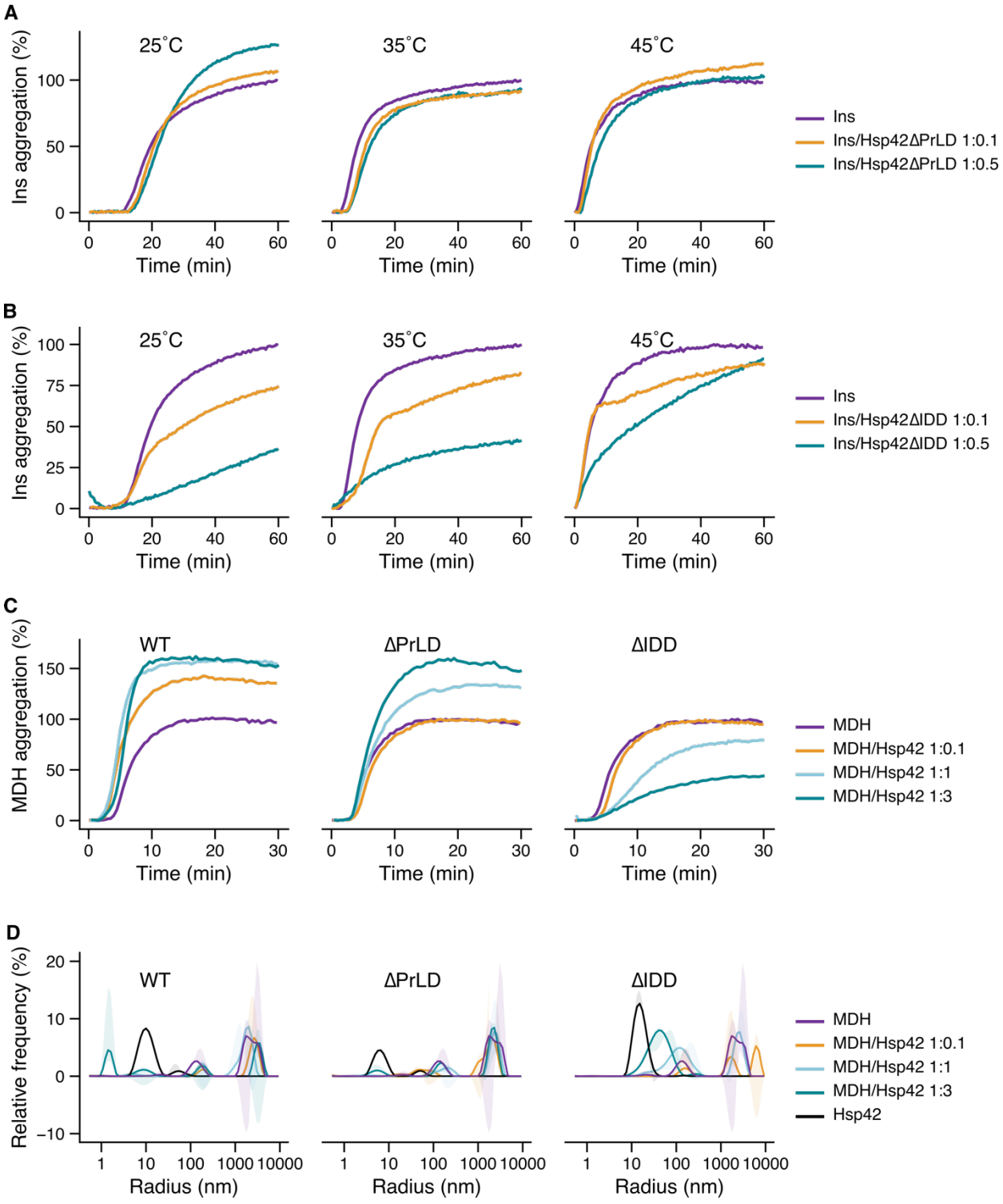

Figure 29. Interaction of Hsp42 ΔPrLD and ΔIDD with various substrates. A-B. Insulin aggregation in the presence or absence of Hsp42ΔPrLD (A) and Hsp42ΔIDD (B) at different temperatures. **C.** MDH aggregation at 47˚C in the presence of absence of Hsp42 WT, ΔPrLD, and ΔIDD. Turbidity values of aggregated MDH were set as 100%. **D.** Relative frequency of hydrodynamic radii of MDH in the absence or presence of Hsp42 WT, ΔPrLD, and ΔIDD at different ratios after 20 minutes incubation at 47˚C measured by DLS (n = 2).

3.23. Luciferase refolding with Hsp42 variants

I next examined how different Hsp42 variants influence cooperation with the *S. cerevisiae* Hsp70/40/100 chaperone system (Ssa1/Ydj1/Hsp104) by monitoring the refolding of Hsp42-bound Luciferase (Fig. 30A-C). Notably, most Hsp42 variants substantially impaired Luciferase refolding by the Hsp70/Hsp100 machinery. Given that the ΔPrLD, ΔCTD, and DE/A variants showed little to no capacity to suppress Luciferase aggregation, their poor performance in refolding assays was expected. In contrast, the ΔIDD and ΔDE variants suppressed Luciferase aggregation comparably to wild-type Hsp42 and even formed smaller assemblies (Fig. 27A, 27B), yet failed to support Luciferase refolding. Remarkably, the ΔDE variant further impeded refolding, performing worse than the refolding of the aggregated Luciferase in the absence of Hsp42. Among all variants, only ΔKR modestly enhanced refolding, although not statistically significant, while the GxG variant showed refolding efficiency similar to the wild type. These findings suggest that distinct domains within Hsp42 are differentially involved in substrate sequestration and subsequent release and/or handover to the Hsp70 machinery.

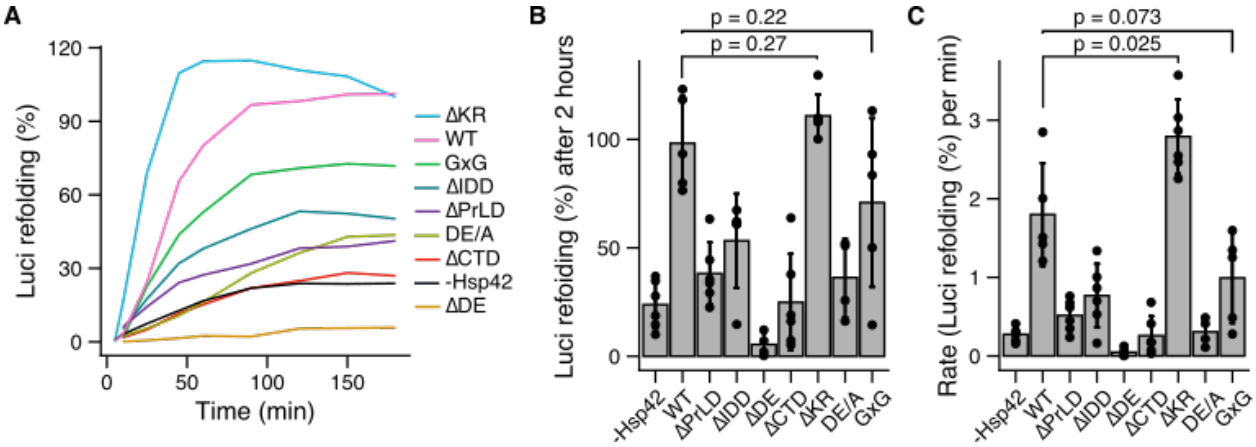

Figure 30. Refolding of Luciferase from Hsp42 variant – Luci complexes by Ssa1, Hsp104, and Ydj1 in the presence of an ATP regeneration system. Error bars represent standard deviations (SD). Luciferase activity was normalized to the activity of the native protein. **A.** Time-course of Luciferase refolding. n = 3-5, representative curves are shown. **B.** Refolding yield of Luciferase after 2 hours of incubation (n = 3-5). **C.** Initial refolding rate of Luciferase, calculated as the slope of the linear phase between 0 and 60 minutes (n = 3-5). Significance is calculated with Welch two sample t-test.

3.24. Hsp42 affinity to aggregated Luciferase

One possible explanation of the discrepancy between the ability to suppress Luciferase aggregation and refold it by some Hsp42 variants, namely ΔIDD, ΔDE, and ΔKR, could be their altered affinity to substrate – the variants with stronger affinity would bind to a substrate quicker but not easily release from it. To examine how quickly these Hsp42 variants bind to (and dissociate from) the substrate, I used biolayer interferometry (BLI). The His-tagged Luciferase was aggregated on the surface of the BLI sensor. The sensor was submerged into the samples with different Hsp42 variants, and the Hsp42 binding to the BLI sensor was recorded by measuring the Hsp42 thickness on the sensor. Afterwards, the sensor was moved to the buffer to record the Hsp42 dissociation (Fig. 31A). A limitation of this approach is the different nature of Luciferase aggregates which do not exactly match gradual Luciferase unfolding linked to simultaneous binding by Hsp42.

ΔPrLD does not bind to Luciferase, which is in agreement with the previous result on PrLD containing the main Luciferase binding site, and serves as a negative control. The rest of the examined variants associate with Luciferase at different rates, but interestingly, upon dissociation the Hsp42 thickness layer does not drop to 0 nm. This can be explained by the fact that Hsp42 does not passively release Luciferase, as already shown in the FRET-based assay (Fig. 22C). The dissociation step, however, shows the dynamics within Hsp42 oligomers – the more dynamic oligomers would experience quicker subunit release from large oligomers upon transfer to the buffer – which ultimately has an effect on the Luciferase interaction as well.

All Hsp42 variants rapidly associate with Luciferase, following a multi-phase exponential binding curve (Fig. 31A). The observed association kinetics likely reflect interactions between distinct Hsp42 oligomeric species and the Luciferase layer, as well as secondary assembly events involving Hsp42 subunits binding to one another, which create the outermost Hsp42 layer and contribute to the overall layer thickness. The plateau phase suggests saturation – i.e., full coverage of Luciferase and complete assembly of the Hsp42 oligomers. Among the tested variants, Hsp42ΔIDD displayed the slowest binding kinetics, although it followed the same exponential binding kinetics and even build a thicker layer (Fig. 31B).

Analysis of the initial rapid binding phase revealed that the Hsp42ΔKR variant exhibited an increased binding rate to Luciferase (Fig. 31C). Furthermore, ΔKR demonstrated enhanced oligomer dynamics, as indicated by a higher dissociation rate from the outermost Hsp42 layer (Fig. 31D). Notably, ΔKR also improved Luciferase refolding in the presence of Ssa1/Hsp104/JDP, indicating a correlation between refolding rates and ΔKR dissociation dynamics determined in BLI. However, to conclusively determine the effect on displacement, a dedicated Hsp42 dissociation assay in the presence of Ssa1/Hsp104/JDP is necessary.

To address this, I conducted a BLI assay in which Ssa1 and Sis1 were applied to the pre-formed Luciferase-Hsp42 layer. Unfortunately, the resulting data were complex and hindered a clear interpretation and did not allow for an unambiguous conclusion (data not shown).

Surprisingly, the Hsp42ΔIDD variant exhibited both a reduced binding rate to Luciferase and a slower oligomer dissociation rate. This finding was unexpected, given that ΔIDD suppressed

Luciferase aggregation to a degree comparable to Hsp42WT. A previous study by Grousl et al. (2018) reported that ΔIDD displays markedly increased substrate-binding capacity *in vivo*. However, it is important to consider that the ΔIDD variant lacks a substantial portion of its N-terminal region, which reduces its overall monomeric dimensions. Consequently, binding of ten ΔIDD monomers may not contribute the same layer thickness as ten WT monomers. As with ΔKR, a dedicated Hsp42 dissociation assay in the presence of Ssa1/Hsp104/JDP is necessary to determine whether the observed ΔIDD behavior correlates with its dissociation from Luciferase.

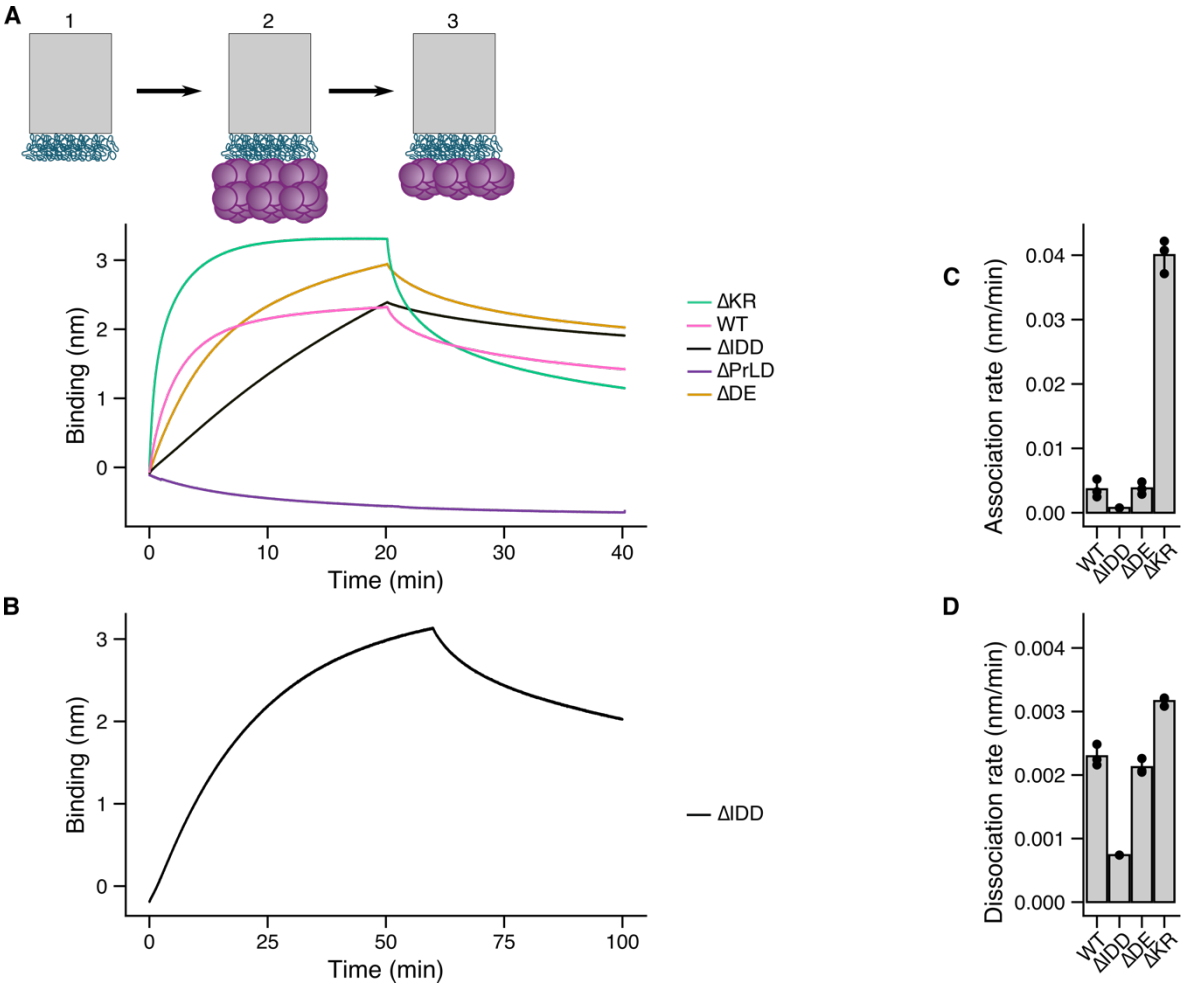

Figure 31. Bio-layer interferometry of Hsp42 variants with aggregated Luciferase. A. Luciferase was aggregated on the subphase of a BLI sensor and set to 0 nm (1), then incubated with different Hsp42 variants (2), and finally washed in buffer leading to dissociation of Hsp42. (3). **B.** Binding to and washing away Hsp42ΔIDD from the aggregated luciferase. **C.** Hsp42 association rate to aggregated luciferase calculated as a rapid rate from the second-order exponential association function. **D.** Hsp42 dissection rate from Luci/Hsp42 layer calculated as from a first-order exponential dissociation function.

3.25. Inhibition of Luciferase refolding by Hsp42 variants

Although the mechanism of Hsp42 displacement remains unknown, the involvement of the Hsp70/Hsp104/JDP system is evident, as substrates are ultimately refolded. Hsp42 variants with higher substrate affinity may rebind to the free substrate after it is released from Hsp42–substrate complexes, thereby interfering with efficient refolding. To test this hypothesis, I performed an order-of-addition experiment. Luciferase was first unfolded in a high concentration of urea, and refolding was initiated by the addition of Ssa1/Hsp104/Ydj1. Hsp42 variants were introduced 15 minutes after the onset of refolding (Fig. 32A). In the absence of Hsp42, luciferase refolding progressed rapidly, reaching 53% of native activity after 90 minutes. Most Hsp42 variants did not significantly impair refolding; however, the ΔKR variant significantly reduced refolding efficiency to 43% (Fig. 32B). This was an unexpected result, given that ΔKR had previously performed better in the refolding of thermally aggregated luciferase. Nevertheless, this finding supports the notion the reduced Luciferase refolding by the ΔIDD or ΔDE variants is not caused by Hsp42-mediated inhibition of free Luciferase. Therefore, the reason must lie in the nature of Hsp42-substrate complexes or the way Hsp42 hand-over the substrate to ATP-dependent chaperones. Additionally, this experiment corroborates that ΔKR has a higher substrate affinity, as also demonstrated in the BLI experiment.

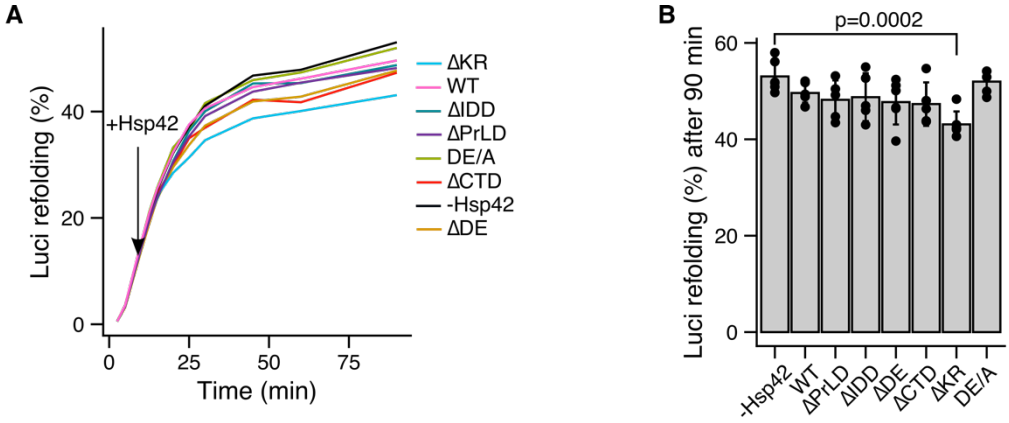

Figure 32. Inhibition of Luciferase refolding by Hsp42 variants. A. Refolding of urea-denatured luciferase by Ssa1/Hsp104/Ydj1. The addition of Hsp42 variants at 15 minutes is indicated with the arrow. **B.** % of refolded Luciferase after 90 minutes. n = 5-7. Significance is calculated with Welch two sample t-test.

3.26. Potential role of the IDD in shaping Hsp42-substrate complexes

The intrinsically disordered domain of Hsp42 plays a crucial role in the formation of large complexes with misfolded substrates (Fig. 28A, 29B). Consistently, deletion of the IDD significantly impaired luciferase refolding *in vitro* (Fig. 30). In *S. cerevisiae*, cytosolic inclusions – whose formation is mediated by Hsp42 – exhibited prolonged persistence and delayed clearance in cells lacking the IDD (Grousl et al., 2018). These observations suggest that the IDD contributes directly or indirectly to the transfer of substrates from Hsp42 to ATP-dependent chaperones, namely the Hsp70/Hsp100/Hsp40 disaggregation machinery.

Hsp70 initiates the disaggregation process, followed by recruitment of Hsp100 disaggregases for substrate solubilization (Żwirowski et al., 2017). In addition to the canonical Hsp70/Hsp100 system, certain bacteria possess stand-alone disaggregases such as ClpG and ClpL, which operate independently of Hsp70 (Bohl and Mogk, 2024).

To investigate the involvement of the IDD and Hsp70 in processing Hsp42-substrate complexes, I utilized two bacterial disaggregation systems: ClpB in cooperation with bacterial Hsp70 analogue DnaK, and ClpG. These experiments were performed by Dr. Axel Mogk. Aggregation of MDH was induced by incubation at 47 °C in the presence of wild-type Hsp42, ΔIDD, or ΔPrLD (used as a negative control), followed by treatment with the respective disaggregation systems. Under these conditions, both Hsp42 WT and ΔPrLD promoted MDH disaggregation by DnaK/ClpB, whereas the ΔIDD variant partially suppressed it (Fig. 33A, B). Impaired MDH recovery from the ΔIDD-bound state is consistent with Luciferase refolding experiments, reinforcing the critical role of the IDD in facilitating Hsp70-dependent disaggregation.

Hsp42 presence completely inhibited ClpG-mediated disaggregation and refolding of MDH. This indicates a specific transfer of Hsp42-bound substrates to the Hsp70-dependent ClpB disaggregase, while the autonomous ClpG disaggregase cannot access the Hsp42-MDH complexes (Fig. 33C, 33D). A control order-of-addition experiment, in which MDH was first aggregated in the absence of Hsp42 and refolding was subsequently initiated by adding either ClpB/DnaK or ClpG together with Hsp42, demonstrated that the observed inhibition is specific to MDH-Hsp42 complexes. In the absence of Hsp42 during aggregation, refolding was restored (Fig. 33E).

This finding is consistent with the previously noticed specific activity of Hsp70 towards sHsp/substrate complexes (e.g. Zwirowski et al.). Interestingly, deletion of the IDD partially restored ClpG activity. This suggests that the IDD may sterically hinder ClpG access to the substrate – possibly by shielding the aggregated protein due to its extended disordered nature. Removing the IDD may expose the substrate surface, enabling ClpG to engage and process the aggregate more effectively.

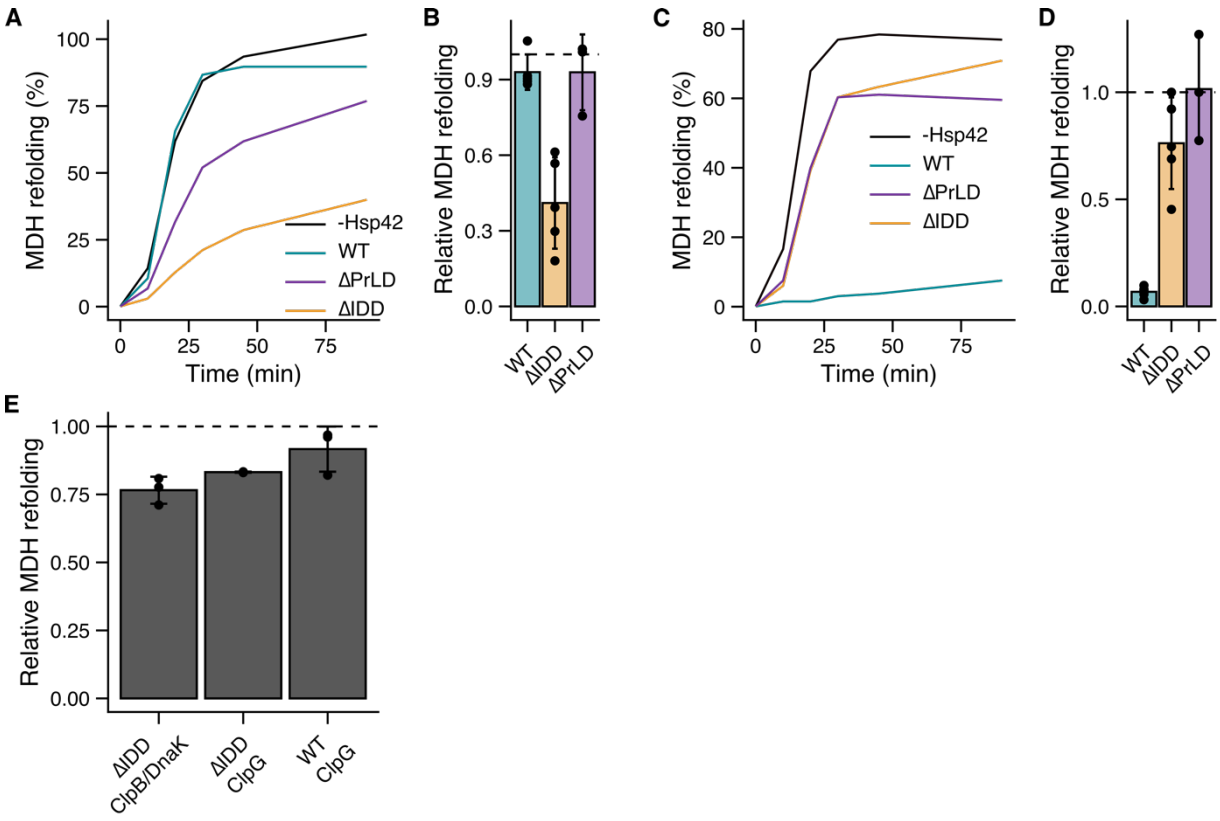

Figure 33. **Refolding of MDH from Hsp42 variant – MDH complexes with different bacterial disaggregation systems. A.** Time-course of MDH refolding by the ClpB/DnaK system. n = 5, representative curves are shown. MDH refolding was normalized to the activity of the native protein. **B.** Refolding yield of MDH after 90 minutes refolding by the ClpB/DnaK system. The refolding is normalized to 1 relative to the MDH refolding in the absence of Hsp42 (n = 5). **C.** Time-course of MDH refolding by the ClpG system. n = 5, representative curves are shown. MDH refolding was normalized to the activity of the native protein. **D.** Refolding yield of MDH after 90 minutes refolding by the ClpG system. The refolding is normalized to 1 relative to the MDH refolding by ClpG after 90 min in the absence of Hsp42 (n = 5). **E.** Refolding yield of MDH aggregates without Hsp42. Refolding is measured 90 minutes after the refolding was initiated by addition of ClpB/DnaK or ClpG with some Hsp42. The refolding is normalized to 1 relative to the MDH refolding in the absence of Hsp42 (experiment preformed by Axel Mogk)

4. Discussion and Outlook

4.1. Hsp42 forms a planar ring of α-crystallin domains surrounded by intrinsically disordered regions

A major focus of this study was to elucidate the oligomeric structure of Hsp42. To this end, a range of biophysical and structural approaches were employed. Similar to other small heat shock proteins, Hsp42 exists as an ensemble of oligomeric species. High-resolution structures of several sHsps, such as *M. jannaschii* Hsp16.5 (Kim et al., 1998) and human Hsp27 (Clouser et al., 2019), have been determined using X-ray crystallography or cryo-electron microscopy (cryo-EM). These proteins possess shorter N-terminal extensions and exhibit a higher degree of homogeneity – features that facilitate structural resolution.

In stark contrast, Hsp42 contains a highly extended and intrinsically disordered NTE of 242 residues, comprising approximately 65% of the entire sequence. The endeavor to resolve Hsp42 oligomer structure by a classical cryo-electron microscopy followed by single particle analysis proved to be unsuccessful in my study. It is important to appreciate the relevance of intrinsically disordered nature of Hsp42. The capture of a single confirmation out of many possible dynamic conformations may miss the dynamic essence that defines both structural nature and functional mechanisms of Hsp42. This highlights a need for unconventional approaches.

AlphaFold3 prediction provided a solid basis for Hsp42 structure analysis. The quality of AlphaFold predicted model could be further improved by integrating experimental distance restrain information obtained in my cross-linking experiment into AlphaFold architecture. This approach, called AlphaLink, was developed for AlphaFold2, with the code being publicly available (Stahl et al., 2023, Stahl et al., 2024). The Hsp42 prediction suggested a planar arrangement of ACD dimers forming an octamer. To the best of my knowledge, this type of single-layer, planar ACD ring architecture has not been reported for any other sHsps. Most structurally characterized sHsps assemble into symmetric, hollow oligomers, often with spherical morphologies. Notably, some barrel-like oligomers have been reported, however formed by stacking ACD dimers either parallel to the top view – as in wheat Hsp16.9 (PDB: 1GME; van Montfort et al., 2001) – or perpendicularly, as in *C. elegans* Sip1 (PDB: 4YDZ; Fleckenstein et al., 2015).

Mass photometry measurements indicate that the Hsp42 predominant oligomeric species consists of eight protomers, thus organized as four ACD dimers (Fig. 6C). This theoretically allows for three possible configurations of the ACD dimers: 1) a single-layer, disc-like structure (as predicted by AlphaFold), 2) a double-layered disk formed by stacking dimers perpendicularly, 3) a double-layered disk formed by stacking dimers parallelly (Fig. 34).

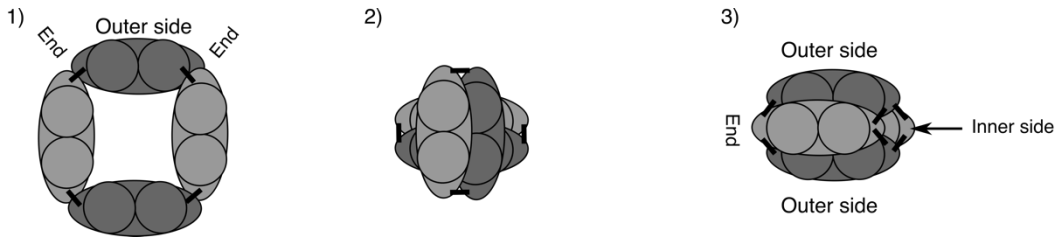

Figure 34. **Three theoretical configurations of four ACD dimers in Hsp42 octamer.** Outer and inner sides indicate the faces of ACD dimers oriented toward the outside of the oligomer and the inside of the oligomeric space, respectively. Black lines show the experimentally confirmed cross-links between the ends of neighboring ACD dimers.

Although the cross-linking of opposite ends of neighboring dimers could confirm the second and third ACD dimer configurations (Fig. 15B), they are less probable because the cross-linking mass spectrometry did not identify any additional cross-links between the two different ACD dimers. This, however, would be expected considering their close proximities in the configurations two and three. The third configuration is additionally even less probable because the cross-linking of the ACD dimer ends should create very little inner space – this makes it impossible to place eight IDDs, which have an entry point into the ACD at the ACD dimer side, as detected by cross-linking (Fig. 15C). Similarly, the dimers cannot be flipped, as this would create a space limitation for interaction of the IxI motif of the eight CTEs with the β4-β8 grooves (Fig. 15D). The fast subunit exchange also argues against the second and third configurations, as the extent of theoretical contact between ACDs would slow down subunit exchange, in contrast to the limited contacts between ACD ends in the first configuration.

Thus, the planar ACD ring configuration predicted by AlphaFold remains the most plausible. To experimentally validate this model, I employed minimal fluorescence photon fluxes microscopy (MinFlux), labeling each ACD with a single fluorophore. If the planar model were correct, one would expect to observe eight fluorophores localized within a single plane (±1.5 nm), in contrast to two planes of four fluorophores each for the second and thirds configurations.

MinFlux showed a potential to achieve this. However, the chosen fluorophores (Alexa Fluor 647 and Alexa Fluor 488) were not suitable, as they did not allow achieving the maximum possible resolution with MinFlux required for resolving fluorophore molecules attached to the Hsp42 oligomer. The problem was a rapid on/off duty cycle of fluorophores and, as a result, simultaneous emission of several fluorophores within one oligomer. To overcome this problem, photoactivatable (caged) fluorophores can be used. They can be precisely controlled with light to switch between fluorescent and non-fluorescent states, allowing a temporal separation of fluorescent emission, ideally one per Hsp42 oligomer at a time. The use of photoactivatable fluorophores to image proteins *in vitro* by MinFlux was shown by Sahl et al. (2014), where they measured intramolecular distances down to 1 nm – and in planar projections down to 1 Å – using commercially as well as in-lab synthesized photoactivatable (caged) fluorophores. If the labeling protocol is successfully established, the imaging approach can be further extended by incorporating multiple fluorophores with distinct excitation/emission wavelengths. Additionally, the analysis can be expanded to include

labeling of alternative regions within the Hsp42 oligomers to probe their spatial organization as well.

Presuming a planar arrangement of the ACD into a ring-like structure, cross-linking mass spectrometry and limited proteolysis followed by mass spectrometry confirmed that the IDD is positioned externally relative to the ACD ring. However, the exact location of the PrLD remains largely experimentally unresolved. Both approaches only showed that residues near S60 are located inside the ring, as they cross-link with the interior of the ACD ring and are protected from Proteinase K cleavage in the limited proteolysis assays (Fig. 13E, 15D).

To confirm the overall architecture of Hsp42 oligomers as a planar, folded ring with disordered IDD regions located on both sides of the ring, I propose performing solution-based small-angle X-ray scattering (SAXS). SAXS would provide information about folded regions (such as the ACD ring) and disordered regions (PrLD, IDD, CTE), as these produce distinct scattering profiles. Additionally, SAXS could help determine whether the center of the Hsp42 oligomer is empty, which may give a hint whether the entire PrLD is indeed located inside the ring as it is predicted in AlphaFold prediction.

4.2. Subunit exchange in Hsp42 enables the exposure of substrate-binding sites

All structural studies of Hsp42, except for limited proteolysis, have aimed to resolve the architecture of the fully assembled oligomer. Despite the predominance of octamers in solution, my data demonstrate that Hsp42 undergoes rapid subunit exchange, most likely in the form of dimer exchange, as mass photometry experiments showed only even numbers of protomers per oligomer – formed by the stepwise addition of two protomers to a preexisting even-numbered assembly (i.e., 2, 4, 6, 8, 10 protomers; Fig. 6C). This exchange occurs so quickly that upon mixing two Hsp42 preparations labeled with distinct fluorophores, a complete equilibrium of heterooligomers was established within minutes at 20˚C (Fig. 10B). This is in stark contrast to other small heat shock proteins, whose subunit exchange rates are significantly slower. For instance, heterooligomers of human HSPB4 and HSPB5 require approximately 30 minutes to equilibrate at 30˚C (Aquilina et al., 2005).

Interestingly, subunit exchange of Hsp42 was previously investigated in our laboratory by Grousl et al. (2018) using also a FRET-based assay. However, the rate of the fast-exchanging phase reported in that study was approximately 1200-fold slower than in my assay (0.1 min^{-1} vs. 120 min^{-1}, respectively), with equilibrium reached only after more than three hours when preformed donor- and acceptor-labeled heterooligomers were mixed with an excess of unlabeled protein. Experimental conditions differed between the two studies. In the case of Grousl et al., the primary amines of Hsp42 were labeled non-specifically, and the labeling efficiency was not reported, which may account for the observed discrepancy. Nevertheless, both studies confirm that Hsp42 undergoes subunit exchange.

If Hsp42 indeed assembles into oligomers resembling those predicted by AlphaFold – where the PrLD is at least partially buried (including substrate binding site ^{57}PLY^{59}) – then subunit exchange could serve as the primary mechanism for exposing substrate-binding sites. This

would provide a plausible explanation for the constitutive chaperone activity of Hsp42, even in the absence of heat shock.

4.3. Hsp42 undergoes structural change upon heat and acidic pH

I have investigated several environmental triggers – namely elevated temperature, decreased pH, and phosphorylation – on the structure and function of Hsp42. My results show that Hsp42 undergoes a reversible oligomeric rearrangement in response to both heat and acidic pH, conditions commonly encountered by *S. cerevisiae* in its natural environment (Fig. 7A, 7B, 8). An increase in temperature correlates with a shift in chaperone activity, from forming small soluble complexes with specific substrates to forming large, light-scattering aggregates (Fig. 19). This transition is mediated by the IDD, as deletion of the IDD abolished aggregase activity while preserving holdase function (Fig. 29B, 29C).

Although the exact mechanism remains unclear, the IDD appears to play an indirect role in promoting large complex formation. It does not directly interact with substrate, as shown by cross-linking mass spectrometry, therefore it cannot increase substrate-binding valency. Rather, the IDD may serve as a scaffold for self-association of multiple Hsp42 oligomers, as suggested by extensive cross-linking between IDD regions or between IDD and ACD observed in cross-linking mass spectrometry (Fig. 14E).

Unfortunately, I was unable to establish a robust assay to directly assess Hsp42 activity across different pH conditions. Nevertheless, I speculate that pH reduction leads to protonation of negatively charged residues, and as a consequence in conformational changes that expose additional substrate-binding surfaces. Under these conditions, the formation of larger oligomers may stem from Hsp42 self-recognition. Such self-association likely does not occur *in vivo*, where misfolded substrates are abundant and preferentially sequestered by Hsp42. To test this hypothesis, a suitable model substrate must be identified – ideally one that is stable across a pH range but can be unfolded by a trigger other than heat, to isolate the pH effect *in vitro*.

I also screened eight phosphomimetic mutants of Hsp42, targeting residues previously identified as phosphorylated in proteomic studies. None of the variants displayed significant structural or functional changes *in vitro* (Fig. 9, S2). As of 2022, no published data had characterized Hsp42 phosphorylation. However, subsequent work by Ahmadpour et al. (2023) demonstrated that a single phosphomimetic substitution (S215D) delays the clearance of heat-induced protein aggregates *in vivo* and reduces refolding efficiency of heat-aggregated luciferase by ~25% *in vitro*. Furthermore, S215 phosphorylation was detected in aging cells, where it impairs aggregate handling. In contrast, my study used a triple phosphomimetic mutant (SSS213–215DDD) with a larger negative charge, which may account for discrepancies between the two findings.

Similarly, Plante et al. (2023) identified transient phosphorylation of Hsp42 at S223 during spore germination. They showed that the germination process in *hsp42Δ* spores is fully restored by expressing either wild-type Hsp42 or a phosphomimetic variant (S223E). In contrast, spores expressing the non-phosphorylatable S223A mutant show a noticeable delay in germination. This developmental transition involves a cytoplasmic pH drop to ~5.9, which

may also modulate Hsp42 activity, although the impact of pH was not explicitly assessed in my analysis of phosphomimetic variants.

These results underscore the importance of considering site specificity, phosphorylation extent, and the physiological context when interpreting the functional consequences of post-translational modifications. To more accurately map Hsp42 phosphorylation, I propose performing Hsp42 pull-downs followed by mass spectrometry to identify phosphoryled residues under diverse conditions: physiological growth, heat shock, and stationary phase (to mimic pH drop). This would enable rational design of phosphomimetic mutants to systematically investigate phosphorylation-dependent activation *in vitro*.

Altogether, these findings highlight the dynamic and condition-sensitive nature of Hsp42 function and the need for unconventional approaches to resolve its structural mechanism. For instance, cross-linking mass spectrometry could be employed under various stress conditions and in the presence or absence of substrate to identify structural rearrangements. For instance, Hsp42 could be cross-linked at 25 °C and 35 °C, and additionally in complex with insulin at the same temperatures, to compare contact patterns between small and large complexes. SAXS experiments performed under analogous conditions could further complement these insights and help elucidate oligomeric changes involved in activation.

4.4. Sequestrase activity of Hsp42 – complex formation with substrates

Hsp42 is capable of sequestering a wide range of substrates. The prion-like domain appears to contain key substrate-binding sites, one of which (residues ^{57}PLY^{59}) was identified through cross-linking mass spectrometry. However, with certain substrates such as malate dehydrogenase, I observed that even in the absence of the entire PrLD, Hsp42 retained some ability to interact with MDH. These interactions, however, were insufficient to support large complex formation equivalent to that seen with wild-type Hsp42 (Fig. 28B). In line with this, cross-links between other regions of Hsp42, specifically the ACD, and substrates were also identified (Fig. 21F, 21G), indicating that additional interaction sites contribute to substrate engagement. The small heat shock interaction with its substrate was indeed reported for some sHsp via the β4-β8 groove hydrophobic grove in the ACD (Mymrikov et al., 2015; Liu et al., 2018; Baughman et al., 2019).

Despite these insights, the overall architecture of Hsp42-substrate complexes remains unresolved. The only sHsp-substrate complex resolved at atomic resolution to date is that of *M. jannaschii* Hsp16.5 with lysozyme (Miller and Reichow, 2025). In this system, lysozyme is completely encapsulated within a spherical Hsp16.5 oligomer, which expands from a 24-mer to a 36-mer to accommodate the substrate. This model, however, does not appear applicable to Hsp42. If the AlphaFold-predicted planar octameric ring structure of Hsp42 is accurate, it would not offer sufficient internal volume to encapsulate substrates. Nevertheless, measurements indicate that Hsp42-substrate complexes are significantly larger than Hsp42 alone, having hydrodynamic radii of ~35 nm versus ~9 nm, respectively (Fig. 17B). This observation suggests that Hsp42 may undergo a substantial structural rearrangement upon substrate binding, potentially forming larger spherical oligomers capable of substrate encapsulation akin to Hsp16.5. To test this hypothesis, imaging approaches such as electron microscopy or cryo-EM would be necessary.

Alternatively, Hsp42 octamers could form mesh-like networks upon substrate binding. It may be especially relevant for aggregase activity of Hsp42 when the formed complexes have dimensions up to 1 µm. This could be experimentally examined by dynamic light scattering analysis at varying concentrations of both Hsp42 and the substrate. If mesh-like assemblies are formed, the complex size should scale with protein and substrate concentration, indicating concentration-limited polymerization. Ultimately, imaging confirmation will be important.

The architecture of Hsp42-Luci complexes, extensively investigated in my study, appears to differ from the model proposed for bacterial IbpA/B-Luci complexes by Żwirowski et al. (2017). Their biochemical data suggested a shell-core structure, with a dynamic outer layer and a more stably bound inner core of IbpA/B. In contrast, my results demonstrate that no Hsp42 molecules are passively released from Hsp42-Luci complexes over time, arguing against a similar shell-core organization for Hsp42. Instead, Hsp42 may stably entrap substrates within more homogeneous assemblies or a stable capsule similar to Hsp16.5.

4.5. Hsp42 – substrates complex dissolution by ATP-dependent chaperones

The architecture of Hsp42-substrate complexes likely plays a critical role in determining the efficiency of substrate disaggregation and refolding by ATP-dependent chaperone systems. While Hsp42 generally facilitates substrate disaggregation (Fig. 23), this effect is contingent upon the involvement of Hsp70. In contrast, disaggregation by the stand-alone disaggregase ClpG in the absence of the bacterial Hsp70, DnaK, was almost completely inhibited in the presence of Hsp42 (Fig. 33C). This suggests that Hsp42 may impose a structural constraint to complexes incompatible with ClpG activity. The IDD of Hsp42 appears to be a key modulator of this process. Deletion of the IDD impaired substrate refolding by the Hsp70-based disaggregation system, indicating that the IDD contributes positively to substrate processing in this context. However, the same deletion largely restored disaggregation by ClpG, implying that the IDD imposes a steric hindrance that interferes with direct substrate access by ClpG. Taken together, these findings suggest that the IDD may exert opposing effects on different chaperone systems – acting as a structural scaffold required for efficient handover to Hsp70, while simultaneously obstructing direct substrate engagement by ClpG. This highlights the importance of spatial and architectural considerations in chaperone-substrate interactions.

The interaction between Hsp70 and Hsp42 within substrate-bound complexes remains unresolved. Given that Hsp42 is not passively released from substrate complexes, it is tempting to hypothesize that Hsp70 actively engages with Hsp42 to facilitate its dissociation and to initiate substrate disaggregation and refolding. However, the prevailing view suggests that no direct interaction occurs between Hsp70 and small heat shock proteins.

My FRET-based experiments demonstrated that Ssa1 induces conformational changes in Hsp42 that are distinct from oligomer dissociation. However, direct physical interaction between the two proteins could not be confirmed by other experimental approaches. Nonetheless, interactions between Ssa1 and Hsp42 have been reported in proteome-wide interactome studies, including affinity purification coupled with mass spectrometry, and more recently through more targeted cross-linking mass spectrometry analyses (Gong et al., 2009; Nitika et al., 2022; Michaelis et al., 2023). Similarly, interactions between the bacterial Hsp70

homolog DnaK and the small heat shock proteins IbpA/B have been reported in the STRING interactome database. These observations suggest that interactions between Hsp70 and small heat shock proteins may be transient, low-affinity, or highly context-dependent, which could explain why Ssa1-Hsp42 interactions were not consistently detected across all experimental methods used in my study.

4.6. Screening of Hsp42 variants shows two distinct functions

To investigate the role of specific Hsp42 domains and motifs in oligomerization, substrate binding, and substrate transfer to ATP-dependent chaperones, a set of Hsp42 mutants and deletion variants was generated and analyzed (Fig. 25A). The structural and functional phenotypes of these variants are summarized in Table 2. The mutations fall into two main categories: those that impair substrate interaction and complex formation, and those that are deficient in the promoting substrate refolding by ATP-dependent chaperones, despite forming substrate complexes similar to the wild type.

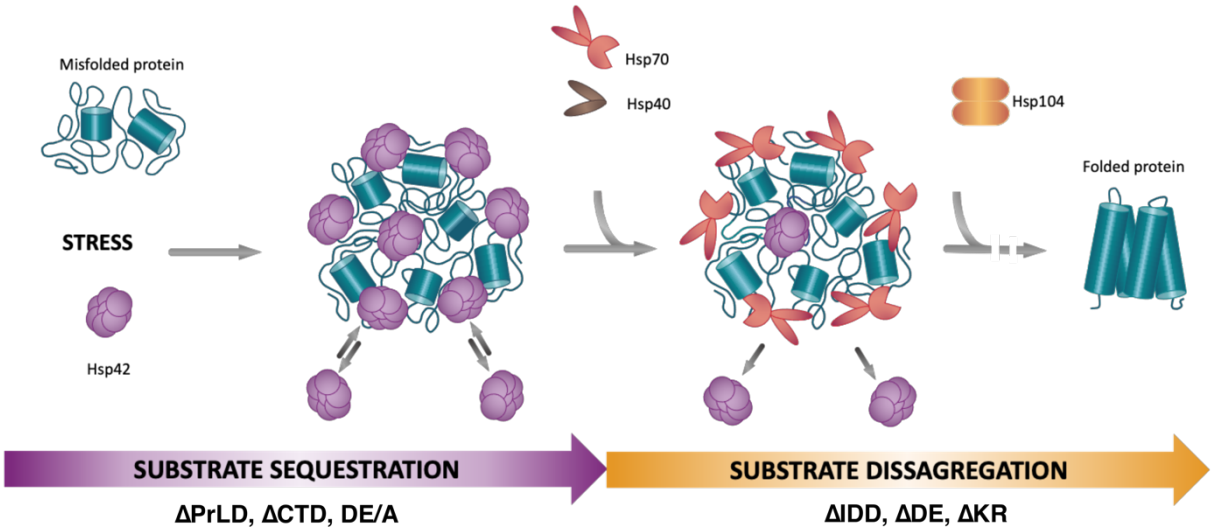

Figure 35. The model of misfolded protein sequestration by Hp42. Upon misfolding stress, Hsp42 binds to partially misfolded proteins and forms assemblies of different sizes. There is a constant dynamic exchange of Hsp42 on the assemblies. When the stress subsides, Hsp42 molecules are displaced by Hsp70. Hsp70 cooperates with Hsp104 for substrate disaggregation and subsequent refolding. Hsp42 variants ΔPrLD, ΔCTD, DE/A affected the substrate sequestration, while variants ΔIDD, ΔDE, ΔKR effectively sequester substrates but altered the substrate hand over to Hsp70 and subsequent refolding by ATP-dependent chaperones.

In the first group, the ΔPrLD variant represents the most direct effect: deletion of the PrLD, which harbors the main substrate-binding site, strongly reduces substrate interaction and thus chaperone activity. The DE/A variant similarly failed to function as a holdase and could not prevent Luciferase aggregation. Although its oligomeric state resembled that of wild-type Hsp42 (octamers), DE/A displayed significantly reduced thermal stability. The mutated residues reside in the C-terminal extension as predicted by AlphaFold; however, the confidence of this structural prediction is low, and it has not been experimentally validated.

Thus, the precise mechanism underlying the reduced thermal stability remains unclear. Similarly, ΔCTD showed a reduced thermal stability and impaired ability act as holdase. The underlying reason could be similar DE/A and requires more structural analysis.

The second group – comprising ΔIDD, ΔDE, and ΔKR – retained the ability to suppress Luciferase aggregation by forming complexes with the substrate, though the complex morphology differed from wild-type, as indicated by the decrease in hydrodynamic radius (Fig. 27B). These data suggest that the mutations impair the release of substrate, potentially by interfering with Hsp70-mediated extraction. In particular, ΔIDD highlights the importance of steric accessibility and Hsp42-substrate interactions for effective handover to Hsp70 and Hsp104.

Interestingly, the ΔKR variant was the only mutant to outperform wild-type Hsp42 in facilitating Luciferase refolding. This variant exhibited both increased substrate affinity and enhanced oligomeric dynamics. These features may allow ΔKR to be more readily displaced from Hsp42-substrate complexes by the downstream chaperone machinery, thereby improving substrate transfer and refolding efficiency.

Surprisingly, the Hsp42GxG variant formed larger oligomers at a concentration of 2.75 µM, as shown by SEC-MALS analysis. To my knowledge, mutations in this motif in other small heat shock proteins typically cause oligomer dissociation, since the conserved IxI motif plays a stabilizing role by interacting with the β4-β8 groove of an adjacent ACD dimer. In contrast, the results here suggest that in Hsp42, alterations to the IxI motif may enable alternative intra-oligomer contacts that still support oligomerization. However, these interactions appear less stable because Hsp42GxG dissociates into dimers at lower concentrations (100 nM; Fig. 26C). This supports the importance of the IxI motif in maintaining Hsp42 oligomer structure, which was also independently shown by cross-linking mass spectrometry.

The mutations in the IxI motif did not affect the chaperone function of Hsp42GxG. Its performance in all functional assays was similar to that of wild-type Hsp42. These assays were performed at Hsp42 concentrations from 50 nM to 1.5 µM, covering both dimeric and larger oligomeric species. These findings indicate that Hsp42 remains functional across its oligomeric states, again corroborating the relevance of oligomeric plasticity of oligomers and subunit exchange in its mode of action.

Altogether, the analysis of selected Hsp42 variants provides useful insight into its mechanism. However, the precise mechanism of Hsp42 activity remains to be defined, and more detailed studies are necessary to fully understand it.

	# protomer	Onset of aggregation (˚C)	Holdase activity	Aggregase activity	Luci refolding	Luci association kinetics	Oligomer dynamics
WT	8-10	67					
ΔPrLD	4	-					na
ΔIDD	61-76	-					
ΔDE	66-81	67					
ΔCTD	90-120	50				na	na
ΔKR	14-20	67					
DE/A	8-10	44				na	na
GxG	20	66				na	na

Table 2. **Summary of Hsp42 variants characterization.** All values are comparative to the wild-type Hsp42 (WT). Color legend: magenta – performed better/faster than WT, blue – performed worse/slower than WT, white – similar to WT. na – not analyzed. **Number (#) of protomers** in oligomers is determined by SEC-MALS at 10 μM injected concentration. **Onset of aggregation** was calculated based on the abrupt increase in the turbidity. **Holdase activity** refers to the ability to suppress thermal aggregation of Luciferase determined by light scattering and DLS. **Aggregase activity** refers to the ability to form large complexes with MDH based on the light scattering. **Luciferase refolding** means whether co-aggregation with Hsp42 variant facilitated or impaired Luciferase refolding by Ssa1/Ydj1/Hsp104. **Luciferase association kinetics** is determined by the speed of binding to aggregated Luciferase by BLI. **Oligomer dynamics** is determined by the dissociated rate of Hsp42 layer in BLI.

5. Material and Methods

5.1. Materials

Equipment

Equipment	Manufacture
Äkta pure 25	GE Healthcare
Agarose gel chambers	ZMBH workshop, University of Heidelberg
Balances: PG603-S, PB1502-S	Mettler Toledo, Satorius
Bio layer interferometry Octer K2	ForteBio
Centrifuge 5424	Eppendorf
Centrifuge Sorvall LYNX 6000, RC6	Thermo Scientific
Cell culture shaking incubators Multitron	Infors HT
Criterion™ Vertical Electrophoresis Cell	Bio-Rad
Electrophoresis power supply EV2650	Consort
Fluorescence Spectrometer FL 6500	PerkinElmer
French Pressure Cell	SLM/Aminco
GelDoc XR	Bio-Rad
Incubator	Sanyo
Lightcycler 480 II	Roche
Luminescence Spectrometer LS55	PerkinElmer
Luminometer Lumat LB 9507	Berthold Technologies
Magnetic stirrer MR 3001 K	Heidolph
MALS detector	WYATT Technology
Mass photometry TwoTM	Refeyn
Microwave KOR 6D07	VWR
NanoDrop ND-2000	Thermo Scientific
Novaspec Plus photometer	Biochrom Ltd
PCR machine FlexCycler2	Analytica Jena
pH-meter Orion Star A111	Thermo Scientific
Prometeus Panta	NanoTemper
Rotor F9-6 x 1000 LEX Fixed Angle	Thermo Scientific
Rotor T29-8 x 50	Thermo Scientific
Stopped Flow spectrometer	AppliedPhotophysics
Thermomixer comfort	Eppendorf AG
Transfer system Trans-Blot Turbo	Bio-Rad

Consumables

Item	Manufacture
Agarose Tablets, 0.5 g /tablet	Serva
Cellulose dialysis membrane	Repligen
Centrifuge tube, with screw cap, conical bottom, 15 and 50 ml	Sarstedt
Criterion TGX precast SDS gel	Bio-Rad
Ground bottom 5 ml PP tubes	Greiner
Leuer Lock syringers 1, 2.5, 5, 10, 50 ml	B. Barun
Needles Microlance™ 3	BD
Octet® NTA Biosensors	Sartorius
PCR strip of 8, 200 µl, PCR Performance Tested, transparent, PP	Sarstedt
Petri dish, PS, 60/15 mm, with vents	Greiner
Prometheus High Sensitivity Capillaries	Nanotemper
Protein Assay Dye Reagent Concentrate	Bio-Rad
PVDF membrane, Roti-PVDF	Roth
Reaction tube, PP 1.5 ml, brown, with lid	NeoLab
Reaction tubes, 1.5 ml, PP	Sarstedt
SafeSeal reaction tube, 1.5 ml, PP, PCR Performance Tested, Low protein-binding	Sarstedt
Syringe filter, Filtropur S, PES, pore size: 0.22 and 0.45 µm, for clear filtration	Sarstedt
SurePAGE™ Bis-Tris gels	GenScript
Trans-blot Turbo transfer packs	Bio-Rad
UV cuvette, 2.7 ml, (HxW): 45 x 12.5 mm, special plastic, transparent, optical sides: 2	Sarstedt
Whatman paper, 3 mm	Schleicher & Schuell

Chromatography columns

Column	Manufacture
GSTrap HP columns	Cytiva
MBPTrap HP	Cytiva
HiLoad 16/600 Superose 6 prep-grade	Cytiva
HiPre 26/10 Desalting column	Cytiva
PD SpinTrap G-25	Cytiva
Superdex 200 increase 3.2/300	Cytiva
Superose 6 Increase 10/300 GL	Cytiva

Kits

Kit	Manufacture
GenElute Gel Extraction Kit	Sigma-Aldrich
GenElute HP Plasmid Miniprep Kit	Sigma-Aldrich
GenElute PCR Clean-Up Kit	Sigma-Aldrich

Reagents

Item	Manufacture
Alexa Fluor™ 488 C_5 Maleimide	Invitrogen
Alexa Fluor™ 594 C_5 Maleimide	Invitrogen
Alexa Fluor™ 647 C_2 Maleimide	Invitrogen
ATP	Sigma-Aldrich
Aquicide II	Millipore
cOmplete, EDTA free protease inhibitor tablets	Roche Diagnostics
dATP, dCTP, dGTP, dTTP	Thermo Scientific
DL-Dithiothreitol (DTT)	Sigma-Aldrich
DNA ladder 1 kb Gene Ruler	Thermo Scientific
DHSO	Sigma-Aldrich
DMTMM	Sigma-Aldrich
DSSO	Sigma-Aldrich
Gel Filtration Molecular Weight Standard	Bio-Rad
Isopropyl-β-D-thiogalactopyranosid (IPTG)	Roth
Luciferin	AppliChem GmbH
PageRuler™ Prestained Protein Ladder	ThermoFisher Scientific
Phospho(enol)pyruvic acid trisodium salt hydrate	Sigma-Aldrich
SYPRO™ Ruby Protein Gel Stain	Invitrogen
SYPRO™ Ruby Protein Gel Stain	Invitrogen
TCEP	Sigma-Aldrich
Quick Coomassie Stain	ProteinArk

Antibiotics

Antibiotics	Final concentration	Manufacture
Ampicillin	100 µg/ml	Carl Roth
Gentamicin	20 µg.ml	Carl Roth
Kanamycin	50 µg/ml	Carl Roth
Chloramphenicol	50 µg/ml	Sigma-Aldrich

Enzymes and Proteins:

Proteins	Manufacture
Bovine Serum Albumin	Sigma-Aldrich
Citrate synthase	Sigma-Aldrich
DNAse I	Roche
Firefly luciferase	Lab stock
His-Ssa1	Liberek lab, University of Gdansk
His-Luciferase	Liberek lab, University of Gdansk
Hsp104	Lab stock
Insulin	Sigma-Aldrich
Malate dehydrogenase	Merck
OptiTaq DNA Polymerase	Roboklon
Phusion DNA Polymerase	ThermoFisher Scientific
Proteinase K	Blirt
Restriction enzymes (BamHI, Eco105I, XhoI, Cfr9I, NdeI, DpnI)	ThermoFisher Scientific
Ssa1	Lab stock
T4 DNA Ligase	ThermoFisher Scientific
Ydj1	Lab stock

Media

All media were autoclaved at 121 °C, at 1.05 bar, for 20 minutes. For the preparation of agar plates the medium was supplemented with 2% (w/v) agar prior to autoclaving.

Medium	**Composition**
LB (Luria-Bertani) medium	10 g/L Tryptone 5 g/L Yeast extract 5 g/L NaCl
2x YT (Yeast Tryptone) medium	16 g/L Tryptone 10 g/L yeast extract 5 g/L NaCl

Standard buffers

Buffer	**Composition**
10X TBE buffe	900mM Tris base 900mM boric acid 20mM EDTA
4xSDS-sample buffer	200 mM Tris pH=6.8, 400 mM DTT 8 % SDS 0.4 % bromphenol blue 40 % glycerol
10xSDS-running buffer	25 mM Tris 193 mM glycine 0.1% SDS
TBS-T	10 mM Tris 150 mM NaCl pH adjusted to 8.0 with HCl 0.5% (v/v) Tween-20

Bacterial strains

Strain	**Genotype**	**Manufacture**
E. coli XL1-Blue cells	*recA1 endA1 gyrA96 thi-1 hsdR17 supE44 relA1 lac* [F *proAB lacI*^{q}*ZΔM15* Tn*10* (Tet^{r})]	Agilent
E. coli ArcticExpress (DE3)	B F $^{-}$ *ompT hsdS*(rB $^{-}$ mB $^{-}$) *dcm*+ Tet^{r} *gal λ*(DE3) *endA* Hte [*cpn10 cpn60* Gent^{r}]	Agilent
E.coli Rosetta (DE3)	F^{-} *ompT hsdS*$_{B}$(r_{B}^{-} m_{B}^{-}) *gal dcm* (DE3) pRARE (Cam^{r})	Novagen

Software and online tools

Software and online tool	Provider
AlphaFold Server	Google DeepMind https://alphafoldserver.com/
ASTRA	WYATT Technology
CIDER	Pappu lab at Washington University in Saint Louis https://pappulab.wustl.edu/CIDER/
ChimeraX	Resource for Biocomputing, Visualization, and Informatics (RBVI) at University of California San Francisco
DSF world	Gestwicki lab at University of California San Francisco https://gestwickilab.shinyapps.io/dsfworld/
Fiji	The Fiji/ImageJ community
Inkscape	Inkscape Project Leadership Committee
IUPred3	Zsuzsanna Dosztányi lab at ötvös Loránd University https://iupred3.elte.hu/
Office 365	Microsoft
R Studio	Posit, PBC
SnapGene Viewer	GSL Biotech LLC
xiVIEW	Pappsilber lab at Technical University Berlin https://xiview.org/index.php

Plasmids

#	Plasmid	Antibiotic	Source
1	pMal-c2E-hsp42_FLAG	Amp	pSU34, Ungelenk PhD thesis
2	pMal-c2E-hsp42	Amp	This study
3	pMal-c2E-hsp42_ΔPrLD	Amp	This study
4	pMal-c2E-hsp42_ΔCTD	Amp	This study
5	pMal-c2E-hsp42_Δ356-375	Amp	This study
6	pMal-c2E-hsp42_I353X-I355X	Amp	This study
7	pGEX-6P-1-preScission	Amp	Lab
8	pUC57-BsaI-Free-hsp42_DE	Amp	BioCat
9	pUC57-BsaI-Free-hsp42_IDD	Amp	BioCat
10	pUC57-BsaI-Free-hsp42_KR	Amp	BioCat
11	pMal-c2E-hsp42_ΔIDD	Amp	This study
12	pMal-c2E-hsp42_ΔDE	Amp	This study
13	pMal-c2E-hsp42_ΔKR	Amp	This study
14	pMal-c2E-hsp42_GEE360-362AAA	Amp	This study
15	pMal-c2E-hsp42_GEE360-362AAA_E366A	Amp	This study
16	pMal-c2E-hsp42_GEE360-362AAA_E366A_EE356-357AA	Amp	This study
17	Ssa1 plasmid	Kan	Lab collection
18	Hsp104 plasmid	Kan	Lab collection
19	pMal_c2E-hsp42_S81C	Amp	This study
20	pMal_c2E-hsp42_ΔIDD_S81C	Amp	This study
21	pDS56 MDH-His	Amp	Lab collection
22	pMal_c2E-hsp42_S81C_C127A	Amp	This study
23	pMal-c2E-hsp42_Y4W	Amp	This study
24	pMal-c2E-hsp42_Y71W	Amp	This study
25	pMal-c2E-hsp42_Y80W	Amp	This study
26	pMal-c2E-hsp42_Y29W	Amp	This study
27	pMal-c2E-hsp42_Y39W	Amp	This study
28	pPROEX-6His-TEV-Sis1	Amp	Liberek, University Gdansk
29	pMal-c2E-hsp42_C127A	Amp	This study
30	pMal-c2E-hsp42_C127A_T254C	Amp	This study

Primers

#	Name	Sequence
1	Hsp42WT_Xmal_fw	gatccccgggatgagtttttatcaaccatcc
2	Hsp42_dPrLD_Xmal_START_fw	gactcccgggatggatgacgaggatggtgaagaaga
3	Hsp42_dCTD_STOP_BamHI_rw	gactggatcctcacggcttttcagtgtcattgacaa
4	Hsp42_d355-375_STOP_BamHI_rw	gactggatcctcaaatggcgatcctctttttggct
5	Hsp42WT_IXI/GXG_fw	aagccaaaaaagaggggcgccggtgaggaaatacccg ac
6	Hsp42_IXI/GXG_rw	gtcgggtatttcctcaccggcgcccctctttttggctt
7	pMal-c2E_seq_fw	gactgtcgatgaagccctg
8	pMal-c2E_seq_rw	cagggttttcccagtcacg
9	Hsp42_E/A_midl_fir st_fw	ggaaatacccgccgcagcattggagtttgaag
10	Hsp42_E/A_midl_fir st_rw	tcaatggcgatcctctttttggcttcgg
11	Hsp42_E/A_rig_sec st_fw	agcattggagtttgcagaaaatcccaaccc
12	Hsp42_E/A_rig_sec st_rw	tcgtcgggtatttcctcaatggcgatcctc
13	Hsp42_E/A_le_thi st_fw	gaggatcgccattgcggcaatacccgccgcag
14	Hsp42_E/A_le_thi st_rw	ttttttggcttcggcttttcagtgtcattgac
15	Hsp42_S81D_fw	caagcctattactatgatcctgaatacggt
16	Hsp42_S81D_rw	tccagggaactggtagtaataggtattag
17	Hsp42_S116D_S118D_fw	gatggtggcgaggacgacaacgatagaagatatccatc
18	Hsp42_S116D_S118D_rw	ttcctgtcttgtagtgccgctgtcaccca
19	Hsp42_S123D_fw	cgatagaagatatccagattattaccattgt
20	Hsp42_S123D_rw	ttgctgtcctcgccaccatcttcctg
21	Hsp42_S141D_fw	ccaacaggcaaacgatttaaacgacttat
22	Hsp42_S141D_rw	ttggtcctattattcctggcagtattac
23	Hsp42_S182D_fw	gataagaaggataaggatgaagcacccaaag
24	Hsp42_S182D_rw	cttttcttctccctttcgccctcctg
25	Hsp42_S205D_fw	gctggaggaatcggatagaccaccattag
26	Hsp42_S205D_rw	tgattcaaaggtttttctttgttgg
27	Hsp42_S213D_S214D_S215D_fw	ccattagccaaaaaagatgatgatttcgctcacctacaag
28	Hsp42_S213D_S214D_S215D_rw	tggtctcgacgattcctccagctgattcaaaggtttttc
29	Hsp42_S223D_fw	cacctacaagcgcctgacccaatacctgac
30	Hsp42_S223D_rw	agcgaacgatgaagatttttttggctaatg
31	Hsp42_S232D_fw	cccgttacaagtagacaagcctgaaacg
32	Hsp42_S232D_rw	tcaggtattggggaaggcgcttgtaggt
33	Hsp42_T344E_fw	ctaaaattgtcaatgacgaagaaaagccgaag
34	Hsp42_T344E_rw	gcaccttaatttgtagtagaccgttgttg
35	Hsp42_S81C_fw	caagcctattactattgtcctgaatacggt
36	Hsp42_S81C_rw	tccagggaactggtagtaataggtattag
37	sis1_700_fw	agaaccagggtgattacaatcc
38	Hsp42WT_C127A_fw	catcatattaccatgctaatactgccagg
39	Hsp42WT_C127A_rw	gatatcttctcgagttgctgtcctcg
40	Hsp42_Y4W_fw	gttcatgagtttttggcaaccatccctatc

41	Hsp42_Y4W_rw	ccgggtacgggcccctggaag
42	Hsp42_Y71W_fw	ctaatacctattactggcagttccctggac
43	Hsp42_Y71W_rw	gaacaccattgtatctgctatac
44	Hsp42_Y80W_fw	caagcctattactggagtcctgaatacggt
45	Hsp42_Y29W_fw	gggcagcaaggatggcctcgccaaccac
46	Hsp42_Y29W_rw	tctctggccagtttggttggataatg
47	Hsp42_Y39W_fw	ggccacagagatggcatccccattatgg
48	Hsp42_Y39W_fw	tttgtggttggcgaggatatcc
49	sis1_100seq_rw	gtcacctgttggcttatctgg
50	Hsp42_T254C_fw	gataccgaggactgttacgtagttgttc
51	Hsp42_T254C_rw	atagacattcacttctggtgaaaatg

5.2. Methods

5.2.1. Molecular cloning

All primers were ordered from Merck, and the restriction enzymes were purchased from ThermoFisher. Cloning steps were performed in *E. coli* XL1-Blue cells in LB medium. The parental plasmid to clone all Hsp42 mutants was pMal-c2E-Hsp42-FLAG from the Ungelenk et al. (2016) study.

For long mutant deletions at either the 5' or 3' ends of the hsp42 gene, the insert was amplified from the parental plasmid by PCR using primers with overhangs containing restriction enzyme recognition sites, with Phusion High-Fidelity DNA Polymerase. Both the PCR-amplified insert and the parental vector were digested with the same restriction enzymes.

For deletions within the hsp42 gene, the deleted region was replaced with a nucleotide stretch that was chemically synthesized and provided in the pUC57-BsaI-Free plasmid (BioCat). Both the pUC57-BsaI-Free insert and the parental plasmids were digested with restriction enzymes. Following enzymatic digestion, the vector and the insert were resolved on a 1% agarose gel (ThermoScientific), and the band of the desired length was excised and purified using a Gel Extraction Kit (Sigma-Aldrich). The vector and insert were ligated with T4 DNA Ligase and transformed into competent cells, which were plated on LB-agar plates supplemented with the appropriate antibiotic. Correct mutagenesis was confirmed by isolating plasmids from *E. coli* colonies and performing sequencing at Microsynth AG.

For point mutations, 5' end-phosphorylated outward-facing primers with no overlap were used, with one primer containing the mutation. PCR was performed using OptiTaq polymerase to amplify the entire parental plasmid. The non-amplified parental plasmid was then digested with DpnI, followed by ligation, transformation into *E. coli* cells, and sequencing of the isolated plasmids to confirm the point mutations.

5.2.2. Protein purification

Hsp42 and variants

3 L of 2×YT medium supplemented with ampicillin and gentamicin was inoculated with an overnight culture of *E. coli* ArcticExpress (DE3) cells carrying the *pMal-c2E* plasmid with inserted the *hsp42* gene fused with an MBP tag, and incubated at 30°C and shaking at 120 rpm. When the culture reached an OD_{600} of 0.8, Hsp42 expression was induced by the addition of IPTG to a final concentration of 0.5 mM. The culture was then incubated overnight at 13°C, and shaking at 120 rpm.

The following day, cells were harvested by centrifugation at 4,500 rpm for 15 minutes using Rotor F9-6 x 1000 LEX Fixed Angle. Cell lysis was performed using a French press at 1,000 psi in 50 mL of Hsp42 Purification Buffer (40 mM Tris-HCl, 150 mM NaCl, 7% glycerol, pH = 7.4) supplemented with an EDTA-free protease inhibitor cocktail tablet. The lysate was cleared by centrifugation at 17,000 rpm for 1 hour at 4°C using Rotor T29-8 x 50. The

supernatant was treated with DNaseI (final concentration 5µg/mL) and loaded onto two sequentially connected 5 mL MBPTrap columns.

MBP-Hsp42 was eluted with the Hsp42 Purification Buffer supplemented with 20 mM Maltose. Eluted MBP-Hsp42 fractions were collected and incubated overnight at 4°C with PreScission protease (final concentration 0.8 µM) to remove the MBP tag. The next day, the sample was centrifuged at maximum speed in a bench-top centrifuge for 15 minutes at 4°C. The supernatant was injected onto a HiLoad 16/600 Superose 6 prep-grade column and purified in the Hsp42 Purification Buffer. Fractions containing purified Hsp42 were analyzed by SDS-PAGE, pooled, and flash-frozen in liquid nitrogen for further use.

PreScission

3 L of LB medium supplemented with ampicillin and chloramphenicol was inoculated with the overnight E.coli Rosetta (DE3) carrying the pGEX-6P-1 plasmid with the inserted PreScission gene and incubated at 37°C and shaking at 120 rpm. When the culture reached an OD_{600} of 0.5, PreScission expression was induced by the addition of IPTG to a final concentration of 0.5 mM. The culture was then incubated overnight at 37°C and shaking at 120 rpm.

The following day, cells were harvested by centrifugation at 4,500 rpm for 15 minutes using Rotor F9-6 x 1000 LEX Fixed Angle. Cell lysis was performed using a French press at 1,000 psi in 50 mL of PreScission Lysis Buffer (10 mM Na2HPO4, 1.8 mM KH2PO4, 140 mM NaCl, 2.7 mM KCl, 1 mM EDTA, 1 mM DTT, 1 tablet EDTA-free protease inhibitor cocktail, pH = 7.3). The lysate was cleared by centrifugation at 17,000 rpm for 1 hour at 4°C using Rotor T29-8 x 50. The supernatant was treated with DNaseI (final concentration 5µg/mL) and loaded onto two sequentially connected 5 mL GSTrap HP columns.

PreScission was eluted with the PreScission Elution Buffer (50 mM Tris-HCl, 10 mM reduced glutathione, 1 mM DTT, pH = 7.4). Eluted PreScission fractions were collected and injected onto HiPrep™ 26/10 Desalting column to exchange buffer into PreScission Storage Buffer (50 mM Tris-HCl, 150 mM NaCl, 1 mM EDTA, 1 mM DTT, 7% glycerol, pH = 7.4). Fractions containing purified PreScission were analyzed by SDS-PAGE, pooled, and flash-frozen in liquid nitrogen for further use.

Sis1 purification

3 L of 2×YT medium supplemented with ampicillin and chloramphenicol was inoculated with an overnight culture of *E. coli* Rosetta (DE3) carrying the pPROEX plasmid harboring the sis1 gene fused with the 6xHis tag, and incubated at 30°C and shaking at 120 rpm. When the culture reached an OD_{600} of 0.5, Sis1 expression was induced by the addition of IPTG to a final concentration of 1 mM. The culture was then incubated for three hours at 30°C, and shaking at 120 rpm.

The cells were harvested by centrifugation at 4,500 rpm for 15 minutes using Rotor F9-6 x 1000 LEX Fixed Angle. Cell lysis was performed using a French press at 1,000 psi in 50 mL of Sis1 Lysis Buffer (50 mM HEPES-KOH, 50 mM KCl, 5mM b-mercaptoethanol, 10%

glycerol, 1 tablet EDTA-free protease inhibitors, pH = 8.0). The lysate was cleared by centrifugation at 17,000 rpm for 1 hour at 4°C using Rotor T29-8 x 50. The supernatant was treated with DNase (final concentration 5µg/mL) and loaded onto a 5 mL HisTrap ™ FF crude column. 6xHis-Sis1 was eluted with the Sis1 Elution Buffer (50 mM HEPES-KOH, 500 mM KCl, 5mM b-mercaptoethanol, 10% glycerol, 500 mM imidazole, pH = 8.0). Eluted 6xHis-Sis1 fractions were collected and injected onto HiPrep™ 26/10 Desalting column to exchange buffer into Sis1 Storage Buffer (50 mM HEPES-KOH, 300 mM KCl, glycerol 10%, pH = 8.0). Fractions containing purified 6xHis-Sis1 were analyzed by SDS-PAGE, pooled, and flash-frozen in liquid nitrogen for further use.

5.2.3. General molecular biology methods

Determination of protein concentration

Protein concentrations were determined with the Bradford assay by using Protein Assay Dye Reagent Concentrate, following the manufacturer's instructions, unless it is states otherwise. BSA was used to create a standard curve (Bradford, 1976).

Protein concentration

All proteins were concentrated using Aquacide II powder (Millipore). The protein solution was transferred into a dialysis membrane with an appropriate molecular weight cut-off (MWCO), sealed with clamps on both ends, and completely buried in Aquacide II powder. Concentration was carried out at 4 °C with gentle shaking until the desired concentration was achieved.

Agarose gel electrophoresis

DNA fragments were separated using agarose gel electrophoresis. Agarose was dissolved in 0.5×TBE buffer to prepare 1% gels The agarose solution was heated until fully dissolved and allowed to cool to approximately 50–60 °C. 1 µL StainG (Serva) per 50mL was added prior to casting the gel. Gels were poured into casting trays with combs and allowed to solidify at room temperature.

DNA samples were mixed with 6 x TriTrack DNA gel loading buffer (ThermoFischer) and loaded into the wells. Electrophoresis was performed in 0.5×TBE running buffer at 150 V until the dye runs till the gel bottom. After electrophoresis, DNA was visualized using in the GelDoc system with UV transillumination.

SDS Polyacrylamide Gel Electrophoresis (SDS-PAGE)

Proteins were separated by SDS Polyacrylamide Gel Electrophoresis. Protein samples were mixed with 4× SDS-sample buffer to achieve a final concentration of 1×, then boiled at 95 °C for 5 minutes. Samples were loaded onto precast Criterion TGX gels (Bio-Rad) or SurePAGE™ Bis-Tris gels (GenScript) with an appropriate polyacrylamide percentage. Electrophoresis was performed at 200 V using SDS running buffer for Criterion TGX gels or Tris-MOPS SDS buffer for Bis-Tris gels, until the dye front reached the bottom. Gels were briefly rinsed with deionized water prior to staining.

SDS-PAGE Staining with Coomassie Blue

A small volume of Quick Coomassie protein stain (ProteinArk) solution was added to fully cover the gel. The gel was heated in a microwave at 1000 W for 30 seconds and then incubated at room temperature with gentle shaking for 1 hour. After staining, the solution was discarded, and the gel was washed twice with deionized water for 1 hour each.

SDS-PAGE Staining with SYPRO Ruby

Gels were fixed in a solution of 50% ethanol and 7% acetic acid for 60 minutes at room temperature with gentle shaking. After fixation, the solution was discarded and enough SYPRO™ Ruby stain (Invitrogen) was added to cover the gel completely. Staining was carried out overnight at room temperature with gentle shaking in a light-protected container. The following morning, the stain was discarded, and the gel was washed twice for 30 minutes with a solution of 10% ethanol and 7% acetic acid. Stained gels were visualized using a GelDoc system with UV transillumination.

Western blot analysis

After separation by SDS-PAGE, proteins were transferred onto polyvinylidene fluoride (PVDF) membranes using the Bio-Rad Trans-Blot Turbo system following the manufacturer's instructions. Membranes were blocked for 30 minutes at room temperature in 3% bovine serum albumin (BSA) dissolved in TBS-T buffer to prevent nonspecific binding.

After blocking, membranes were incubated with the primary antibody diluted in TBS-T for 1 hour at room temperature with gentle shaking. Following three washes with TBS-T (5 minutes each), membranes were incubated overnight at 4 °C with an appropriate horseradish peroxidase (HRP)-conjugated secondary antibody, also with gentle shaking.

The next morning, membranes were washed three times with TBS-T (5 minutes each). They were then incubated with ECL substrate solution (GE Healthcare) for 10 minutes to enable protein visualization. Excess liquid was gently removed by blotting the membranes on Whatman paper. Protein bands were detected by capturing the chemiluminescent signal using a LAS-4000 imaging system.

5.2.4. Structural methods

Electron Microscopy

For all Electron Microscopy imaging protocols including sample freezing for cryo-EM, gradual fixation protocol, data acquisition and data analysis refer to the lab of Stefan Pfeffer (ZMBH, University of Heidelberg). Cross-linking by DSSO protocol used for EM is described in the "Cross-linking mass spectrometry" section.

AlphaFold Prediction

The three-dimensional structure of Hsp42 octamer was predicted using AlphaFold3 (DeepMind) (https://alphafoldserver.com/). The input sequence was provided in FASTA format, and default parameters were used. The best-scored models were analyzed and visualized by ChimeraX software.

Minimal fluorescence photon fluxes microscopy (MinFlux)

Hsp42-C127A/T254C was labeled with Alexa Fluor 488 as described in the "Förster Resonance Energy Transfer (FRET) Assay" section. Labeling with Alexa Fluor 647 was performed in 40 mM HEPES, 300 mM NaCl, pH 7.4 by incubating the protein with a 5-fold molar excess of dye for 8 hours at 35 °C, followed by overnight incubation at 8 °C with shaking at 350 rpm. To remove unbound dye, the protein samples were buffer-exchanged four times into 40 mM HEPES, 150 mM NaCl, pH 7.4 using PD SpinTrap™ G-25 columns.

Protein concentration and degree of labeling were determined as described in the "Förster Resonance Energy Transfer (FRET) Assay" section, using A_{max} = 650 nm, CP = 0.03, and ε_{dye} = 265,000 $M^{-1}cm^{-1}$.

The labelled protein was cross-linked with DSSO as described in the "Cross-linking Mass Spectrometry" section. The protein was then immobilized on plasma-cleaned, polylysine-coated microscopy slides by incubation at room temperature for 10 minutes, followed by washing with PBS buffer. Imaging was performed in GLOX buffer supplemented with varying concentrations of MEA (2–50 mM) or βME (143 mM). For the image acquisition protocol, refer to Dr. Charlotte Kaplan (BioQuant, University of Heidelberg).

5.2.5. Biophysical methods

Nano-differential scanning fluorimetry (nanoDSF)

NanoDSF coupled to turbidity measurement was performed in Prometeus Panta (Sinning lab, BZH, University of Heidelberg) using high-sensitivity capillaries. Proteins were diluted to the concentrations indicated in the Results in 40 mM HEPES-NaCl, 150 mM NaCl, 2 mM DTT, pH = 7.4. The unfolding was recorded from 20 to 75 degrees at a 1˚C min ramp speed. The transition temperatures were calculated with the built-in Prometeus Panta software.

Dynamic light scattering (DLS)

NanoDSF coupled to turbidity measurement was performed in Prometeus Panta (Sinning lab, BZH, University of Heidelberg) using high-sensitivity capillaries. Proteins were diluted to the concentrations indicated in the Results in 40 mM HEPES-NaCl, 150 mM NaCl, 2 mM DTT, pH = 7.4 and measured with the default high sensitivity mode. The hydrodynamic radius and polydispersity index values were determined using the built-in Prometheus Panta software. Upon measurement of the cumulant hydrodynamic radius was measured recorded from 20 to 75 degrees at a 1˚C min ramp speed.

Thermal shift assay with SyproOrange

To determine the protein thermal transitions, the protein was mixed with SYPRO™ Orange stain (Invitrogen) by diluting the original stock 80 times in 40 mM HEPES, 150 mM NaCl, pH = 7.5. The protein concentration was 10 μM. The fluorescence nm was recorded from 25 to 75˚C at a 1˚C/min ramp speed using LightCycler 480 II (Roche). The apparent melting temperatures were determined online on https://gestwickilab.shinyapps.io/dsfworld/ by sigmoid fitting.

Mass Photometry

The molecular weight of Hsp42 samples was determined by measuring 100 nM of proteins in 40 mM HEPES, 150 mM NaCl, pH = 7.4 using a TwoMP instrument (EMBL, Heidelberg, Protein Expression and Purification Core Facility). The protein sample was prior centrifuges at 14000 xg for 15 minutes. The buffer was filtered. The molecular masses were calculated by the in-built TwoMP software.

Analytical size exclusion chromatography (aSEC)

Oligomerization of Hsp42 was determined by size exclusion chromatography using Superose 6 Increase 10/300 GL following a manufacturer's protocol in 40 mM HEPES, 150 mM NaCl, pH = 7.4. The injected protein concentration was 10 μM. Chromatography runs were performed at 8˚C. Elution fractions were analyzed via SDS-PAGE followed by staining with SYPRO™ Ruby stain according to manufacturer protocols.

Size exclusion chromatography coupled to multi-angle light scattering (SEC-MALS)

SEC-MALS measurements were performed in the Sinning lab (BZH, University of Heidelberg) using their Äkta Pure 25 and light scattering instrument DAWN HELEOS 8. 10 µM of Hsp42 was incubated at room temperature for 15 minutes and 50 µl was injected onto the Supe 200 increase 3.2/300 column and run at room temperature in 40 mM HEPES, 150 mM NaCl, 1 mM DTT, pH = 7.5 with the flow rate 0.07 ml/min. The data analysis was performed in ASTRA software. Molecular weight was calculated by fitting the Zimm model with the best fit degree. The concentration of eluted protein was calculated using the formula:

$$c = \frac{dRI_{max\ peak\ signal} - dRI_{baseline}}{\frac{dn}{dc}},$$

where dRI is a differential refractive index and dn/dc is a refractive index increment of the Hsp42 which equals to 0.186465789.

Bio layer interferometry (BLI)

BLI experiments were performed in the Liberek lab (University of Gdańsk) using an Octet K2 instrument (Sartorius). The BLI buffer contained 25 mM HEPES, 75 mM KCl, and 15 mM $MgCl_2$, pH 8.0. Octet NTA biosensors (Sartorius) were used for all experiments. Upon BLI recording the sensor was shaken at 1000 rpm.

To assess the affinity of Hsp42 variants for aggregated Luciferase, Luciferase was aggregated directly on the sensor surface in the bench Thermomixer. Sensors were incubated in urea-denatured His-tagged Luciferase (0.5 µg/µl in BLI buffer supplemented with 5.2 M urea) for 10 minutes at room temperature with shaking at 400 rpm. Following this, sensors were washed in BLI buffer (without urea) for 5 minutes at room temperature and subsequently incubated in native Luciferase (0.1 µg/µl in BLI buffer) at 44 °C for 10 minutes. After a final wash in BLI buffer for 5 minutes, the sensors were ready for measurement.

For affinity measurements, 1 µM of each Hsp42 variant in BLI buffer supplemented with 2 mM DTT was pre-incubated at 37 °C for 15 minutes. The Luciferase-coated sensors were then immersed in the Hsp42 samples and association was recorded for 20 minutes at 37 °C. Dissociation was monitored by immediately transferring the sensors into fresh BLI buffer containing 2 mM DTT and recording for another 20 minutes under the same conditions.

The association and dissociation rates were calculated by fitting the respective phases to a two-phase exponential association and dissociation model, respectively. The rate of the fast phase (k_1) is shown in Results.

$$Binding = C_1 \cdot (1 - e^{-k1 \cdot Time}) + C_2 \cdot (1 - e^{-k2 \cdot Time}) + C_0 \quad \text{(association)}$$

$$Binding = C_1 \cdot (e^{-k1 \cdot Time}) + C_2 \cdot (e^{-k2 \cdot Time}) + C_0 \quad \text{(dissociation),}$$

where C_0 is Luciferase thickness at Time = 0; C_1, C_2 are amplitudes of thickness in each phase; k_1, k_2 are respective rate constants of Hsp42 binding.

Förster Resonance Energy Transfer (FRET) Assay

For labeling, Hsp42 was buffer-exchanged into 40 mM HEPES, 150 mM NaCl, pH 7.4 using PD SpinTrap™ G-25 buffer exchange columns according to the manufacturer's protocol. Hsp42 was labeled with Alexa Fluor 488 (Donor) or Alexa Fluor 594 (Acceptor) by incubating approximately 150 µl of protein (at ~100 µM concentration) with a two-fold molar excess of the respective fluorophore dye for 2 hours at 25 °C with shaking at 350 rpm. To remove unbound dye, the protein samples were buffer-exchanged twice into 40 mM HEPES, 150 mM NaCl, pH 7.4 using fresh PD SpinTrap™ G-25 columns. The protein concentration and the degree of labeling (DOL) was calculated by measuring the protein absorbance at 280 nm (A280), and protein absorbance at the wavelength maximum for the dye molecule (A_{max}), which is 495 nm for Alexa Fluor 488 and 590 nm for Alexa Fluor 594.

$$\text{Protein concentration} = \frac{A_{280} - (A_{max} \cdot CF)}{\varepsilon_{prot}} \cdot MW$$

where CF is a correction factor, which is 0.11 for Alexa Fluor 488 and 0.56 for Alexa Fluor 594, and ε_{prot} is an extinction coefficient of Hsp42 which equals to 35750 $M^{-1}cm^{-1}$. MW – molecular weight of Hsp42 (43260 Da).

$$DOL = \frac{MW}{\text{Protein concentration}} \cdot \frac{A_{max}}{\varepsilon_{dye}}$$

where ε_{dye} is an extinction coefficient of a dye, which is 72000 $M^{-1}cm^{-1}$ for Alexa Fluor 488 and 96000 $M^{-1}cm^{-1}$ for Alexa Fluor 594.

FRET measurements were performed using a stopped-flow spectrometer. For all experiments, the excitation wavelength was set to 477 nm, and acceptor fluorescence was recorded using a 590 nm filter. The standard buffer used for all measurements was 40 mM HEPES, 150 mM NaCl, pH 7.4. For experiments involving Ssa1, the buffer was supplemented with 2 mM $MgCl_2$.

To assess subunit exchange, donor-labeled Hsp42 and acceptor-labeled Hsp42 were mixed at equimolar concentrations (0.2 µM, 0.5 µM, or 1 µM each) and immediately measured. Raw FRET data were fitted to different exponential association models to determine the best-fit kinetic parameters describing the subunit exchange process:

$\text{Fluorescence} = C \cdot (1 - e^{-k \cdot Time}) + C_0$ (first order)

$\text{Fluorescence} = C_1 \cdot (1 - e^{-k1 \cdot Time}) + C_2 \cdot (1 - e^{-k2 \cdot Time}) + C_0$ (second order)

$\text{Fluorescence} = C_1 \cdot (1 - e^{-k1 \cdot Time}) + C_2 \cdot (1 - e^{-k2 \cdot Time}) + C_3 \cdot (1 - e^{-k3 \cdot Time}) + C_0$ (third order),

where C_0 is fluorescence at Time = 0; C, C_1, C_2, C_3, are amplitudes of fluorescent change in each phase; k, k1, k2, k3 are respective rate constants.

For subunit dissociation experiments, hetero-labeled Hsp42 oligomers were prepared by incubating donor-labeled Hsp42 with acceptor-labeled Hsp42 at equimolar concentrations for 1 hour at 25 °C. To initiate dissociation, the preformed hetero-labeled oligomers were mixed with a five-fold molar excess of unlabeled Hsp42 and immediatelymeasured. Dissociation was monitored as a decrease in FRET efficiency over time, and the resulting data were analyzed using exponential decay models of different order to extract kinetic parameters:

$$\text{Fluorescence} = C \cdot (e^{-k \cdot Time}) + C_0 \quad \text{(first order)}$$

$$\text{Fluorescence} = C_1 \cdot (e^{-k1 \cdot Time}) + C_2 \cdot (e^{-k2 \cdot Time}) + C_0 \quad \text{(second order)}$$

$$\text{Fluorescence} = C_1 \cdot (e^{-k1 \cdot Time}) + C_2 \cdot (e^{-k2 \cdot Time}) + C_3 \cdot (e^{-k3 \cdot Time}) + C_0 \quad \text{(third order),}$$

where C_0 is fluorescence at Time = 0; C, C_1, C_2, C_3, are amplitudes of fluorescent change in each phase; k, k_1, k_2, k_3 are respective rate constants.

For FRET measurements in the presence of substrate, either Luciferase or MDH was aggregated in the presence of Hsp42. For subunit association measurements, the aggregation was performed with donor-labeled Hsp42. For subunit dissociation measurements, hetero-labeled Hsp42 oligomers were used. Luciferase was aggregated at 43 °C for 20 minutes, while MDH was aggregated at 41 °C for 30 minutes. After aggregation, samples were immediately subjected to FRET analysis as described above. The association quantification was performed at described above.

Aggregation assay monitored by light scattering

Hsp42 and substrate proteins were centrifuged at 14,000 × g for 15 minutes to remove potential aggregates. Buffers, cuvettes, and the spectrophotometer were pre-heated to the required temperatures. Hsp42 was first mixed with buffer, followed by the addition of substrate or reducing agents (if applicable) immediately before measurement. The total reaction volume for each assay was 300 µL.

For all substrates, the standard buffer was 40 mM Tris-HCl, 150 mM NaCl, pH 7.4. For pH-dependent experiments, the buffer was 20 mM MOPS, 20 mM MES, 150 mM NaCl, adjusted to pH 6.0 or pH 7.5.

All substrate proteins were used at a final concentration of 0.5 µM, except for insulin, which was used at 20 µM. Aggregation was initiated by incubation at specific temperatures: 37 °C for luciferase, 41 °C or 47 °C for malate dehydrogenase, 45 °C for citrate synthase. For insulin, aggregation was triggered by the addition of 10 mM DTT at various temperatures; for lysozyme, by 1 mM TCEP at 30˚C.

Aggregation was monitored by measuring light scattering: at 600 nm for Luciferase, Malate dehydrogenase, Citrate synthase, and Lysozyme, and at 360 nm for Insulin.

5.2.6. Biochemical methods

Cross-linking mass spectrometry

All cross-linking experiments were performed in CR buffer (40 mM HEPES, 150 mM NaCl, pH 7.4), following prior buffer exchange using PD SpinTrap G-25 columns. 10 µM Hsp42 was incubated with either a 50-fold molar excess of DSSO or a 500-fold molar excess of DHSO at 25 °C with shaking at 350 rpm for two hours. For DHSO cross-linking, DMTMM was added in 2-, 5-, and 9-fold molar excess relative to DHSO. The reaction was quenched by buffer exchange into CR buffer using single-use PD SpinTrap G-25 columns.

For Hsp42–substrate cross-linking, 10 µM Hsp42 was incubated with 2 µM of either Luciferase or MDH at 37 °C for 15 minutes or at 41 °C for 60 minutes, respectively. Cross-linking was then carried out under the same conditions as described for Hsp42 alone.

For Hsp42–Ssa1 cross-linking, 2 µM Ssa1 and 10 µM Hsp42 were cross-linked under the same conditions as described above.

Mass spectrometry analysis of cross-linked Hsp42 was performed by the Core Facility for Mass Spectrometry & Proteomics at ZMBH (University of Heidelebrg).. Please refer to the facility for the detailed protocol.

Limited proteolysis coupled with mass spectrometry

10 µM Hsp42 was incubated with 20 nM Proteinase K (1:500 dilution) in 40 mM HEPES, 150 mM NaCl, and 2 mM $CaCl_2$, pH 7.4. Samples were collected every five minutes, mixed with SDS-sample buffer, and immediately boiled at 95 °C for 5 minutes. Proteolysis for mass spectrometry analysis was performed in triplicate. Samples taken at 0, 5, and 15 minutes were mixed with SDS-sample buffer lacking bromophenol blue and boiled at 95 °C for 5 minutes. For details on trypsin digestion, mass spectrometry, and data analysis, refer to the Core Facility for Mass Spectrometry & Proteomics at ZMBH (University of Heidelberg).

Luciferase refolding assay

HKM buffer: 25 mM HEPES-KOH, 50 mM KCl, 10 mM $MgCl_2$, 2 mM DTT, pH = 7.8.

Reaction buffer: 25 mM Glycylglycine, 12.5 mM $MgSO_4$, 5 mM ATP, pH = 7.4.

50 nM Luciferase was denatured in the presence or absence of a 10-fold excess Hsp42 in HKM buffer at 43˚C for 20 min or for 10 minutes in 5.2 M Urea in HKM buffer. 50 µl of denatured Lciferase or Luciferase/Hsp42 complexes was mixed with 50 µl of the chaperone-ATP mix in HKM buffer (final 3 µM Ssa1, 1.5 µM Ydj1 or Sis1, 1.5 µM Hsp104, 2 mM ATP, 3 mM phosphoenolpyruvate, 20 ng/µL pyruvate). Refolding occurred at 25˚C. Luciferase activity was measured by adding 2 µl of the refolding reaction to 125 µl of Reaction buffer and 125 µl of luciferin (final 250 µM) in Luminometer.

MDH refolding assay

Aggregation buffer: 50 mM Tris pH 7.5, 50 mM KCl, 20 mM $MgCl_2$, 2 mM DTT

Measurement buffer: 150 mM Potassium phosphate pH 7.6, 0.5 mM Oxaloacetate, 0.28 mM NADH, 2 mM DTT

1 µM MDH was aggregated in the presence or absence of a 4-fold excess of Hsp42 variants in Aggregation buffer at 47˚C for 30 min. The disaggregation reaction was initiated by addition of 1 µM ClpB with KJE (1 µM DnaK, 0.2 µM DnaJ, 0.1 µM GrpE) or 2 µM ClpG. For the order of addition experiment, Hsp42 variants were added to preformed aggregated MDH. Disaggregation reaction was performed at 30˚C in the ATP-regeneration system (2 mM ATP, 3 mM phosphoenolpyruvate, 20 ng/µL pyruvate). MDH activity was determined at indicated timepoints by mixing 15 µl from a disaggregation reaction with 690 µL Measurement buffer inside a 1 ml Polystyrene Cuvette (Sarstedt). MDH activity was quantified by measuring changes in absorption at 340 nm for 30 s on a Biochrom Novaspec Plus photometer (DA340/min). The activity of native MDH served as a reference to determine disaggregation efficiency.

5.2.7. Others

Quantification and Statistical Analysis

Plotting, data quantification and statistical analyses were done with R/Rstudio. Fitting of data was done with the nls function in base R. p values were calculated by Welch's two-sample t-test using t.test() function integrated in base R.

In box plots, the central line indicates the median, the box spans the interquartile range (25th to 75th percentile), and the whiskers represent the full range of the data, from minimum to maximum

Use of Artificial Intelligence

ChatGPT was used to proofread and edit the original text, as well as to assist with writing code for data analysis. DeepL was used to translate the English Abstract into German.

Supplementary figures

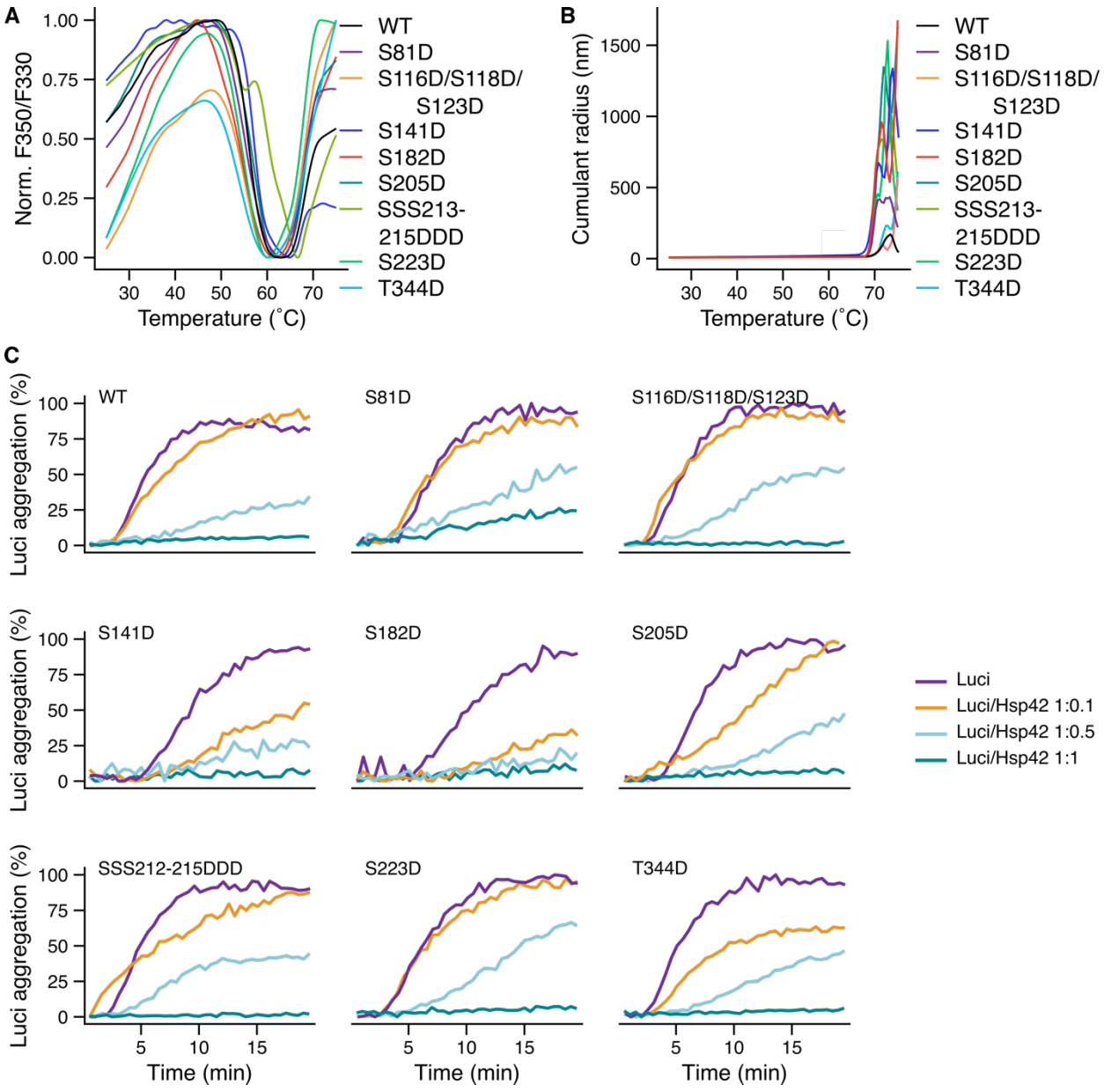

Figure S1. Thermal stability and chaperone activity of Hsp42 phosphomimetic variants. **A.** The normalized ratio of fluorescence at 350 nm to fluorescence at 330 nm of the Hsp42 phosphomimetic variants at 10 µM measured with nanoDSF (n = 2, one representative curve for each variant is shown). **B.** Cumulant radius of Hsp42 phosphomimetic variants at 10 µM upon melting at 10 µM measured with DLS (n = 2, one representative curve for each variant is shown). **C.** Light scattering percent of Luci aggregation in the presence of the Hsp42 phosphomimetic variants at different Luci/Hsp42 ratios at 37˚C.

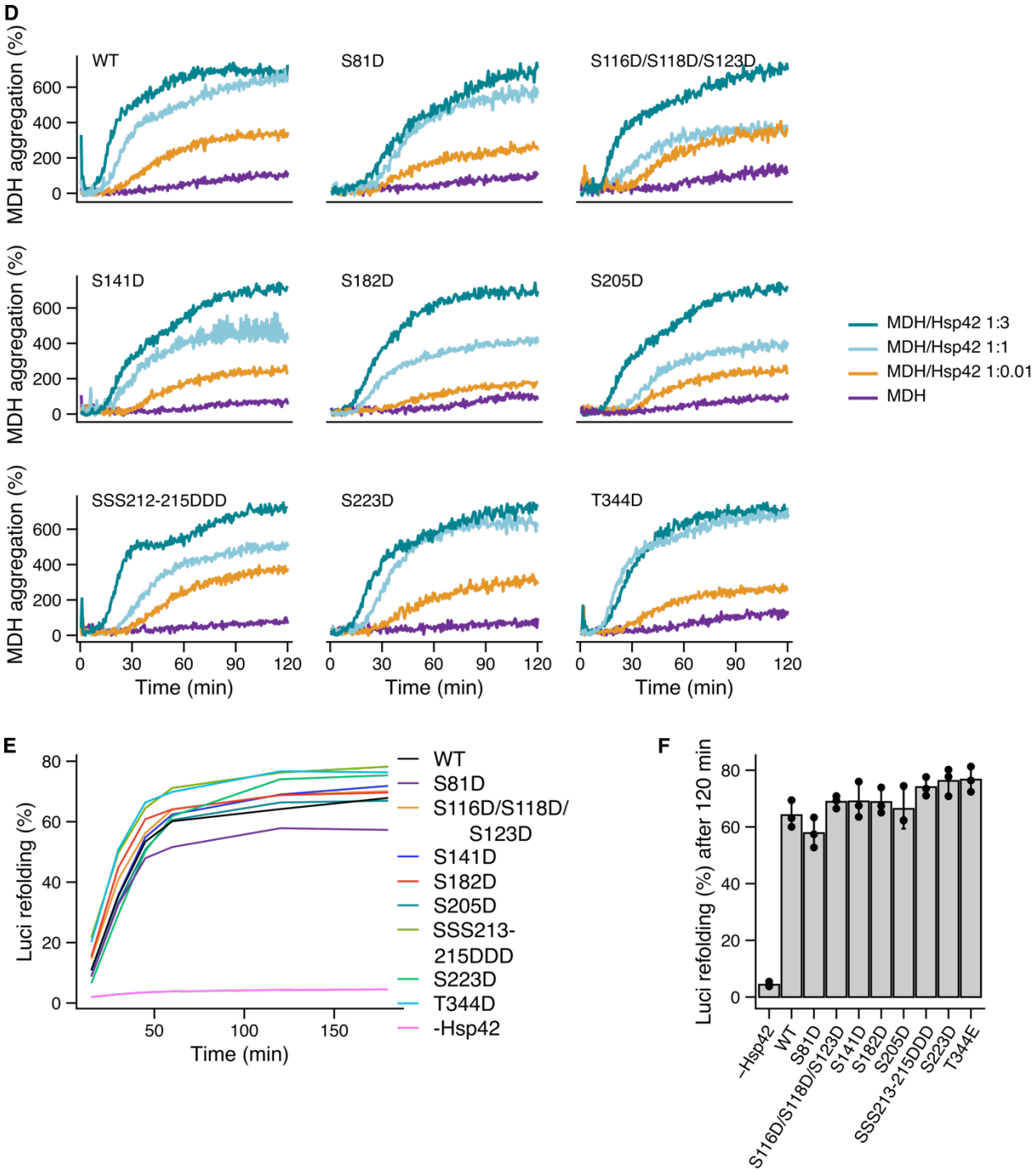

Figure S1 (cont). Thermal stability and chaperone activity of Hsp42 phosphomimetic variants. D. Light scattering percent of MDH in the presence of the Hsp42 phosphomimetic variants at different MDH/Hsp42 ratios at 41˚C. Time-course of Luciferase refolding from the temperature aggregated Hsp42 phosphomimetic variant–Luci complexes by Ssa1, Hsp104, and Ydj1 in the presence of an ATP regeneration system. Luciferase activity was normalized to the activity of the native protein. F. Refolding yield of Luciferase from the temperature aggregated Hsp42 phosphomimetic variant–Luci complexes after 2 hours of incubation. Error bars represent standard deviations (n = 3).

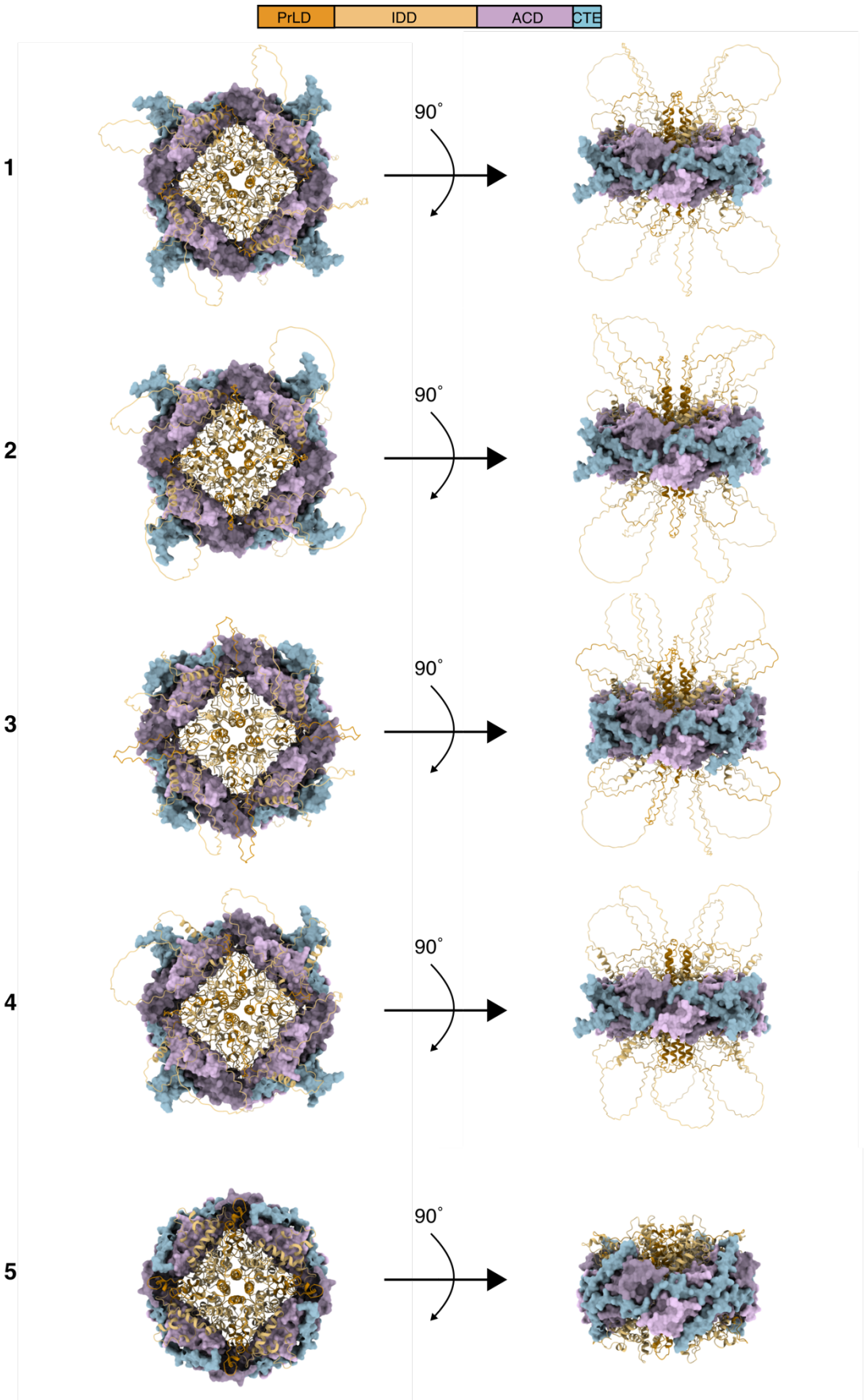

Figure S2. Models of AlphaFold 3 prediction of Hsp42 the octamer. The models are ranked based on the average pLDDT score across all residues, from highest to lowest (1-5).

Literature

Abramson, J., Adler, J., Dunger, J., Evans, R., Green, T., Pritzel, A., Ronneberger, O., *et al.* (2024), "Accurate structure prediction of biomolecular interactions with AlphaFold 3", *Nature*, Vol. 630 No. 8016, pp. 493–500, doi: 10.1038/s41586-024-07487-w.

Aebersold, R., Agar, J.N., Amster, I.J., Baker, M.S., Bertozzi, C.R., Boja, E.S., Costello, C.E., *et al.* (2018), "How many human proteoforms are there?", *Nature Chemical Biology*, Vol. 14 No. 3, pp. 206–214, doi: 10.1038/nchembio.2576.

Ahmadpour, D., Kumar, N., Fischbach, A., Chawla, S., Widlund, P.O. and Nyström, T. (2023), "Syntaxin 5-dependent phosphorylation of the small heat shock protein Hsp42 and its role in protein quality control", *FEBS Journal*, Vol. 290 No. 19, pp. 4744–4761, doi: 10.1111/febs.16886.

Aquilina, J.A., Benesch, J.L.P., Ding, L.L., Yaron, O., Horwitz, J. and Robinson, C.V. (2005), "Subunit exchange of polydisperse proteins", *Journal of Biological Chemistry*, Vol. 280 No. 15, pp. 14485–14491, doi: 10.1074/jbc.m500135200.

Baldwin, A.J., Lioe, H., Hilton, G.R., Baker, L.A., Rubinstein, J.L., Kay, L.E. and Benesch, J.L.P. (2011), "The polydispersity of AB-Crystallin is rationalized by an interconverting polyhedral architecture", *Structure*, Vol. 19 No. 12, pp. 1855–1863, doi: 10.1016/j.str.2011.09.015.

Balzarotti, F., Eilers, Y., Gwosch, K.C., Gynnå, A.H., Westphal, V., Stefani, F.D., Elf, J., *et al.* (2016), "Nanometer resolution imaging and tracking of fluorescent molecules with minimal photon fluxes", *Science*, Vol. 355 No. 6325, pp. 606–612, doi: 10.1126/science.aak9913.

Bartelt-Kirbach, B., Moron, M., Glomb, M., Beck, C.-M., Weller, M.-P. and Golenhofen, N. (2016), "HspB5/αB-crystallin increases dendritic complexity and protects the dendritic arbor during heat shock in cultured rat hippocampal neurons", *Cellular and Molecular Life Sciences*, Vol. 73 No. 19, pp. 3761–3775, doi: 10.1007/s00018-016-2219-9.

Bartolec, T.K., Vázquez-Campos, X., Norman, A., Luong, C., Johnson, M., Payne, R.J., Wilkins, M.R., *et al.* (2023), "Cross-linking mass spectrometry discovers, evaluates, and corroborates structures and protein–protein interactions in the human cell", *Proceedings of the National Academy of Sciences*, Vol. 120 No. 17, doi: 10.1073/pnas.2219418120.

Baughman, H.E.R., Pham, T.-H.T., Adams, C.S., Nath, A. and Klevit, R.E. (2020), "Release of a disordered domain enhances HspB1 chaperone activity toward tau", *Proceedings of the National Academy of Sciences*, Vol. 117 No. 6, pp. 2923–2929, doi: 10.1073/pnas.1915099117.

Benesch, J.L.P., Aquilina, J.A., Baldwin, A.J., Rekas, A., Stengel, F., Lindner, R.A., Basha, E., *et al.* (2010), "The quaternary organization and dynamics of the molecular chaperone HSP26 are thermally regulated", *Chemistry & Biology*, Vol. 17 No. 9, pp. 1008–1017, doi: 10.1016/j.chembiol.2010.06.016.

Bohl, V. and Mogk, A. (2024), "When the going gets tough, the tough get going—Novel bacterial AAA+ disaggregases provide extreme heat resistance", *Environmental Microbiology*, Vol. 26 No. 7, doi: 10.1111/1462-2920.16677.

Bova, M.P., Huang, Q., Ding, L. and Horwitz, J. (2002), “Subunit Exchange, Conformational Stability, and Chaperone-like Function of the Small Heat Shock Protein 16.5 fromMethanococcus jannaschii”, *Journal of Biological Chemistry*, Vol. 277 No. 41, pp. 38468–38475, doi: 10.1074/jbc.m205594200.

Bradford, M.M. (1976), “A rapid and sensitive method for the quantitation of microgram quantities of protein utilizing the principle of protein-dye binding”, *Analytical Biochemistry*, Vol. 72 No. 1–2, pp. 248–254, doi: 10.1016/0003-2697(76)90527-3.

Braun, N., Zacharias, M., Peschek, J., Kastenmüller, A., Zou, J., Hanzlik, M., Haslbeck, M., *et al.* (2011), “Multiple molecular architectures of the eye lens chaperone αB-crystallin elucidated by a triple hybrid approach”, *Proceedings of the National Academy of Sciences*, Vol. 108 No. 51, pp. 20491–20496, doi: 10.1073/pnas.1111014108.

Cabrera, M., Boronat, S., Marte, L., Vega, M., Pérez, P., Ayté, J. and Hidalgo, E. (2020), “Chaperone-Facilitated Aggregation of Thermo-Sensitive Proteins Shields Them from Degradation during Heat Stress”, *Cell Reports*, Vol. 30 No. 7, pp. 2430-2443.e4, doi: 10.1016/j.celrep.2020.01.077.

Cereghetti, G., Kissling, V.M., Koch, L.M., Arm, A., Schmidt, C.C., Thüringer, Y., Zamboni, N., *et al.* (2024), “An evolutionarily conserved mechanism controls reversible amyloids of pyruvate kinase via pH-sensing regions”, *Developmental Cell*, Vol. 59 No. 14, pp. 1876-1891.e7, doi: 10.1016/j.devcel.2024.04.018.

Cimprich, P., SlavÃK, J. and Kotyk, A. (1995), “Distribution of individual cytoplasmic pH values in a population of the yeastSaccharomyces cerevisiae”, *FEMS Microbiology Letters*, Vol. 130 No. 2–3, pp. 245–251, doi: 10.1111/j.1574-6968.1995.tb07727.x.

Clark, A.R., Egberts, W.V., Kondrat, F.D.L., Hilton, G.R., Ray, N.J., Cole, A.R., Carver, J.A., *et al.* (2018), “Terminal regions confer plasticity to the tetrameric assembly of human HSPB2 and HSPB3”, *Journal of Molecular Biology*, Vol. 430 No. 18, pp. 3297–3310, doi: 10.1016/j.jmb.2018.06.047.

Clouser, A.F. and Klevit, R.E. (2017), “pH-dependent structural modulation is conserved in the human small heat shock protein HSBP1”, *Cell Stress and Chaperones*, Vol. 22 No. 4, pp. 569–575, doi: 10.1007/s12192-017-0783-z.

Combe, C.W., Graham, M., Kolbowski, L., Fischer, L. and Rappsilber, J. (2024), “XIVIEW: Visualisation of Crosslinking Mass Spectrometry data”, *Journal of Molecular Biology*, Vol. 436 No. 17, p. 168656, doi: 10.1016/j.jmb.2024.168656.

Das, R.K. and Pappu, R.V. (2013), “Conformations of intrinsically disordered proteins are influenced by linear sequence distributions of oppositely charged residues”, *Proceedings of the National Academy of Sciences*, Vol. 110 No. 33, pp. 13392–13397, doi: 10.1073/pnas.1304749110.

Delbecq, S.P., Jehle, S. and Klevit, R. (2012), “Binding determinants of the small heat shock protein, αB-crystallin: recognition of the ‘IxI’ motif”, *The EMBO Journal*, Vol. 31 No. 24, pp. 4587–4594, doi: 10.1038/emboj.2012.318.

Delbecq, S.P., Rosenbaum, J.C. and Klevit, R.E. (2015), “A mechanism of subunit recruitment in human small heat shock protein oligomers”, *Biochemistry*, Vol. 54 No. 28, pp. 4276–4284, doi: 10.1021/acs.biochem.5b00490.

Ecroyd, H., Meehan, S., Horwitz, J., Aquilina, J.A., Benesch, J.L.P., Robinson, C.V., Macphee, C.E., *et al.* (2006), "Mimicking phosphorylation of αB-crystallin affects its chaperone activity", *Biochemical Journal*, Vol. 401 No. 1, pp. 129–141, doi: 10.1042/bj20060981.

Eisenhardt, B.D. (2013), "Small heat shock proteins: recent developments", *BioMolecular Concepts*, Vol. 4 No. 6, pp. 583–595, doi: 10.1515/bmc-2013-0028.

Erdős, G., Pajkos, M. and Dosztányi, Z. (2021), "IUPred3: prediction of protein disorder enhanced with unambiguous experimental annotation and visualization of evolutionary conservation", *Nucleic Acids Research*, Vol. 49 No. W1, pp. W297–W303, doi: 10.1093/nar/gkab408.

Faust, O., Abayev-Avraham, M., Wentink, A.S., Maurer, M., Nillegoda, N.B., London, N., Bukau, B., *et al.* (2020), "HSP40 proteins use class-specific regulation to drive HSP70 functional diversity", *Nature*, Vol. 587 No. 7834, pp. 489–494, doi: 10.1038/s41586-020-2906-4.

Fleckenstein, T., Kastenmüller, A., Stein, M.L., Peters, C., Daake, M., Krause, M., Weinfurtner, D., *et al.* (2015), "The chaperone activity of the developmental small heat shock protein SIP1 is regulated by pH-Dependent conformational changes", *Molecular Cell*, Vol. 58 No. 6, pp. 1067–1078, doi: 10.1016/j.molcel.2015.04.019.

Franzmann, T.M., Jahnel, M., Pozniakovsky, A., Mahamid, J., Holehouse, A.S., Nüske, E., Richter, D., *et al.* (2018), "Phase separation of a yeast prion protein promotes cellular fitness", *Science*, Vol. 359 No. 6371, doi: 10.1126/science.aao5654.

Franzmann, T.M., Wühr, M., Richter, K., Walter, S. and Buchner, J. (2005), "The Activation Mechanism of Hsp26 does not Require Dissociation of the Oligomer", *Journal of Molecular Biology*, Vol. 350 No. 5, pp. 1083–1093, doi: 10.1016/j.jmb.2005.05.034.

Friedrich, K.L., Giese, K.C., Buan, N.R. and Vierling, E. (2004), "Interactions between Small Heat Shock Protein Subunits and Substrate in Small Heat Shock Protein-Substrate Complexes", *Journal of Biological Chemistry*, Vol. 279 No. 2, pp. 1080–1089, doi: 10.1074/jbc.m311104200.

Frottin, F., Schueder, F., Tiwary, S., Gupta, R., Körner, R., Schlichthaerle, T., Cox, J., *et al.* (2019), "The nucleolus functions as a phase-separated protein quality control compartment", *Science*, Vol. 365 No. 6451, pp. 342–347, doi: 10.1126/science.aaw9157.

Fu, X., Shi, X., Yan, L., Zhang, H. and Chang, Z. (2013), "In vivo substrate diversity and preference of small heat shock protein IBPB as revealed by using a genetically incorporated photo-cross-linker", *Journal of Biological Chemistry*, Vol. 288 No. 44, pp. 31646–31654, doi: 10.1074/jbc.m113.501817.

Glover, J.R. and Lindquist, S. (1998), "HSP104, HSP70, and HSP40", *Cell*, Vol. 94 No. 1, pp. 73–82, doi: 10.1016/s0092-8674(00)81223-4.

Gong, Y., Kakihara, Y., Krogan, N., Greenblatt, J., Emili, A., Zhang, Z. and Houry, W.A. (2009), "An atlas of chaperone–protein interactions in Saccharomyces cerevisiae : implications to protein folding pathways in the cell", *Molecular Systems Biology*, Vol. 5 No. 1, doi: 10.1038/msb.2009.26.

Grousl, T., Ungelenk, S., Miller, S., Ho, C.-T., Khokhrina, M., Mayer, M.P., Bukau, B., *et al.* (2018), "A prion-like domain in Hsp42 drives chaperone-facilitated aggregation of misfolded proteins", *The Journal of Cell Biology*, Vol. 217 No. 4, pp. 1269–1285, doi: 10.1083/jcb.201708116.

Gutierrez, C.B., Yu, C., Novitsky, E.J., Huszagh, A.S., Rychnovsky, S.D. and Huang, L. (2016), "Developing an acidic residue reactive and Sulfoxide-Containing MS-Cleavable homobifunctional Cross-Linker for probing Protein–Protein interactions", *Analytical Chemistry*, Vol. 88 No. 16, pp. 8315–8322, doi: 10.1021/acs.analchem.6b02240.

Hantke, I., Schäfer, H., Janczikowski, A. and Turgay, K. (2018), "YocM a small heat shock protein can protect Bacillus subtilis cells during salt stress", *Molecular Microbiology*, Vol. 111 No. 2, pp. 423–440, doi: 10.1111/mmi.14164.

Harris, H.M.B. and Hill, C. (2021), "A place for viruses on the tree of life", *Frontiers in Microbiology*, Vol. 11, doi: 10.3389/fmicb.2020.604048.

Hartl, F.U., Bracher, A. and Hayer-Hartl, M. (2011), "Molecular chaperones in protein folding and proteostasis", *Nature*, Vol. 475 No. 7356, pp. 324–332, doi: 10.1038/nature10317.

Haslbeck, M., Braun, N., Stromer, T., Richter, B., Model, N., Weinkauf, S. and Buchner, J. (2004), "Hsp42 is the general small heat shock protein in the cytosol of Saccharomyces cerevisiae", *The EMBO Journal*, Vol. 23 No. 3, pp. 638–649, doi: 10.1038/sj.emboj.7600080.

Haslbeck, M., Franzmann, T., Weinfurtner, D. and Buchner, J. (2005), "Some like it hot: the structure and function of small heat-shock proteins", *Nature Structural & Molecular Biology*, Vol. 12 No. 10, pp. 842–846, doi: 10.1038/nsmb993.

Haslbeck, M., Walke, S., Stromer, T., Ehrnsperger, M., White, H.E., Chen, S., Saibil, H.R., *et al.* (1999a), "Hsp26: a temperature-regulated chaperone", *The EMBO Journal*, Vol. 18 No. 23, pp. 6744–6751, doi: 10.1093/emboj/18.23.6744.

Haslbeck, M., Walke, S., Stromer, T., Ehrnsperger, M., White, H.E., Chen, S., Saibil, H.R., *et al.* (1999b), "Hsp26: a temperature-regulated chaperone", *The EMBO Journal*, Vol. 18 No. 23, pp. 6744–6751, doi: 10.1093/emboj/18.23.6744.

Heirbaut, M., Beelen, S., Strelkov, S.V. and Weeks, S.D. (2014), "Dissecting the functional role of the N-Terminal domain of the human small heat shock protein HSPB6", *PLoS ONE*, Vol. 9 No. 8, p. e105892, doi: 10.1371/journal.pone.0105892.

Hilton, G.R., Hochberg, G.K.A., Laganowsky, A., McGinnigle, S.I., Baldwin, A.J. and Benesch, J.L.P. (2013), "C-terminal interactions mediate the quaternary dynamics of αB-crystallin", *Philosophical Transactions of the Royal Society B Biological Sciences*, Vol. 368 No. 1617, p. 20110405, doi: 10.1098/rstb.2011.0405.

Ho, C.-T., Grousl, T., Shatz, O., Jawed, A., Ruger-Herreros, C., Semmelink, M., Zahn, R., *et al.* (2019), "Cellular sequestrases maintain basal Hsp70 capacity ensuring balanced proteostasis", *Nature Communications*, Vol. 10 No. 1, doi: 10.1038/s41467-019-12868-1.

Hoffman, L.M., Jensen, C.C. and Beckerle, M.C. (2022), "Phosphorylation of the small heat shock protein HspB1 regulates cytoskeletal recruitment and cell motility", *Molecular Biology of the Cell*, Vol. 33 No. 11, doi: 10.1091/mbc.e22-02-0057.

Iburg, M., Puchkov, D., Rosas-Brugada, I.U., Bergemann, L., Rieprecht, U. and Kirstein, J. (2020), "The noncanonical small heat shock protein HSP-17 from Caenorhabditis elegans is a selective protein aggregase", *Journal of Biological Chemistry*, Vol. 295 No. 10, pp. 3064–3079, doi: 10.1074/jbc.ra119.011185.

Ito, H., Kamei, K., Iwamoto, I., Inaguma, Y., Nohara, D. and Kato, K. (2001), "Phosphorylation-induced change of the oligomerization state of AB-crystallin", *Journal of Biological Chemistry*, Vol. 276 No. 7, pp. 5346–5352, doi: 10.1074/jbc.m009004200.

Janowska, M.K., Baughman, H.E.R., Woods, C.N. and Klevit, R.E. (2019), "Mechanisms of small heat shock proteins", *Cold Spring Harbor Perspectives in Biology*, Vol. 11 No. 10, p. a034025, doi: 10.1101/cshperspect.a034025.

Jaya, N., Garcia, V. and Vierling, E. (2009), "Substrate binding site flexibility of the small heat shock protein molecular chaperones", *Proceedings of the National Academy of Sciences*, Vol. 106 No. 37, pp. 15604–15609, doi: 10.1073/pnas.0902177106.

Johnston, C.L., Marzano, N.R., Paudel, B.P., Wright, G., Benesch, J.L.P., Van Oijen, A.M. and Ecroyd, H. (2020), "Single-molecule fluorescence-based approach reveals novel mechanistic insights into human small heat shock protein chaperone function", *Journal of Biological Chemistry*, Vol. 296, p. 100161, doi: 10.1074/jbc.ra120.015419.

Jovcevski, B., Kelly, M.A., Rote, A.P., Berg, T., Gastall, H.Y., Benesch, J.L.P., Aquilina, J.A., *et al.* (2015), "Phosphomimics destabilize HSP27 oligomeric assemblies and enhance chaperone activity", *Chemistry & Biology*, Vol. 22 No. 2, pp. 186–195, doi: 10.1016/j.chembiol.2015.01.001.

Kandel, R., Jung, J. and Neal, S. (2023), "Proteotoxic stress and the ubiquitin proteasome system", *Seminars in Cell and Developmental Biology*, Vol. 156, pp. 107–120, doi: 10.1016/j.semcdb.2023.08.002.

Kao, A., Chiu, C.-L., Vellucci, D., Yang, Y., Patel, V.R., Guan, S., Randall, A., *et al.* (2010), "Development of a novel cross-linking strategy for fast and accurate identification of cross-linked peptides of protein complexes", *Molecular & Cellular Proteomics*, Vol. 10 No. 1, p. M110.002170, doi: 10.1074/mcp.m110.002212.

Kim, K.K., Kim, R. and Kim, S.-H. (1998), "Crystal structure of a small heat-shock protein", *Nature*, Vol. 394 No. 6693, pp. 595–599, doi: 10.1038/29106.

Lee, H.-Y., Chao, J.-C., Cheng, K.-Y. and Leu, J.-Y. (2018), "Misfolding-prone proteins are reversibly sequestered to an Hsp42-associated granule upon chronological aging", *Journal of Cell Science*, Vol. 131 No. 16, doi: 10.1242/jcs.220202.

Lelj-Garolla, B. and Mauk, A.G. (2011), "Roles of the N- and C-terminal sequences in Hsp27 self-association and chaperone activity", *Protein Science*, Vol. 21 No. 1, pp. 122–133, doi: 10.1002/pro.761.

Liu, I.-C., Chiu, S.-W., Lee, H.-Y. and Leu, J.-Y. (2012), "The histone deacetylase Hos2 forms an Hsp42-dependent cytoplasmic granule in quiescent yeast cells", *Molecular Biology of the Cell*, Vol. 23 No. 7, pp. 1231–1242, doi: 10.1091/mbc.e11-09-0752.

Liu, Z., Wang, C., Li, Y., Zhao, C., Li, T., Li, D., Zhang, S., *et al.* (2018), "Mechanistic insights into the switch of αB-crystallin chaperone activity and self-multimerization",

Journal of Biological Chemistry, Vol. 293 No. 38, pp. 14880–14890, doi: 10.1074/jbc.ra118.004034.

Mainz, A., Peschek, J., Stavropoulou, M., Back, K.C., Bardiaux, B., Asami, S., Prade, E., *et al.* (2015), "The chaperone αB-crystallin uses different interfaces to capture an amorphous and an amyloid client", *Nature Structural & Molecular Biology*, Vol. 22 No. 11, pp. 898–905, doi: 10.1038/nsmb.3108.

Mateju, D., Franzmann, T.M., Patel, A., Kopach, A., Boczek, E.E., Maharana, S., Lee, H.O., *et al.* (2017), "An aberrant phase transition of stress granules triggered by misfolded protein and prevented by chaperone function", *The EMBO Journal*, Vol. 36 No. 12, pp. 1669–1687, doi: 10.15252/embj.201695957.

Mathias, R.T., Riquelme, G. and Rae, J.L. (1991), "Cell to cell communication and pH in the frog lens.", *The Journal of General Physiology*, Vol. 98 No. 6, pp. 1085–1103, doi: 10.1085/jgp.98.6.1085.

Michaelis, A.C., Brunner, A.-D., Zwiebel, M., Meier, F., Strauss, M.T., Bludau, I. and Mann, M. (2023), "The social and structural architecture of the yeast protein interactome", *Nature*, Vol. 624 No. 7990, pp. 192–200, doi: 10.1038/s41586-023-06739-5.

Miller, A.P., O'Neill, S.E., Lampi, K.J. and Reichow, S.L. (2024), "The α-crystallin Chaperones Undergo a Quasi-ordered Co-aggregation Process in Response to Saturating Client Interaction", *Journal of Molecular Biology*, Vol. 436 No. 8, p. 168499, doi: 10.1016/j.jmb.2024.168499.

Miller, A.P. and Reichow, S.L. (2025), "Mechanism of small heat shock protein client sequestration and induced polydispersity", *Nature Communications*, Vol. 16 No. 1, doi: 10.1038/s41467-025-58964-3.

Mogk, A., Kummer, E. and Bukau, B. (2015), "Cooperation of Hsp70 and Hsp100 chaperone machines in protein disaggregation", *Frontiers in Molecular Biosciences*, Vol. 2, doi: 10.3389/fmolb.2015.00022.

Mogk, A., Ruger-Herreros, C. and Bukau, B. (2019), "Cellular functions and mechanisms of action of small heat shock proteins", *Annual Review of Microbiology*, Vol. 73 No. 1, pp. 89–110, doi: 10.1146/annurev-micro-020518-115515.

Morimoto, R.I. (2008), "Proteotoxic stress and inducible chaperone networks in neurodegenerative disease and aging", *Genes & Development*, Vol. 22 No. 11, pp. 1427–1438, doi: 10.1101/gad.1657108.

Morishita, H. and Mizushima, N. (2019), "Diverse cellular roles of autophagy", *Annual Review of Cell and Developmental Biology*, Vol. 35 No. 1, pp. 453–475, doi: 10.1146/annurev-cellbio-100818-125300.

Morrison, L.E., Hoover, H.E., Thuerauf, D.J. and Glembotski, C.C. (2003), "Mimicking phosphorylation of AB-Crystallin on serine-59 is necessary and sufficient to provide maximal protection of cardiac myocytes from apoptosis", *Circulation Research*, Vol. 92 No. 2, pp. 203–211, doi: 10.1161/01.res.0000052989.83995.a5.

Mühlhofer, M., Peters, C., Kriehuber, T., Kreuzeder, M., Kazman, P., Rodina, N., Reif, B., *et al.* (2021), "Phosphorylation activates the yeast small heat shock protein Hsp26 by

weakening domain contacts in the oligomer ensemble", *Nature Communications*, Vol. 12 No. 1, doi: 10.1038/s41467-021-27036-7.

Mymrikov, E.V., Daake, M., Richter, B., Haslbeck, M. and Buchner, J. (2016), "The chaperone activity and substrate spectrum of human small heat shock proteins", *Journal of Biological Chemistry*, Vol. 292 No. 2, pp. 672–684, doi: 10.1074/jbc.m116.760413.

Nitika, N., Zheng, B., Ruan, L., Kline, J.T., Omkar, S., Sikora, J., Torres, M.T., *et al.* (2022), "Comprehensive characterization of the Hsp70 interactome reveals novel client proteins and interactions mediated by posttranslational modifications", *PLoS Biology*, Vol. 20 No. 10, p. e3001839, doi: 10.1371/journal.pbio.3001839.

Nollen, E. a. A., Salomons, F.A., Brunsting, J.F., Van Der Want, J.J.L., Sibon, O.C.M. and Kampinga, H.H. (2001), "Dynamic changes in the localization of thermally unfolded nuclear proteins associated with chaperone-dependent protection", *Proceedings of the National Academy of Sciences*, Vol. 98 No. 21, pp. 12038–12043, doi: 10.1073/pnas.201112398.

Oka, T. and Futai, M. (2000), "Requirement of V-ATPase for Ovulation and Embryogenesis inCaenorhabditis elegans", *Journal of Biological Chemistry*, Vol. 275 No. 38, pp. 29556–29561, doi: 10.1074/jbc.m002756200.

Orij, R., Postmus, J., Ter Beek, A., Brul, S. and Smits, G.J. (2008), "In vivo measurement of cytosolic and mitochondrial pH using a pH-sensitive GFP derivative in Saccharomyces cerevisiae reveals a relation between intracellular pH and growth", *Microbiology*, Vol. 155 No. 1, pp. 268–278, doi: 10.1099/mic.0.022038-0.

Peschek, J., Braun, N., Rohrberg, J., Back, K.C., Kriehuber, T., Kastenmüller, A., Weinkauf, S., *et al.* (2013), "Regulated structural transitions unleash the chaperone activity of αB-crystallin", *Proceedings of the National Academy of Sciences*, Vol. 110 No. 40, doi: 10.1073/pnas.1308898110.

Plante, S., Moon, K.-M., Lemieux, P., Foster, L.J. and Landry, C.R. (2023), "Breaking spore dormancy in budding yeast transforms the cytoplasm and the solubility of the proteome", *PLoS Biology*, Vol. 21 No. 4, p. e3002042, doi: 10.1371/journal.pbio.3002042.

Quinlan, R.A., Zhang, Y., Lansbury, A., Williamson, I., Pohl, E. and Sun, F. (2013), "Changes in the quaternary structure and function of MjHSP16.5 attributable to deletion of the IXI motif and introduction of the substitution, R107G, in the α -crystallin domain", *Philosophical Transactions of the Royal Society B Biological Sciences*, Vol. 368 No. 1617, p. 20120327, doi: 10.1098/rstb.2012.0327.

Rajagopal, P., Tse, E., Borst, A.J., Delbecq, S.P., Shi, L., Southworth, D.R. and Klevit, R.E. (2015), "A conserved histidine modulates HSPB5 structure to trigger chaperone activity in response to stress-related acidosis", *eLife*, Vol. 4, doi: 10.7554/elife.07304.

Reinle, K., Mogk, A. and Bukau, B. (2021), "The diverse functions of small heat shock proteins in the proteostasis network", *Journal of Molecular Biology*, Vol. 434 No. 1, p. 167157, doi: 10.1016/j.jmb.2021.167157.

Sahl, S.J., Matthias, J., Inamdar, K., Weber, M., Khan, T.A., Brüser, C., Jakobs, S., *et al.* (2024), "Direct optical measurement of intramolecular distances with angstrom precision", *Science*, Vol. 386 No. 6718, pp. 180–187, doi: 10.1126/science.adj7368.

Saji, H., Iizuka, R., Yoshida, T., Abe, T., Kidokoro, S., Ishii, N. and Yohda, M. (2007), "Role of the IXI/V motif in oligomer assembly and function of StHsp14.0, a small heat shock protein from the acidothermophilic archaeon, Sulfolobus tokodaii strain 7", *Proteins Structure Function and Bioinformatics*, Vol. 71 No. 2, pp. 771–782, doi: 10.1002/prot.21762.

Schindelin, J., Arganda-Carreras, I., Frise, E., Kaynig, V., Longair, M., Pietzsch, T., Preibisch, S., *et al.* (2012), "Fiji: an open-source platform for biological-image analysis", *Nature Methods*, Vol. 9 No. 7, pp. 676–682, doi: 10.1038/nmeth.2019.

Shrivastava, A., Sandhof, C.A., Reinle, K., Jawed, A., Ruger-Herreros, C., Schwarz, D., Creamer, D., *et al.* (2022), "The cytoprotective sequestration activity of small heat shock proteins is evolutionarily conserved", *The Journal of Cell Biology*, Vol. 221 No. 10, doi: 10.1083/jcb.202202149.

Sluchanko, N.N., Beelen, S., Kulikova, A.A., Weeks, S.D., Antson, A.A., Gusev, N.B. and Strelkov, S.V. (2017), "Structural Basis for the Interaction of a Human Small Heat Shock Protein with the 14-3-3 Universal Signaling Regulator", *Structure*, Vol. 25 No. 2, pp. 305–316, doi: 10.1016/j.str.2016.12.005.

Sluzala, Z.B., Hamati, A. and Fort, P.E. (2025), "Key role of phosphorylation in small heat shock protein regulation via oligomeric disaggregation and functional activation", *Cells*, Vol. 14 No. 2, p. 127, doi: 10.3390/cells14020127.

Specht, S., Miller, S.B.M., Mogk, A. and Bukau, B. (2011), "Hsp42 is required for sequestration of protein aggregates into deposition sites in Saccharomyces cerevisiae", *The Journal of Cell Biology*, Vol. 195 No. 4, pp. 617–629, doi: 10.1083/jcb.201106037.

Stahl, K., Graziadei, A., Dau, T., Brock, O. and Rappsilber, J. (2023), "Protein structure prediction with in-cell photo-crosslinking mass spectrometry and deep learning", *Nature Biotechnology*, Vol. 41 No. 12, pp. 1810–1819, doi: 10.1038/s41587-023-01704-z.

Stahl, K., Warneke, R., Demann, L., Bremenkamp, R., Hormes, B., Brock, O., Stülke, J., *et al.* (2024), "Modelling protein complexes with crosslinking mass spectrometry and deep learning", *Nature Communications*, Vol. 15 No. 1, doi: 10.1038/s41467-024-51771-2.

Stark, H. (2010), "GRAFIX: Stabilization of fragile macromolecular complexes for single particle Cryo-EM", *Methods in Enzymology on CD-ROM/Methods in Enzymology*, pp. 109–126, doi: 10.1016/s0076-6879(10)81005-5.

Strauch, A., Rossa, B., Köhler, F., Haeussler, S., Mühlhofer, M., Rührnößl, F., Körösy, C., *et al.* (2022), "The permanently chaperone-active small heat shock protein Hsp17 from Caenorhabditis elegans exhibits topological separation of its N-terminal regions", *Journal of Biological Chemistry*, Vol. 299 No. 1, p. 102753, doi: 10.1016/j.jbc.2022.102753.

Szeto, T.H., Rowland, S.L. and King, G.F. (2001), "The dimerization function of MINC resides in a structurally autonomous C-Terminal domain", *Journal of Bacteriology*, Vol. 183 No. 22, pp. 6684–6687, doi: 10.1128/jb.183.22.6684-6687.2001.

Tomiczek, B., Delewski, W., Nierzwicki, L., Stolarska, M., Grochowina, I., Schilke, B., Dutkiewicz, R., *et al.* (2020), "Two-step mechanism of J-domain action in driving Hsp70 function", *PLoS Computational Biology*, Vol. 16 No. 6, p. e1007913, doi: 10.1371/journal.pcbi.1007913.

Tsoi, P.S., Quan, M.D., Ferreon, J.C. and Ferreon, A.C.M. (2023), “Aggregation of Disordered Proteins Associated with Neurodegeneration”, *International Journal of Molecular Sciences*, Vol. 24 No. 4, p. 3380, doi: 10.3390/ijms24043380.

Van Heel, M., Harauz, G., Orlova, E.V., Schmidt, R. and Schatz, M. (1996), “A new generation of the IMAGIC image processing system”, *Journal of Structural Biology*, Vol. 116 No. 1, pp. 17–24, doi: 10.1006/jsbi.1996.0004.

Van Montfort, R.L.M., Basha, E., Friedrich, K.L., Slingsby, C. and Vierling, E. (2001), “Crystal structure and assembly of a eukaryotic small heat shock protein.”, *Nature Structural & Molecular Biology*, Vol. 8 No. 12, pp. 1025–1030, doi: 10.1038/nsb722.

Veinger, L., Diamant, S., Buchner, J. and Goloubinoff, P. (1998), “The Small Heat-shock Protein IbpB from Escherichia coli Stabilizes Stress-denatured Proteins for Subsequent Refolding by a Multichaperone Network”, *Journal of Biological Chemistry*, Vol. 273 No. 18, pp. 11032–11037, doi: 10.1074/jbc.273.18.11032.

Weeks, S.D., Baranova, E.V., Heirbaut, M., Beelen, S., Shkumatov, A.V., Gusev, N.B. and Strelkov, S.V. (2014), “Molecular structure and dynamics of the dimeric human small heat shock protein HSPB6”, *Journal of Structural Biology*, Vol. 185 No. 3, pp. 342–354, doi: 10.1016/j.jsb.2013.12.009.

Weitzel, G., Pilatus, U. and Rensing, L. (1987), “The cytoplasmic pH, ATP content and total protein synthesis rate during heat-shock protein inducing treatments in yeast”, *Experimental Cell Research*, Vol. 170 No. 1, pp. 64–79, doi: 10.1016/0014-4827(87)90117-0.

Wu, D., Vonk, J.J., Salles, F., Vonk, D., Haslbeck, M., Melki, R., Bergink, S., *et al.* (2019), “The N terminus of the small heat shock protein HSPB7 drives its polyQ aggregation–suppressing activity”, *Journal of Biological Chemistry*, Vol. 294 No. 25, pp. 9985–9994, doi: 10.1074/jbc.ra118.007117.

Wyszkowski, H., Janta, A., Sztangierska, W., Obuchowski, I., Chamera, T., Kłosowska, A. and Liberek, K. (2021), “Class-specific interactions between Sis1 J-domain protein and Hsp70 chaperone potentiate disaggregation of misfolded proteins”, *Proceedings of the National Academy of Sciences*, Vol. 118 No. 49, doi: 10.1073/pnas.2108163118.

Yu, C., Leung, S.K.P., Zhang, W., Lai, L.T.F., Chan, Y.K., Wong, M.C., Benlekbir, S., *et al.* (2021), “Structural basis of substrate recognition and thermal protection by a small heat shock protein”, *Nature Communications*, Vol. 12 No. 1, doi: 10.1038/s41467-021-23338-y.

Zhang, S., Zhu, Y., Lu, J., Liu, Z., Lobato, A.G., Zeng, W., Liu, J., *et al.* (2022), “Specific binding of Hsp27 and phosphorylated Tau mitigates abnormal Tau aggregation-induced pathology”, *eLife*, Vol. 11, doi: 10.7554/elife.79898.

Żwirowski, S., Kłosowska, A., Obuchowski, I., Nillegoda, N.B., Piróg, A., Ziętkiewicz, S., Bukau, B., *et al.* (2017), “Hsp70 displaces small heat shock proteins from aggregates to initiate protein refolding”, *The EMBO Journal*, Vol. 36 No. 6, pp. 783–796, doi: 10.15252/embj.201593378.

Table of Figures

Table of Tables

Abbreviations

A	Acceptor
Å	Angström
AAA+	ATPase associated with diverse cellular activities
ACD	a-crystallin domain
aSEC	Analytical size-exclusion chromatography
ATP	Adenosine-5'-triphosphate
AU	Arbitrary unit
BLI	Bio-layer interferometry
Cryo-EM	Cryogenic electron microscopy
CS	Citrate synthase
CTE	C-terminal extension
D	Donor
DHSO	Dihydrazide sulfoxide
DLS	Dynamic light scattering
DMTMM	4-(4,6-dimethoxy-1,3,5-triazin-2-yl)-4-methylmorpholinium chloride
dRI	Differential refrective index
DSSO	Disuccinimidyl sulfoxide
DTT	Dithiothreitol
EM	Electron microscopy
FRET	Förster resonance energy transfer
Hsp	Heat shock protein
IDD	Intrinsically disordered domain
IgG	Immunoglobulin G
Ins	Insulin
IPTG	Isopropyl-β-D-thiogalactopyranosid
JDP	J-domain protein
kDa	Kilodalton
Luci	Luciferase
Lys	Lysozyme
mAU	Milli absorbance units
MBP	Maltose binding protein
MEA	Mercaptoethylamine
MDH	Malate dehydrogenase
MinFlux	Minimal fluorescence photon fluxes microscopy
MW	Molecular weight
m/z	Mass-to-charge ratio
nanoDSF	Nano differential scanning fluorometry
NTE	N-terminal extension
PAE	Predicted aligned error
pLDDT	Predicted local distance difference test
PrLD	Prion-like domain
pTM	Predicted template modeling-score
PQS	Protein quality control
SD	Standard deviation
SDS-PAGE	Sodium dodecyl sulfate - polyacrylamide gel electrophoresis
SEC	Size-exclusion chromatography
SEC-MALS	Size-exclusion chromatography with multi-angle light scattering
sHsp	Small heat shock protein
TCEP	tris(2-carboxyethyl)phosphine
XL	Cross-link
βME	β-mercaptoethanol

Acknowledgements

I would like to thank my family for being there for me – mom, dad, sister, and Mira. I thank Bernd Bukau, Axel Mogk, Matthias Mayer for supervision, my defense committee members – Ilka Bischofs and Sebastian Schuck; my lab colleagues – Regina, Lucia, Timo, Valentin, Mariasole, Stefano, Kevin, Pana, Karmen, and Areeb, members of the Mayer's lab in ZMBH – Veronika, Ira, Moritz, Yuantao, Yang, and Sczymon; my collaborators from Gdansk – Krzysztof Liberek, Hubert, Piots, Wiktoria, Klaudia; my collaborators from the Mass spectrometry facility in ZMBH – Marcin, Sabine, Nicole, and Ute; Charlotte from the MinFlux facility in BioQuant; Holger from the Imaging facility in ZMBH; Dirk from the EM facility in BZH; Karine form the Protein Expression and Purification Core Facility in EMBL; Merlin from the Sinning lab in BZH; Stefan Pfeffer, Erik, and Giulia from the Pfeffer lab in ZMBH.